

# DISSERTATION

## **Thermal Oxidation and Dopant Activation of Silicon Carbide**

ausgeführt zum Zwecke der Erlangung des akademischen  
Grades

eines Doktors der technischen Wissenschaften

eingereicht an der Technischen Universität Wien  
Fakultät für Elektrotechnik und Informationstechnik

von

**Vito Šimonka**

Argentinerstraße 16/3/44  
1040 Wien, Österreich

geboren am 18. April 1991 in Murska Sobota, Slowenien

Wien, im September 2018

---



# Abstract

One of the most investigated materials in microelectronics is currently the wide bandgap semiconductor silicon carbide. Due to its attractive material properties, silicon carbide-based applications are promising higher energy efficiencies and at the same time higher operating temperatures, frequencies, and voltages, whilst allowing further physical downscaling. However, for a broad utilization, silicon carbide is facing several limitations due to crystal orientation-dependent phenomena as well as poor electrical characteristics. In order to significantly boost the exploitation of silicon carbide as a key substrate material for microelectronic devices, it is crucial to fully comprehend and predict the physical effects of the involved fabrication processing steps. Those predictions are based on modeling and simulation techniques, which are vital for the design and optimization of devices and device fabrication processes. The ultimate goal of simulation-based predictions is to reduce the need for conventional, cost-intensive experimental investigations and thus to reduce development costs, ultimately allowing to sustain the high pace of progress in semiconductor industry. In this work two key challenges in modeling and simulation of silicon carbide device fabrication are investigated and overcome: Thermal oxidation and dopant activation. The first part focuses on the oxidation mechanisms and models, in particular Massoud's model, which is calibrated for the four most common crystal orientations. In addition, a novel interpolation method for oxidation growth rates, which enables accurate three-dimensional simulations of arbitrary structures, is presented and evaluated. The second part focuses on the activation of dopants during post-implantation annealing. After a discussion of the physics involved in annealing processes, three activation models are presented. The developed models and their calibrated parameters have been implemented into Silvaco's Victory Process simulator which is used to perform numerous studies of various silicon carbide devices to verify the modeling approaches. The results show that it is crucial for device fabrication simulations to be able to accurately predict the geometry and doping profiles of silicon carbide devices. For this reason, this work provides a new understanding of the oxidation and activation mechanisms, promotes the advancement of the silicon carbide semiconductor technology, and, finally, enables to advance technology computer-aided design tools with novel modeling and simulation capabilities for oxidation and post-implantation annealing processes.



# Kurzfassung

Eines der am meisten untersuchten Materialien in der Mikroelektronik ist derzeit der Halbleiter mit großer Bandlücke Siliziumkarbid. Aufgrund seiner attraktiven Materialeigenschaften versprechen Anwendungen auf Siliziumkarbid-Basis eine höhere Energieeffizienz trotz höherer Betriebstemperaturen, -frequenzen und -spannungen, während gleichzeitig ein weiteres Verkleinern von Bauelementen ermöglicht wird. Die breite Verwendung von Siliziumkarbid ist jedoch aufgrund von kristallorientierungsabhängigen Phänomenen, sowie schlechten elektrischen Eigenschaften begrenzt. Um die Nutzung von Siliziumkarbid als wichtiges Substratmaterial für mikroelektronische Bauelemente signifikant zu steigern, ist es entscheidend, die physikalischen Effekte der involvierten Herstellungsschritte ganzheitlich zu verstehen und vorherzusagen. Diese Vorhersagen basieren auf Modellierungs- und Simulationstechniken, welche entscheidend sind für den Entwurf und die Optimierung von Geräten und Herstellungsprozessen. Das ultimative Ziel dieser simulationsbasierten Vorhersagen ist es, den Bedarf für konventionelle, kostenintensive, experimentelle Untersuchungen und somit die Entwicklungskosten zu reduzieren, um letztlich das hohe Tempo des Fortschritts in der Halbleiterindustrie aufrechtzuerhalten. In dieser Arbeit werden zwei zentrale Herausforderungen bei der Modellierung und Simulation der Herstellung von Siliziumkarbid-Bauelementen untersucht und überwunden: Thermische Oxidation und Dotierstoffaktivierung. Der erste Teil befasst sich mit Oxidationsmechanismen und -modellen, insbesondere mit Massoud's empirischem Modell, welches für die vier häufigsten Kristallorientierungen kalibriert ist. Darüber hinaus wird eine neuartige Interpolationmethode für Oxidationswachstumsraten, die eine genaue dreidimensionale Simulation beliebiger Strukturen ermöglicht, vorgestellt und untersucht. Der zweite Teil konzentriert sich auf die Aktivierung von Dopanden während des Ausheilens nach der Ionenimplantation. Nach einer Beschreibung der involvierten Physik in den Ausheilverfahren werden drei Aktivierungsmodelle vorgestellt. Die entwickelten Modelle und ihre kalibrierten Parameter wurden in Silvacos Simulationswerkzeug, Victory Process, implementiert, welches zur Durchführung zahlreicher Untersuchungen verschiedener Siliziumkarbid-Bauelemente zur Verifizierung der Modellierungsansätze verwendet wird. Die Ergebnisse zeigen, dass es für die Herstellung von Bauelementen entscheidend ist, die Geometrie und Dotierungsprofile von Siliziumkarbid-Bauelementen genau vorherzusagen zu können. Aus diesem Grunde schafft diese Arbeit ein neues Verständnis der Oxidations- und Aktivierungsmechanismen und kann so die Weiterentwicklung der Siliziumkarbid-Halbleitertechnologie fördern, wodurch ein Fortschritt von computer-gestützten Entwurfswerkzeugen mit neuartigen Modellierungs- und Simulationsfähigkeiten für Oxidations- und Post-Implantationsausheilverfahren ermöglicht wird.



# Acknowledgement

First and foremost, I would like to thank my advisor Prof. Dr. Siegfried Selberherr for providing me with a supportive working environment, where I was able to pursue my ideas and attend numerous international conferences and courses, where I was able to collaborate and exchange ideas with renowned leading experts.

Additional thanks go to our project leader Dr. Josef Weinbub for the opportunity to be part of the Christian Doppler Laboratory for High Performance TCAD at the Institute for Microelectronics, TU Wien. Thanks for many valuable discussions, excellent research ideas, and elaborated suggestions.

I would also like to thank Dr. Andreas Hössinger, product manager for process simulations at Silvaco Europe Ltd., for constant support, availability, and motivation by providing unique research challenges and discussions.

I am very grateful to my colleagues Paul Manstetten, Giorgios Diamantopoulos, Lukas Gnam, and others for their support and numerous excellent discussions, which constructively pushed research further. In addition, I am thankful to our research group for making me feel like a part of a big collective and making it a pleasure to work every day.

To my girlfriend, I am grateful for showing me that the research is not the only thing to fall in love with. To my parents Ivanka Režonja Šimonka and Jožef Šimonka, who have sacrificed a lot in their lives in order to provide me with a life where I feel that every goal is within my reach, I am and forever remain grateful.



# Contents

<b>Abstract</b>	<b>I</b>
<b>Kurzfassung</b>	<b>III</b>
<b>Acknowledgement</b>	<b>V</b>
<b>List of Acronyms</b>	<b>IX</b>
<b>List of Symbols</b>	<b>XI</b>
<b>1 Introduction</b>	<b>1</b>
1.1 Silicon Carbide . . . . .	1
1.1.1 Crystallography . . . . .	2
1.1.2 Physical Properties . . . . .	6
1.1.3 Device Applications . . . . .	10
1.2 Device Fabrication . . . . .	12
1.2.1 Photolithography . . . . .	14
1.2.2 Etching . . . . .	14
1.2.3 Deposition . . . . .	15
1.2.4 Oxidation . . . . .	16
1.2.5 Ion Implantation . . . . .	16
1.2.6 Annealing and Diffusion . . . . .	17
1.2.7 Dicing and Packaging . . . . .	18
1.3 TCAD . . . . .	18
1.3.1 Process Simulations . . . . .	19
1.3.2 Device Simulations . . . . .	19
1.3.3 Circuit Simulations . . . . .	20
1.3.4 TCAD Tools . . . . .	20
1.4 Research Goals . . . . .	21
1.4.1 Research Setting . . . . .	22
1.5 Outline . . . . .	22
<b>2 Thermal Oxidation</b>	<b>23</b>
2.1 Silicon Dioxide . . . . .	24
2.2 Fundamentals of the Oxidation Mechanism . . . . .	26
2.3 Oxidation Models . . . . .	28
2.3.1 Deal-Grove Model . . . . .	28

2.3.2	Massoud's Model . . . . .	32
2.3.3	C and Si Emission Model . . . . .	34
2.3.4	Summary of Oxidation Models . . . . .	36
2.4	Growth Rates . . . . .	36
2.4.1	Arrhenius Equation . . . . .	39
2.4.2	Calibrated Parameters . . . . .	41
2.5	Interpolation Method . . . . .	47
2.5.1	Parametric Expression . . . . .	48
2.5.2	Explicit Expression . . . . .	50
2.6	Orientation-Dependent Oxidation Model . . . . .	55
2.6.1	Process Simulations . . . . .	56
2.7	Molecular Dynamics Simulations of Orientation Dependences . . . . .	62
2.7.1	Simulation Setup . . . . .	63
2.7.2	Simulation Results and Analyses . . . . .	64
2.8	Summary of Research Achievements . . . . .	72
<b>3</b>	<b>Dopant Activation</b>	<b>73</b>
3.1	Fundamentals of Carrier Concentration . . . . .	75
3.1.1	General Analysis of Impurities . . . . .	75
3.1.2	Charge Neutrality Equation . . . . .	78
3.1.3	Charge Neutrality Fitting . . . . .	79
3.2	Activation Ratio Model . . . . .	83
3.2.1	Methodology . . . . .	83
3.2.2	Calibration . . . . .	84
3.3	Semi-Empirical Model . . . . .	87
3.3.1	Methodology . . . . .	88
3.3.2	Calibration . . . . .	89
3.3.3	Characterization . . . . .	93
3.3.4	Simulations . . . . .	95
3.4	Transient Model . . . . .	99
3.4.1	Methodology . . . . .	99
3.4.2	Calibration . . . . .	101
3.4.3	Characterization . . . . .	103
3.4.4	Simulations . . . . .	107
3.5	Summary of Research Achievements . . . . .	113
<b>4</b>	<b>Conclusions</b>	<b>115</b>
	<b>Bibliography</b>	<b>133</b>
	<b>Curriculum Vitae</b>	<b>135</b>
	<b>Own Publications</b>	<b>139</b>

# List of Acronyms

1D, 2D, 3D	one-, two-, and three-dimensional
Al	aluminium
ALD	atomic layer deposition
AFM	atomic force microscopy
B	boron
C	carbon
CrN	chromium nitride
CVD	chemical vapor deposition
ECD	electrochemical deposition
FA	furnace annealing
GaAs	gallium arsenide
GaN	gallium nitride
Ge	germanium
H <sub>2</sub> O	dihydrogen oxide (water)
IGBT	insulated-gate bipolar transistors
JFET	junction-gate field-effect transistors
LAMMPS	large-scale atomic/molecular massively parallel simulator
LED	light emitting diode
MBE	molecular beam epitaxy
MD	molecular dynamics
MESFET	metal-semiconductor field-effect transistor
MOSFET	metal-oxide-semiconductor field-effect transistor
N	nitrogen
NO	nitric oxide
O	oxygen (element)
O <sub>2</sub>	oxygen (molecule)
P	phosphorus
PVD	physical vapor deposition

RBS	Rutherford backscattering spectrometry
ReaxFF	reactive force-field
RTA	rapid thermal annealing
SBD	Schottky barrier diode
Si	silicon
SiC	silicon carbide
Si <sub>2</sub> C	disilicon carbide
SiC <sub>2</sub>	silicon dicarbide
SiO <sub>2</sub>	silicon dioxide
TCAD	technology computer-aided design
TEM	transmission electron microscopy
Ti	titanium
TiAlN	titanium aluminium nitride
TiN	titanium nitride
QM	quantum mechanics
VSC-3	Vienna Scientific Cluster 3
W	tungsten
ZrN	zirconium nitride

# List of Symbols

## Physical Quantities

Symbol	Description	Unit
$a$	width of a crystal unit cell	$\mu\text{m}$
$\alpha_{\text{CO}}$	production ratio of CO	1
$b$	height of a crystal unit cell	$\mu\text{m}$
$B$	parabolic rate coefficient	$\text{m}^2/\text{s}$
$B/A$	linear rate coefficient	$\text{m}/\text{s}$
$C$	initial enhancement parameter	$\mu\text{m}/\text{s}$
$C^*, C_0$	concentration of the oxidants in the gas ambient and at the oxide surface	$\text{cm}^{-3}$
$C_{\text{act}}$	active dopant concentration	$\text{cm}^{-3}$
$C_{\text{C}}, C_{\text{C}}^{\text{I}}, C_{\text{C}}^{\text{S}}$	concentrations of C, C interstitial, and C at the oxide surface	$\text{cm}^{-3}$
$C_{\text{C}}^0$	solubility limit of C	$\text{cm}^{-3}$
$C_{\text{init}}$	initial active dopant concentration	$\text{cm}^{-3}$
$C_{\text{O}}, C_{\text{O}}^{\text{S}}$	concentrations of O and O at the oxide surface	$\text{cm}^{-3}$
$C_{\text{th}}$	threshold concentration	$\text{cm}^{-3}$
$C_{\text{tot}}$	total doping concentration	$\text{cm}^{-3}$
$C_{\text{S}}$	concentration of the oxidants at the interface	$\text{cm}^{-3}$
$C_{\text{Si}}, C_{\text{Si}}^{\text{I}}, C_{\text{Si}}^{\text{S}}$	concentrations of Si, Si interstitials, and Si at the oxide surface	$\text{cm}^{-3}$
$C_{\text{Si}}^0$	solubility limit of Si	$\text{cm}^{-3}$
$C_{\text{ss}}$	solid solubility	$\text{cm}^{-3}$
$D$	oxidant diffusion coefficient in the oxide	$\text{m}^2/\text{s}$
$D_{\text{C}}, D_{\text{O}}, D_{\text{Si}}$	diffusion coefficient of C, O, and Si	$\text{m}^2/\text{s}$
$E$	energy	eV

$E_a$	activation energy	eV
$E_A, E_D$	ionization energy of acceptors and donors	eV
$E_B$	breakdown field	MV/cm
$E_C$	bottom edge of the conduction band	eV
$E_F$	Fermi level	eV
$E_V$	top edge of the valence band	eV
$E_g$	energy bandgap	eV
$\varepsilon_s$	relative dielectric constant	1
$\eta, \eta'$	oxidation rate of Si and C interstitials on the oxide surface	1
$F_{1-3}$	oxidation fluxes	$\text{cm}^{-2} \text{s}^{-1}$
$F_{\text{act}}$	empirical scalar parameter	1
$g_A, g_D$	spin degeneracy factor of acceptors and donors	1
$h$	gas-phase transport coefficient	m/s
$H$	inverse Henry's law constant	$\text{mol}/\text{m}^3\text{Pa}$
$k$	reaction rate coefficient	$\text{cm}^3 \text{mol}^{-1} \text{s}^{-1}$
$k_0$	initial interfacial oxidation rate	m/s
$k_s$	surface oxidation rate coefficient	m/s
$k_{\text{Si}}, k_m, k_a, k_C$	oxidation growth rates in direction of the Si-, m-, a-, and C-face	$\text{s}^{-1}$
$\kappa$	characteristic reaction rate	$\text{s}^{-1}$
$\kappa_{1/2}, \kappa'_{1/2}$	oxidation rates of Si and C interstitials on the oxide surface	m/s
$L$	characteristic length	$\mu\text{m}$
$\lambda$	thermal conductivity	W/cm K
$M_C$	number of equivalent minima in the conduction band	1
$m_e^*, m_h^*$	effective mass of electrons and holes	kg
$\mu_n$	electron mobility	$\text{cm}^2/\text{Vs}$
$\mu_p$	hole mobility	$\text{cm}^2/\text{Vs}$
$n$	electron concentration	$\text{cm}^{-3}$
$n_i$	intrinsic carrier concentration	$\text{cm}^{-3}$
$N$	number of oxidant species	$\text{cm}^{-3}$
$N_A, N_D$	acceptor and donor concentration	$\text{cm}^{-3}$

$N_C, N_V$	effective density of states in the conduction and valence band	$\text{cm}^{-3}$
$\nu_{\text{Si}}, \nu_{\text{C}}$	emission ratio of Si and C	1
$p$	hole concentration	$\text{cm}^{-3}$
$p_x$	partial pressure	Pa
$R_{\frac{1}{2}}$	half-maximal electrical activation ratio	1
$R_{\text{act}}$	electrical activation ratio	1
$R_{\text{act}}^{\text{n}}, R_{\text{act}}^{\text{p}}$	electrical activation ratio of n-type and p-type doping	1
$R_{\text{max}}, R_{\text{min}}$	maximal and minimal electrical activation ratio	1
$\rho$	density of a crystal unit cell	$\text{g}/\text{cm}^{-3}$
$\rho_C, \rho_V$	density of states in the conduction and valence band	$\text{cm}^3$
$t$	time	s
$T$	temperature	$^{\circ}\text{C}$
$t_A$	annealing time	min
$T_A$	annealing temperature	$^{\circ}\text{C}$
$T_{\text{ip}}$	temperature at the inflection point	$^{\circ}\text{C}$
$T_{\text{melt}}$	melting point	$^{\circ}\text{C}$
$x, y, z$	direction vector coordinates	1
$\hat{X}$	normalized oxide thickness	1
$X$	thickness of the oxide	$\mu\text{m}$
$X_{\text{init}}$	initial thickness of the oxide	$\mu\text{m}$
$X_{\text{max}}$	maximal thickness of the oxide	$\mu\text{m}$
$Z$	pre-exponential factor	$\text{cm}^{-3}$

## Physical Constants

Symbol	Description	Value
$h$	Planck constant	$6.62607 \cdot 10^{-34} \text{ Js}$
$k_{\text{B}}$	Boltzmann constant	$1.38065 \cdot 10^{-23} \text{ JK}^{-1}$
$m_0$	rest mass of an electron	$9.10938 \cdot 10^{-31} \text{ kg}$
$R$	ideal gas constant	$8.31446 \text{ J K}^{-1} \text{ mol}^{-1}$



# 1 Introduction

Semiconductor devices were the key enabler for the arrival of the computer age, also known as the second industrial revolution. At the heart of the information and communication technologies, integrated circuits (ICs) - based on an ensemble of semiconductor devices - find applications in consumer electronics, automobiles, medical equipment, industrial devices, and many more. The dominant semiconductor for the majority of electronic devices has for a long time been silicon (Si). However, recently wide-bandgap semiconductors, particularly silicon carbide (SiC), attracted much attention because of many key benefits over other semiconductor materials in a large number of industrial and military applications [1], [2]. Although Si has been used for high-power, high-temperature, and high-frequency devices, significant performance improvements of Si devices can no longer be expected, because the devices have reached their performance limit introduced by the material's inherent physical properties [3]. Thus, SiC power devices will set new standards in power savings for virtually everything that converts or uses electricity, from wind turbines and solar installations to industrial data centers, hybrid cars, and medical imaging systems, just to name a few. Apart from the significant progress achieved in the area of SiC-based electronics continued advancements in numerical simulations are necessary to enhance the design and optimization of SiC devices, which will further optimize the devices and reduce fabrication costs. The development of novel electronic devices thus requires accurate one- (1D), two- (2D), and three-dimensional (3D) modeling approaches to be able to predict physical phenomena during device fabrication and operation.

## 1.1 Silicon Carbide

Naturally occurring SiC, also known as moissanite, is extremely rare and can be found only in certain types of meteorite. It was found in 1983 as a small component of the Canyon Diablo meteorite in Arizona [4]. Because of the rarity of natural moissanite, most of SiC is synthetic. The simplest manufacturing process is to combine silica sand and carbon (C) in an Acheson graphite electric resistance furnace [5] at a high-temperature, between 1600°C and 2500°C. The material formed in the Acheson furnace varies in purity, according to its distance from the graphite resistor heat source. Pure SiC can be made by the Lely process, in which SiC powder is sublimated into high-temperature species of Si, C, silicon dicarbide (SiC<sub>2</sub>), and disilicon carbide (Si<sub>2</sub>C) in an argon gas ambient at 2500°C and finally redeposited into flake-like single crystals [6].

This method was extended as seeded sublimation technique in the late 1970s [7]. The latter method was further refined in the early 1990s [8] for producing large-diameter SiC boules. Various modifications of these techniques are now used at many laboratories worldwide. Bulk single crystals of SiC with diameters of  $> 100$  mm are fabricated today [9].

Among the wide-bandgap semiconductors, SiC is the only compound semiconductor which can be thermally oxidized in the form of silicon dioxide ( $\text{SiO}_2$ ), similarly to Si. Devices which can be fabricated on Si substrates, such as power metal-oxide-semiconductor field-effect transistors (MOSFET) and insulated-gate bipolar transistors (IGBT), can thus also be fabricated on SiC substrates. Therefore, SiC is considered to be a post Si power device material, as SiC offers superior physical properties over Si, such as wide-bandgap, high electrical breakdown voltage, and high thermal conductivity [10], [11]. However, in order to take advantage of these superior properties of SiC, many challenges on the material level must be better understood and eventually overcome, particularly concerning crystal structure, substrate orientation, bond formation, dopant activation, and ionization [12].

### 1.1.1 Crystallography

SiC exists in more than 250 crystal structures, known as crystalline forms, which are called polytypes [13]. They are variations of the same chemical compound, which are identical in two dimensions and differ in the third. Thus, the polytypes can be viewed as layers stacked in a certain sequence [14]. Each SiC bilayer can be oriented into only three possible positions with respect to the lattice, while the tetrahedral bonding is maintained. These three layers are arbitrarily denoted A, B, and C. The most common polytypes of SiC presently being developed for electronics are the cubic 3C-SiC, the hexagonal 4H-SiC and 6H-SiC, and the rhombohedral 15R-SiC. 3C-SiC is the only form of SiC with a cubic crystal lattice structure which is similar to Si. The prefix number, e.g., 3 in 3C-SiC, refers to the number of layers needed for periodicity, i.e., the stacking sequence ABC. 4H-SiC consists of an equal number of cubic and hexagonal bonds with a stacking sequences of ABAC, while 6H-SiC is composed of two-thirds cubic bonds and one-third hexagonal bonds with a stacking sequence of ABCACB. The overall symmetry is hexagonal for both polytypes, despite the cubic bonds which are present in each. Cubic lattice sites are typically denoted as k and hexagonal sites as h. Similarly, 15R-SiC is a rhombohedral crystal structure composed of three-fifth cubic bonds and two-fifth hexagonal bonds. The stacking sequences among common SiC polytypes are summarized in Table 1.1.

Changing the stacking sequence of SiC has an impact on the mechanical material properties [15], particularly on lattice constants, i.e., basic cell dimensions. The lattice height  $b$  of 6H-SiC is approximately 1.5 times higher than of 4H-SiC. However, the lattice width  $a$  is almost identical for both hexagonal polytypes. In contrary, the basic cube dimension of 3C-SiC is higher than the hexagon width of 4H- and 6H-SiC, while the density of all three polytypes remains equal. The common SiC polytypes have, compared to Si, gallium nitride (GaN), and gallium arsenide (GaAs), approximately a five times higher thermal conductivity and an approximately two times higher melting point<sup>1</sup>. The mechanical properties of 3C-SiC, 4H-SiC, 6H-SiC, Si, and GaAs are summarized in Table 1.2.

Table 1.1: Stacking sequences of common SiC polytypes. k and h refer to cubic and hexagonal lattice sites, respectively.

Polytype	Stacking Sequence	No. k	No. h
3C	ABC	1	0
4H	ABAC	1	1
6H	ABCACB	2	1
15R	ABCACBCABACBCB	3	2

Table 1.2: Mechanical material properties of common SiC polytypes and other common semiconductors.  $a$  and  $b$  are the width and the height of the crystal unit cell, respectively,  $\rho$  is the density of the crystal unit cell,  $\lambda$  is the thermal conductivity, and  $T_{\text{melt}}$  is the melting point.

Property	3C-SiC	4H-SiC	6H-SiC	Si	GaAs
$a$ [Å]	4.359	3.073	3.081	5.43	5.65
$b$ [Å]	4.359	10.05	15.12	5.43	5.65
$\rho$ [gm/cm <sup>3</sup> ]	3.2	3.2	3.2	2.3	5.3
$\lambda$ [W/cmK]	5	5	5	1.5	0.5
$T_{\text{melt}}$ [°C]	2830	2830	2830	1420	1240

<sup>1</sup>The melting point refers to the temperature at which a solid changes its state to liquid at atmospheric pressure.

Today, only 4H- and 6H-SiC polytypes are available commercially as substrate materials. Among the hexagonal polytypes, 4H-SiC is the most promising polytype being already implemented in various applications, such as high-voltage MOSFETs [16], [17], and is thus the focus of this thesis. 4H-SiC has the stacking sequence ABAC. The layer structure of 4H-SiC is shown in Figure 1.1.

The typically used notation system for crystallographic planes, also known as faces, are Miller indices [18]. For the cubic crystal three Miller indices,  $h$ ,  $k$ , and  $l$ , are used to describe directions and planes in the crystal. These are integers with the same ratio as the reciprocals of the intercepts with x-, y-, and z-axis, respectively.  $h$ ,  $k$ , and  $l$  denote the family of planes orthogonal to  $hb_1 + kb_2 + lb_3$ , where  $b_1$ ,  $b_2$ , and  $b_3$  are the reciprocal lattice vectors. Correspondingly, the three primitive lattice vectors which define the unit cell are  $a_1$ ,  $a_2$ , and  $a_3$ .

For hexagonal structures, however, four Miller indices are commonly used, denoted  $h$ ,  $k$ ,  $i$ , and  $l$ , which must obey the constraint  $h + k + i = 0$ . Correspondingly, four primitive lattice vectors  $a_1$ ,  $a_2$ ,  $a_3$ , and  $c$  are defined for the hexagonal unit cell. The sum of the reciprocal intercepts with  $a_1$ ,  $a_2$ , and  $a_3$  is zero. The angle  $\gamma$  between the  $a$ -vectors is  $120^\circ$ , whereas the  $c$ -vector is perpendicular to the plane of the  $a$ -vectors. A representative selection of basic planes as examples of determining Miller indices is shown in Figure 1.2. In the case of 4H-SiC the four commonly investigated crystallographic faces are the  $(0001)$  Si-,  $(000\bar{1})$  C-,  $(1\bar{1}00)$  m-, and  $(11\bar{2}0)$  a-face, shown in Figure 1.3. Despite the fact that all SiC polytypes chemically consist of 50% carbon atoms bonded with covalent (i.e., molecular) bonds to 50% Si atoms, each SiC polytype has its own distinct set of physical properties [19].

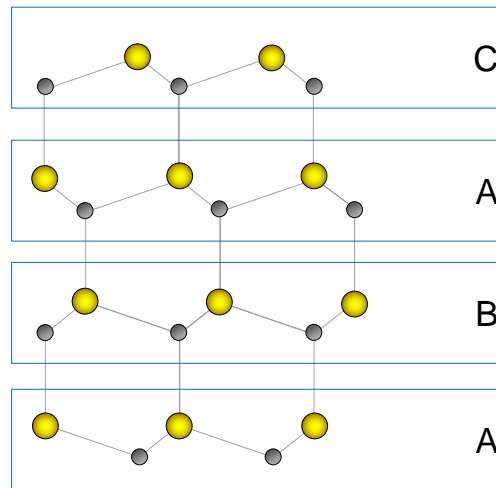


Figure 1.1: Cross-section of a basic cell of 4H-SiC with the stacking sequence ABAC. The yellow and gray spheres represent Si and C, respectively.

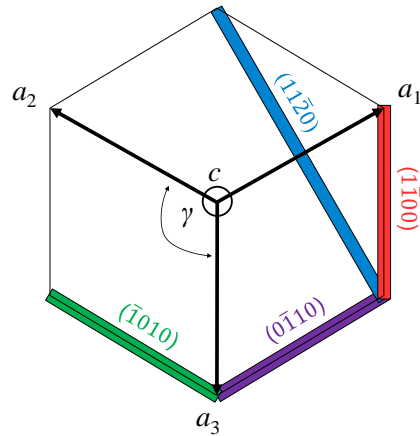


Figure 1.2: Examples of Miller indices for a hexagonal crystal structure, showing a representative selection of basic planes:  $(\bar{1}010)$  (green),  $(0\bar{1}10)$  (violet),  $(1\bar{1}00)$  (red), and  $(11\bar{2}0)$  (blue square).  $a_1$ ,  $a_2$ ,  $a_3$ , and  $c$  are the primitive lattice vectors and  $\gamma = 120^\circ$  is the angle between the  $a$ -vectors. The vector  $c$  is perpendicular to the  $a$ -vectors and points into the drawing plane.

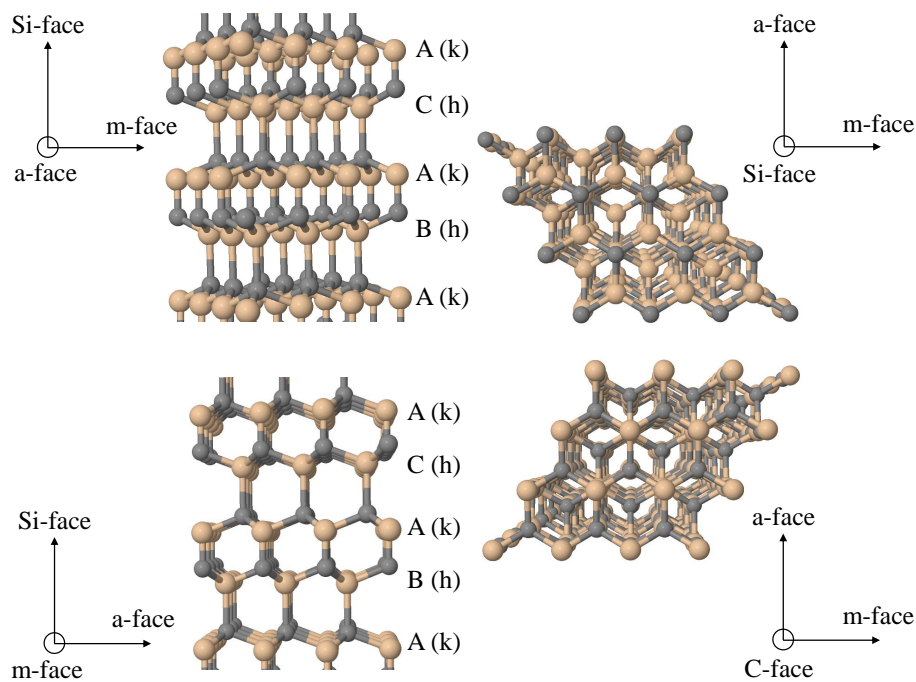


Figure 1.3: 3D schematic illustrations of various perspectives of a 4H-SiC polytype with the stacking sequence ABAC. The brown spheres represent Si atoms, the gray spheres C atoms, and the arrows show directions towards corresponding crystallographic faces. The Miller indices are: Si-face  $(0001)$ , C-face  $(000\bar{1})$ , m-face  $(1\bar{1}00)$ , and a-face  $(11\bar{2}0)$ . h and k stand for the hexagonal and cubic lattice sites, respectively.

### 1.1.2 Physical Properties

The properties of SiC make it the foremost semiconductor material for short wavelength optoelectronic, high-temperature, radiation resistant, high-power, and high-frequency electronic devices [20]. SiC-based devices can operate at high temperatures without suffering from intrinsic conduction effects, because of its wide-bandgap. SiC can withstand electric fields five to twenty times larger than Si or GaAs without undergoing avalanche breakdown [21]. This high breakdown electric field allows the devices to be closer together, providing high device packing density for integrated circuits. SiC is in addition an excellent thermal conductor, e.g., at room temperature (300 K) it has a three to thirteen times higher thermal conductivity than Si [22]. The high thermal conductivity enables SiC-based devices to operate at extremely high power levels whilst still being able to dissipate the large amounts of generated excess heat. SiC devices can operate at high frequencies, such as radio and microwave frequency ranges, due to the larger saturated electron drift velocity, which is two to two-and-a-half times larger than that of Si [23]. Comparisons of the bandgap, breakdown field, thermal conductivity, melting point, and saturation velocity of Si, GaN, GaAs, 4H-SiC, and 6H-SiC are shown in Figure 1.4.

The arrangement of next neighbors in the lattice is the same for all SiC polytypes, but crystallographic nonequivalent lattice sites exist in different polytypes. Thus, electronic properties, such as effective mass, carrier mobility, and bandgap, vary between different SiC stacking sequences and crystal orientations. Different polytypes have profound effects on the material properties, for example, the bandgap changes from 3.2 eV (4H-SiC) to 2.4 eV (3C-SiC). Some of the SiC properties are anisotropic, i.e., direction-dependent with respect to the crystal orientation. One example is the electron mobility which is in the case of 6H-SiC  $60 \text{ cm}^2/\text{Vs}$  parallel to the  $c$ -axis and  $400 \text{ cm}^2/\text{Vs}$  perpendicular to the  $c$ -axis. The low anisotropy of the electron mobility in 4H-SiC is one of the primary reasons for the emerging popularity of 4H-SiC, compared to 6H-SiC which has an extremely high anisotropic electron mobility.

Dopants in SiC can be incorporated into energetically nonequivalent cubic (k) or quasi-hexagonal (h) lattice sites, as shown in Figure 1.5. Hall measurements have yielded two donor levels upon the occupancy site in 6H-SiC, i.e., the hexagonal site is 85 meV and the cubic site is 140 meV. In 4H-SiC the donor levels of nitrogen (N)-doped SiC are 50 meV and 92 meV for hexagonal and cubic sites, respectively. For phosphorus (P)-doped SiC the donor levels are 54 meV and 93 meV for hexagonal and cubic sites, respectively [10]. The fact that most dopant levels are deeper than those found comparably in Si explains the partial carrier freeze-out in SiC at room temperature, since the thermal energy is only  $\approx 25.9 \text{ meV}$  at 300 K. In contrast, for p-type aluminium (Al)-doped SiC, an average acceptor energy level in the range of 200 to 240 meV is found for all polytypes. Other p-type dopants such as boron (B) have deeper acceptor levels ( $\approx 300 \text{ meV}$ ), but are not commonly used.

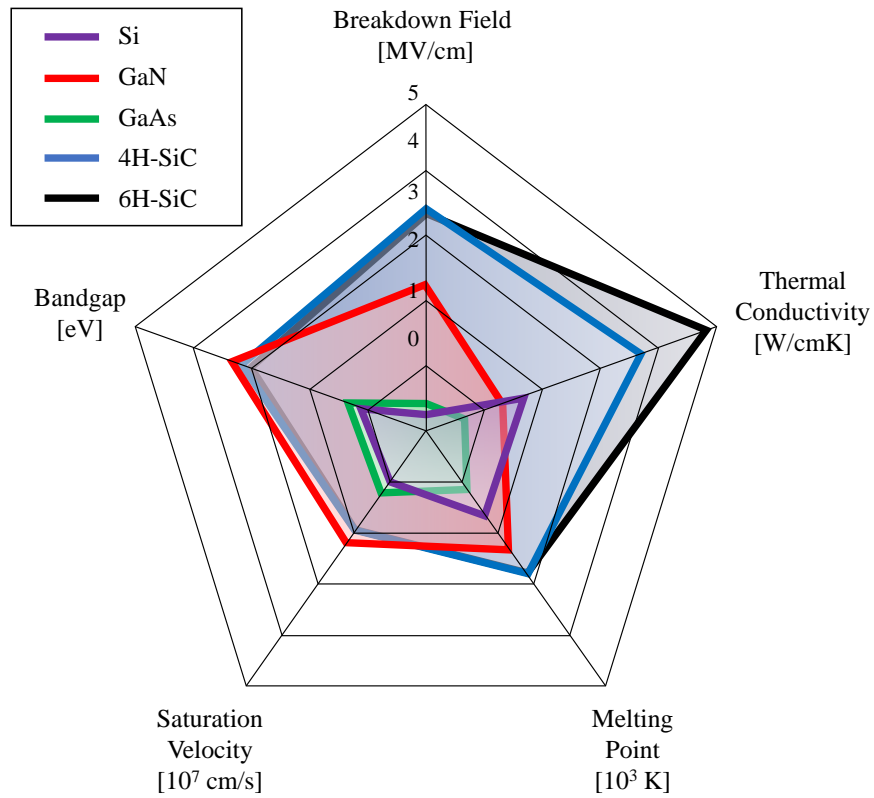


Figure 1.4: Comparison of relevant material properties of Si (violet), GaN (red), GaAs (green), 4H-SiC (blue), and 6H-SiC (black line).

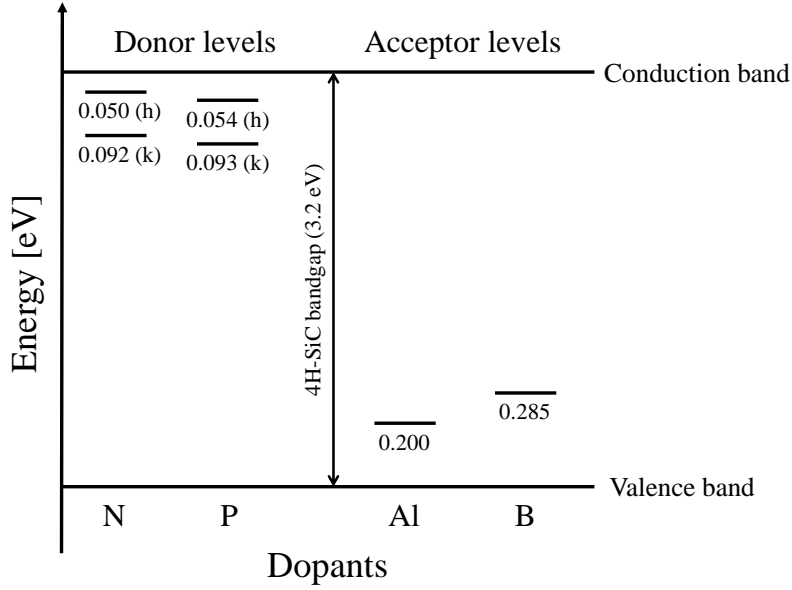


Figure 1.5: Diagram of the common dopants in SiC showing the donor and acceptor energy levels. h and k stand for the hexagonal and cubic lattice sites, respectively.

The effective mass of an electron or a hole is usually stated in units of the rest mass of an electron  $m_0 = 9.11 \cdot 10^{-31}$  kg. In these units the effective mass of electrons or holes is commonly in the range from 0.01 to 10, but can be as high as 1000 for exotic heavy fermion materials [24]. The experimental and theoretical values of the longitudinal and transverse effective mass of electrons and holes in SiC are still diverging across the literature for various polytypes and directions [1]. However, typically used values for calculating carrier concentrations are based on Hall effect analyses: The effective mass of electrons at 300 K for 4H-SiC is  $0.4m_0$  [25] and for 6H-SiC  $0.6m_0$  [26]. The effective mass of holes at 300 K for 4H-SiC is  $2.6m_0$  and for 6H-SiC  $2.8m_0$ . These differences clearly show that the effective mass of the electrons and holes are polytype-dependent.

All of the electrical properties of 4H- and 6H-SiC are summarized in Table 1.3. For comparison the properties of Si are shown as well. The major SiC polytypes exhibit advantages and disadvantages in basic material properties compared to Si. However, the main advantages of SiC over Si are particularly the thermal conductivity, the electrical breakdown strength, and the bandgap, which all together allow for higher temperature, frequency, and voltage operation of SiC-based devices.

Table 1.3: Comparison of electrical properties of common SiC polytypes, SiC anisotropy, and Si.  $E_g$  is the bandgap,  $\varepsilon_s$  the relative dielectric constant,  $E_B$  the breakdown field,  $\lambda$  the thermal conductivity,  $n_i$  the intrinsic carrier concentration,  $\mu_n$  the electron mobility,  $\mu_p$  the hole mobility,  $E_D$  the ionization energy of donors,  $E_A$  the ionization energy of acceptors,  $M_C$  the number of equivalent minima in the conduction band,  $m_e^*$  the effective mass of an electron,  $m_h^*$  the effective mass of a hole, and  $m_0 = 9.11 \cdot 10^{31}$  kg the electron rest mass.  $\parallel$  and  $\perp$  refer to parallel and perpendicular directions, respectively, and k and h refer to cubic and hexagonal lattice sites.  $\mu_n$  and  $\mu_p$  are measured at donor and acceptor concentration  $10^{16}$  cm $^{-3}$ ,  $E_B$  at donor concentration  $10^{17}$  cm $^{-3}$ , and  $m_e^*$  and  $m_h^*$  at temperature 300 K [1], [10], [25], [26], [27], [28], [29], [30].

Property	4H-SiC	6H-SiC	Si
$E_g$ [eV]	3.2	3.0	1.12
$\varepsilon_s$	9.7	9.66	11.9
$E_B$ [MV/cm]	$\parallel$ $c$ -axis: 3.0 $\perp$ $c$ -axis: 1.0	$\parallel$ $c$ -axis: 3.2 $\perp$ $c$ -axis: 1.0	0.3
$\lambda$ [W/cm K]	3.7	4.9	1.31
$n_i$ [cm $^{-3}$ ]	$5.0 \cdot 10^{-9}$	$1.6 \cdot 10^{-6}$	$9.65 \cdot 10^9$
$\mu_n$ [cm $^2$ /Vs]	$\parallel$ $c$ -axis: 900 $\perp$ $c$ -axis: 800	$\parallel$ $c$ -axis: 60 $\perp$ $c$ -axis: 400	1430
$\mu_p$ [cm $^2$ /Vs]	115	90	480
Donor: $E_D$ [meV]	N: 50 (k), 92 (h) P: 54 (k), 93 (h)	N: 85 (k), 140 (h) P: 80 (k), 110 (h)	P: 45 As: 54
Acceptor: $E_A$ [meV]	Al: 200 B: 285	Al: 240 B: 300	Al: 67 B: 45
$M_C$	3	6	6
$m_e^*$	$0.4m_0$	$0.6m_0$	$0.2m_0$
$m_h^*$	$2.6m_0$	$2.8m_0$	$0.4m_0$

### 1.1.3 Device Applications

Several SiC semiconductor devices, utilized mostly in high-power applications [31], [32], [33], are commercially available, such as Schottky barrier diodes (SBDs), junction-gate field-effect transistors (JFETs), and MOSFETs, shown in Figure 1.6. The first commercial 1200 V JFETs were introduced in 2008, followed by the first commercial 1200 V MOSFETs in 2011. In the same timeframe some companies started implementing bare SiC Schottky diode chips into their power electronic modules. In fact, SiC SBDs are widely used in IGBT power modules and power factor correction circuits.

Power devices and electronics are critical components which regulate the delivered and used power. For the generation of energy sources, such as wind and solar energy, SiC-based devices convert energy for households and industries. In hybrid or electric vehicles power devices manage the electricity running through electric motors and for data centers the same devices control power usage by the large scale computer systems. As an exemplary outlook, performance gains from SiC electronics could enable the public power grid to handle increased consumer electricity demand without building additional generation plants, and improve power quality and operational reliability through smart power management [27].

What makes SiC-based power electronics so attractive is the fact that for a given blocking voltage the doping concentration can be almost one hundred times higher than in Si-based devices. This results in a high blocking voltage at a low on-resistance, which is crucial for high-power applications, since less heat will be generated as the on-resistance decreases, reducing the system's thermal load and increasing overall efficiency.

In the area of future power applications, GaN is another important wide bandgap material which shows a great promise in device performance improvements. There is a great deal of ongoing discussions about differences in advances and challenges between SiC and GaN. On one hand, GaN is seen as the competitor to SiC, but on the other hand, it is believed that each of them will settle into its own niche [34], [35]. Currently many companies and research institutions rather focus on SiC due to the following reasons: 1) SiC devices fit very well into the markets and applications as are known from Si technology. 2) SiC power device technology is more mature than GaN. 3) Path to profitable growth seems shorter with SiC than GaN. 4) SiC offers the possibility of producing MOSFETs, while GaN does not.

However, there are a few difficulties inherent in manufacturing SiC-based electronic components, with the elimination of defects being the foremost problem. These defects result in poor reverse blocking performance in components made of SiC crystals [36]. In addition to this crystal quality problem, difficulties in the interface of SiO<sub>2</sub> with SiC have hindered the advance of both SiC-based power MOSFETs and IGBTs.

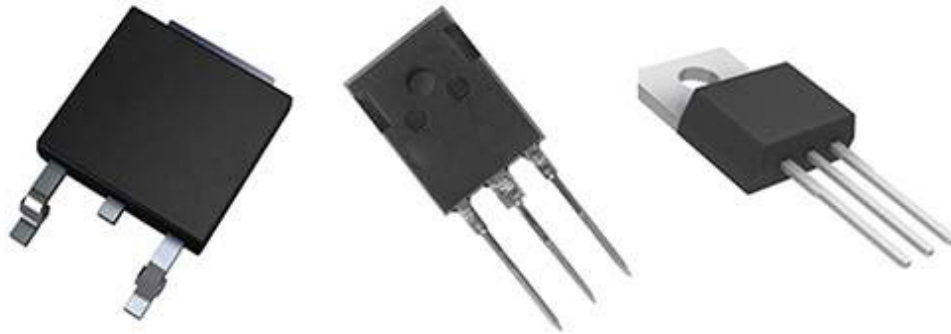


Figure 1.6: Examples of commercially available SiC devices: JBS (left), JFET (center), and MOSFET (right).

The principal optoelectronic applications for SiC are low-intensity blue light emitting diodes (LEDs) and substrates for GaN-based high-intensity blue LEDs or laser diodes [37]. In fact, electroluminescence was first discovered in 1907 using a crystal of SiC together with a cat's whisker detector. After some years of development SiC LEDs were commercially produced worldwide, i.e., yellow SiC LEDs in the 1970s and blue SiC LEDs in the 1980s. However, with the introduction of GaN LEDs, which can produce ten to hundred times brighter emissions, SiC LED production was interrupted. Nevertheless, SiC is still popular as a substrate for GaN-based devices and mostly utilized for high-temperature, -voltage, and -frequency applications.

High-temperature SiC-based devices are developed for aircraft and automotive engine sensors, jet engine ignition systems, transmitters for deep well drilling, and a number of industrial process measurement and control systems [38], [39]. The use of electromechanical controls which are capable of harsh-ambient operation will enable substantial jet-aircraft weight savings, reduced maintenance, reduced pollution, higher fuel efficiency, and increased operational reliability [40]. SiC semiconductor devices can function at much higher temperatures than Si devices, due to the wide-bandgap and low intrinsic carrier concentration of SiC. The intrinsic carrier concentration increases exponentially with temperature [27], thus the undesired junction reverse-bias leakage current becomes unacceptably large. In this case the semiconductor device's operation is overcome by uncontrolled conductivity, when the intrinsic carrier concentration exceeds device doping levels. Therefore, very small intrinsic carrier concentrations of SiC enable junction temperatures and device operation temperatures above 800°C and 600°C, respectively [36], [41].

High-voltage SiC-based devices have tremendous potential due to the high electric breakdown field in the range of  $1 \cdot 10^6$  V/cm to  $4 \cdot 10^6$  V/cm and high thermal conductivity in the range of 2 W/cm K to 5 W/cm K of SiC [42]. The high breakdown field of SiC-based devices enables much higher doping levels and thinner layers for a particular voltage, compared to Si devices. This results in up to a three hundred times lower on-resistance for SiC unipolar devices compared to equivalent Si devices.

Moreover, the high breakdown field and wide-bandgap allow for much faster power switching devices. High-frequency SiC-based devices are being used in power supplies, cellular phone base stations, phased array radar systems, and lightweight radio frequency and microwave transmitters, where conventional devices cannot operate adequately due to high power densities and high temperature demands [43]. However, the SiC technology faces many challenges in fabrication processes, particularly due to the unique material properties of SiC.

## 1.2 Device Fabrication

Semiconductor device fabrication is a process to create ICs present in everyday electronic devices, such as computers, mobile phones, televisions, radios, cameras, washing machines, lights, vehicles, and many more. Fabrication processes are a sequential set of tasks utilizing photolithographic and physical as well as chemical processing techniques during which the 3D IC structures are gradually created on a semiconductor wafer [44]. The processes are performed in highly specialized facilities, known as fabs. The device fabrication process times are very cost-intensive and lengthy, i.e., the entire manufacturing process takes approximately six to eight weeks and can in certain circumstances take up to fifteen weeks [44].

The previously mentioned step-by-step and layer-upon-layer method of producing ICs in a wafer is called planar technology. A big advantage of this technology is that each fabrication step is applied to the entire wafer. Therefore, it is possible to interconnect many devices with high precision and to fabricate many ICs on one wafer at the same time. Thus, from an economical perspective, it is highly beneficial to reduce the area of each IC, i.e., reduce the size of the devices and interconnects, in order to get more chips per wafer and thus reduce costs [44]. For example, over the last decades the node sizes decreased from 10  $\mu\text{m}$  in 1971 to 10 nm in 2017 [45], which is a decrease of three orders of magnitude, meaning that on the same wafer size approximately  $10^6$  more chips can be produced via the same process. This development was projected by Moore's law [46], [47], [48], which states that the number of transistors on a dense IC for the same costs doubles every 18 to 24 months.

The most commonly used processing steps for IC fabrication are photolithography, etching, deposition, ion implantation, thermal oxidation, annealing, and diffusion [44], [49]. The manufacturing steps involved in the fabrication of semiconductor devices are briefly discussed in the following sections. As an example of a device fabrication, simplified processing steps of a SiC MOSFET are schematically depicted in Figure 1.7.

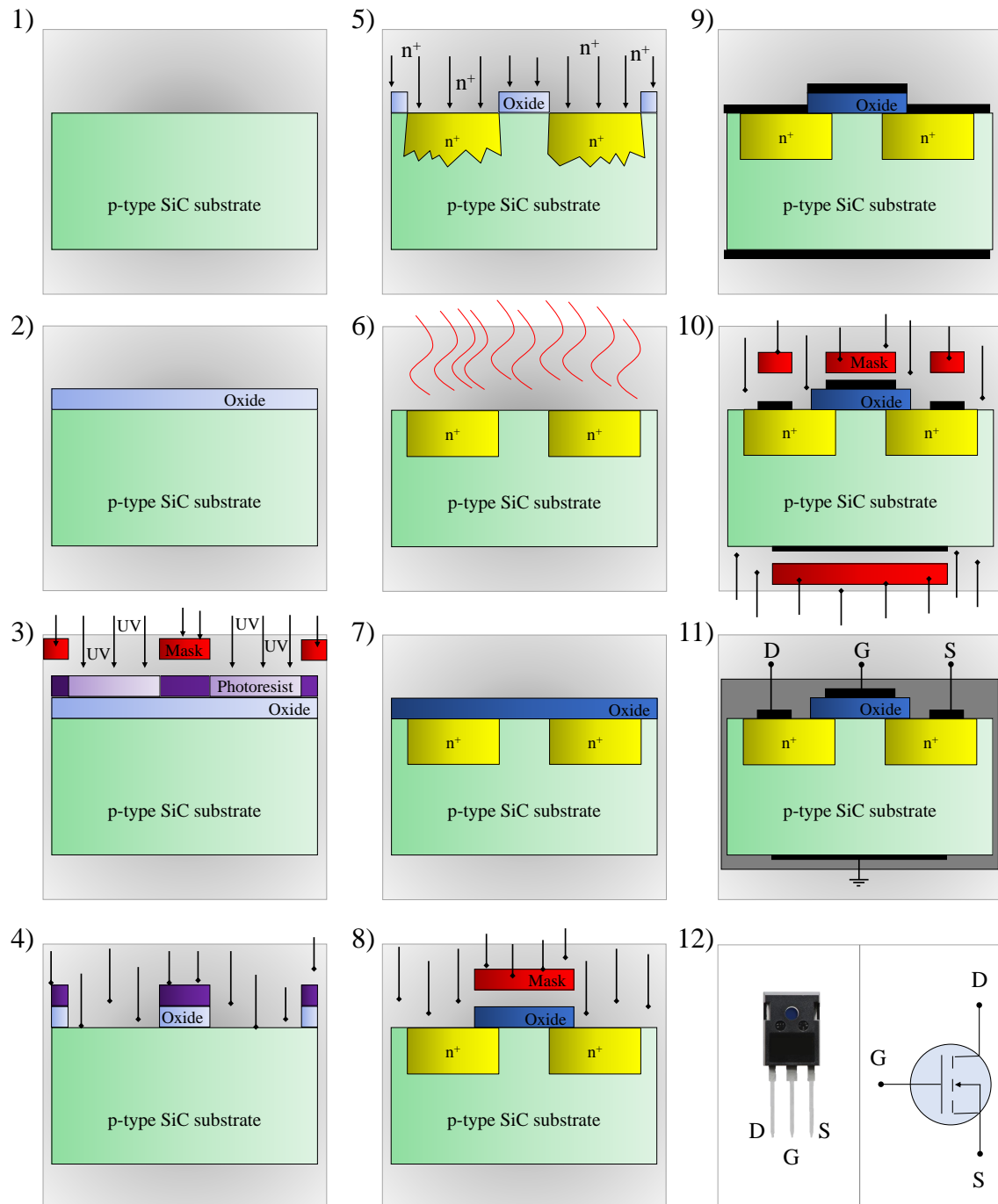


Figure 1.7: Schematic summary of the major processing steps in the fabrication of a SiC MOSFET: 1) p-type SiC substrate wafer, 2) thermal oxidation, 3) photolithography, 4) oxide etching, 5)  $n^+$  ion implantation, 6) annealing and diffusion, 7) thermal oxidation, 8) oxide etching, 9) metal deposition, 10) metal etching, 11) dicing and packaging, and 12) final device (left) and device's circuit scheme (right). D, S, and G stand for drain, source, and gate, respectively.

The fabrication of a SiC MOSFET begins with the SiC substrate wafer, followed by thermal oxidation, photolithography, and etching in order to create a mask for ion implantation. In this way, the oxide is produced selectively, which protects particular areas from ion implantation. The rest of the substrate is implanted with dopants and annealed in order to increase the electrical activity of implanted regions, to repair the crystal lattice, and to reduce the trap density. After that, a high quality oxide is grown on the surface and selectively removed by photolithography and etching to create a gate oxide for the device. Afterwards a metal is deposited and etched on the top and the bottom of the device to create ohmic contacts for the source, gate, and drain. Finally, the device is diced from the wafer and packaged in order to protect it from the external environment and to provide connections to drain, gate, and source for the use in external circuits [1], [49].

### 1.2.1 Photolithography

Photolithography, also known as optical or UV lithography, is a process to pattern parts of a thin film or the bulk of a semiconductor substrate. It is a photographic process by which a light sensitive polymer, called a photoresist, is exposed and developed to ultimately form 3D relief images on the substrate using a geometric pattern, called a mask [44]. In general, the ideal photoresist image has the exact shape of the intended pattern given by the mask in the plane of the substrate, with vertical walls through the resist. Thus, the final resist pattern is binary, i.e., parts of the substrate are covered with resist while other parts are not. This binary pattern is needed for pattern transfer since the parts of the substrate covered with resist will be protected from etching, ion implantation, or other pattern transfer mechanisms.

The general sequence of processing steps for a typical photolithography process is 1) substrate preparation, 2) photoresist spin coat, 3) pre-bake, 4) exposure to ultraviolet light, 5) post-exposure bake, 6) development, i.e., making photoresist soluble, and 7) post-bake [44], [49]. A resist strip is the final operation in the lithographic process, after the resist pattern has been transferred onto the underlying layer. This sequence is generally performed on several tools linked together into a contiguous unit called a lithographic cluster. In common ICs a modern MOSFET wafer will go through the photolithographic cycle up to fifty times [44].

### 1.2.2 Etching

Etching is a process to physically or chemically remove layers from the surface of a wafer during device fabrication. In order to generate the desired patterns and geometries on a wafer, several etching steps must be performed before the wafer design is complete [44]. Patterns are controlled via protecting materials which resist etching.

Commonly the protective material is a photoresist which is patterned by photolithography (cf. Section 1.2.1).

Etching techniques exist in several varieties, i.e., selective or non-selective and isotropic or anisotropic [44], [49]. If the etching step is intended to make a cavity in a material, the depth of the cavity can be controlled using the etching time and the known etch rate. Many times etching must entirely remove the top layer of a multilayer structure, without damaging the underlying or masking layers. The etching ability to remove one particular material while partly or fully preserving another is selectivity which depends on the ratio of the etch rates for different materials. Some etches undercut the masking layer and form cavities with sloping sidewalls. The distance of undercutting is called bias. Etchants with large bias are called isotropic, because they erode the substrate equally in all directions. Modern processes greatly prefer anisotropic etches, because they produce sharp, well-controlled features [50].

The two fundamental types of etching techniques are liquid-phase (wet) and plasma-phase (dry) etching [44], [49]. The dry etching uses a plasma process where ions and neutral radicals are accelerated towards the surface to remove certain materials. The plasma process is typically anisotropic, where the etch rate is mainly in the direction of the accelerated ions [44]. Wet chemical processes are typically isotropic, i.e., they etch in all directions with the same rate. However, both dry and wet etching can be anisotropic by causing an etch rate variation with different material crystal orientations [49].

### 1.2.3 Deposition

Deposition is a process that grows, coats, or in any way transfers a material onto the wafer. Various deposition techniques are available today, such as physical vapor deposition (PVD), chemical vapor deposition (CVD), electrochemical deposition (ECD), molecular beam epitaxy (MBE), and atomic layer deposition (ALD) [49], [50]. PVD and CVD are currently the most commonly used techniques in the semiconductor industry.

PVD refers to a variety of vacuum deposition methods which can be used to produce thin films and coatings. It is characterized by a process in which a material changes from the condensed phase to a vapor phase and back to a thin film in condensed phase. No chemical reaction occurs at the deposition site, but rather a material is released from a source and transferred to a substrate [49]. The most commonly used PVD techniques are sputtering and evaporation [44]. Common industrial coatings applied by PVD are titanium nitride (TiN), zirconium nitride (ZrN), chromium nitride, (CrN), and titanium aluminium nitride (TiAlN).

CVD, on the other hand, refers to a chemical process used to produce high-quality and high-performance solid materials. In typical CVD techniques, a wafer is exposed to one or multiple volatile precursors, which react and decompose on the substrate surface to

produce the desired deposit. A high deposition temperature is usually required in order to drive the reaction where the resulting film has a very good step coverage and better uniformity, compared to PVD. Industry-related CVD processes include deposition of materials in various forms, such as monocrystalline, polycrystalline, amorphous, and epitaxial [49]. The most common deposition materials are SiO<sub>2</sub>, C, germanium (Ge), tungsten (W), and titanium (Ti).

### 1.2.4 Oxidation

Oxidation is a process which generates a layer of oxide, usually SiO<sub>2</sub>, on the surface of a semiconductor wafer. The oxidation is typically performed at temperatures above 800°C in oxidation furnaces which can accept several wafers at the same time [49]. The orientation of the semiconductor crystal affects the oxidation growth rate as well as the oxide cleanness [1]. An oxide can be either thermally oxidized or chemically deposited [49]. In cases where the oxide must be grown on non-Si-based surfaces, only deposition can be used, because non-Si materials are unable to form SiO<sub>2</sub>. The chemical deposition is usually performed using tetraethyl orthosilicate or silane pyrolysis [50]. However, the thermal oxidation of any variety is commonly preferred, because it produces a higher-quality oxide with a much cleaner interface, i.e., less interface defects, than the chemical deposition [44].

SiO<sub>2</sub> layers of precisely controlled thicknesses are produced during IC fabrication by exposing a semiconductor to either oxygen gas (O<sub>2</sub>) or water vapor (H<sub>2</sub>O) at elevated temperatures. In either case the oxidizing species diffuse through the existing oxide and react at the interface, e.g., SiC-SiO<sub>2</sub>. SiO<sub>2</sub> is used for several purposes, ranging from serving as a mask controlling dopant implantation to serving as the most critical component in the MOSFET technology, i.e., the gate oxide [1], [50]. The oxidation process is discussed in more detail in the Chapter 2.

### 1.2.5 Ion Implantation

Ion implantation is a process which introduces dopants into a material and thereby changes its physical, chemical, or electrical properties. In this process, ions of an element, such as Al, B, P, or N, are accelerated into a solid target like Si or SiC at relatively low temperatures (below 300°C) [44]. Ion implantation equipment typically consists of 1) an ion source, where ions of the desired element are produced, 2) an accelerator, where the ions are electrostatically accelerated to a high energy, and 3) a target chamber, where the ions impinge on a target, which is the material to be implanted. Therefore, ion implantation is considered a special case of particle radiation. Each ion is typically a single atom or molecule. The total amount of implanted material in a target is the integral over time of the ion current, also known as the dose, measured commonly in cm<sup>-2</sup> [49].

Dopant ions are generally created from a gas source, for purity reasons, and are afterwards accelerated towards the wafer to penetrate into the crystal lattice. This process generates a charge carrier in a semiconductor for each dopant atom in the lattice [44]. The generated charge carrier can be an electron or a hole, depending on the type of dopants, i.e., donors or acceptors. Doping an intrinsic semiconductor with donor impurities produces n-type semiconductors, which have a large electron concentration after implantation and are negatively charged, thus the term n, which stands for negative. On the other hand, p-type semiconductors are created by doping an intrinsic semiconductor with acceptor impurities and thus have a large hole concentration, and are positively charged, thus the term p, which stands for positive [49].

The crystal structure of a target can be damaged or even destroyed by the energetic collision cascades with ions of high energies. Moreover, the desired carrier concentration is typically not achieved after the implantation, due to defects and clusters which occur during the implantation process. Therefore, post-implantation annealing steps are necessary in order to repair lattice damage and increase electrical activation of the implanted species [1], [50].

### 1.2.6 Annealing and Diffusion

Annealing is a heat treatment of wafers, which alters the physical and chemical properties of semiconductors. In device fabrication typical techniques are furnace annealing (FA) and rapid thermal annealing (RTA) [44]. Both processes utilize high temperatures (commonly above 1000°C) in order to affect the semiconductors' electrical and chemical properties, i.e., activate and diffuse dopants, change substrate interfaces, densify deposited layers, change states of the grown films, and repair crystal lattice damage [50]. The main difference between FA and RTA is the timescale of the process, which is in the order of 10-60 minutes for FA and several seconds for RTA. Recently RTA is favored in the semiconductor industry, because the relatively long thermal cycle of FA causes dopants, especially B, to diffuse further than intended. It is important that during the thermal cycles the cooling of wafers must be slow to prevent dislocations and wafer breakage due to the thermal shock [44].

An alternative to ion implantation is diffusion which typically occurs during annealing steps. Charge carriers are introduced into a wafer via the diffusion of dopants from the surface into a semiconductor at relatively high temperatures (above 1000°C). The depth of the diffusion within a semiconductor is a function of the temperature and must be thus carefully executed so that the desired doping profile is not damaged by further processing steps which require high temperatures, e.g., oxidation [49]. One advantage of diffusion over ion implantation is that no damage is introduced to the lattice or the surface, since there is no ion bombardment. Another advantage is the ability to create very shallow and predictable charge concentration profiles. However, for SiC the diffusion of the common dopants is very low and cannot be conveniently used as a doping technique [1].

### 1.2.7 Dicing and Packaging

Wafer dicing is a process by which the dies, i.e., small blocks of functional circuits on a wafer, are separated from the wafer [44]. The dicing methods include breaking, mechanical sawing, or laser cutting and are typically automated to ensure precision, accuracy, and high throughput. Once a wafer is diced into individual dies, every die is packaged or placed on a circuit substrate [44], [49].

IC packaging is the final stage of the device fabrication, where the tiny blocks of functional circuits, i.e., dies, are each encapsulated in a supporting case which prevents physical damage and corrosion. Packages also include contact pins which are used to connect the produced devices to external circuits, e.g., a central processing unit must be connected to a motherboard [44], [49]. Larger devices, intended particularly for high-power applications, are installed in carefully designed heat sinks so that they can dissipate hundreds or thousands of watts of waste heat produced in a device [50].

## 1.3 TCAD

Technology computer-aided design (TCAD) mimics semiconductor device fabrication, design, and operation by modeling, analysis, and simulation approaches based on fundamental physics or empirical observations. One of the most important uses of TCAD tools is to explore new device technologies, where many exploratory simulations are performed in order to give the device engineers a better understanding of the possible benefits and drawbacks of a potential technology.

Conventional industrial development of new devices based on experimental evaluations involves several iterations of trial and error in fabrication, until a specified goal in terms of design conditions is reached. Therein lies the importance of TCAD, that is to substantially decrease development time and costs of a new semiconductor technology. The fact that computer resources are becoming cheaper, compared to drastically increasing costs of experimental investigations, is further underlining the importance of TCAD-based predictions [51]. Therefore, TCAD plays a crucial role in the evolution of semiconductor technologies by replacing many cost- and time-intensive experiments with computer simulations.

The first numerical modeling was suggested in 1964 for a 1D bipolar transistor [52]. This approach was further developed and applied to PN-junction diodes and junction isolated, double-diffused, and bipolar transistors in the late 1960s. These devices and technology were the basis of the first ICs, but had many scaling issues and process variabilities, i.e., when various devices of the identical fabrication process exhibit significant differences in the electrical or mechanical properties [51]. With the development of electronic devices and ICs in the past decades, TCAD evolved along the way into a very strong branch of electronic design automation. The fast-moving progress

in semiconductor technologies thus demands continued research in all areas related to TCAD in order to keep up with the rapid developments. The individual simulation steps involved in TCAD are process, device, and circuit simulations and are discussed in the following.

### 1.3.1 Process Simulations

The accuracy and robustness of the process technology, its variability, and operating conditions of the ICs are critical in determining performance, yield, and reliability of devices. Therefore, process simulations are necessary to accurately predict, for example, the active dopant distribution, the stress distribution, and the device geometry. The development of models and methods for a better representation of the actual physical processes is the key driver for continued advances in process simulations. Model development is typically based on fundamental physics and/or on empirical observations. Process simulation is thus an interdisciplinary field where scientists from chemistry, physics, computer science, mathematics, and engineering collaborate in developing new models involved in predicting the fabrication of various semiconductor devices.

Industries typically prefer simple modeling approaches which approximate the desired properties and simultaneously require negligible computational efforts, i.e., empirical modeling approaches. In order to obtain reliable parameters for empirical modeling it is necessary to calibrate the parameters relative to experimental data. In summary, the ultimate goal of process simulations is modeling and simulation of the fabrication processes, such as oxidation, implantation, and annealing, in order to provide doping profiles and geometries for consecutive device simulations.

### 1.3.2 Device Simulations

In order to be able to predict device characteristics, models for the behavior of electrical devices are necessary. These models, i.e., compact and physics-driven models, are at the core of device simulations, which require device geometries and doping levels as input. Device simulations are particularly useful for predictive parametric analysis of novel device structures, i.e., conducting vast parameter studies to obtain, for example, current density, threshold voltage, on-resistance, and breakdown voltage. Device modeling and simulation enables to obtain a better understanding of conceived properties and behavior of the semiconductor devices and to improve their reliability and scalability. Furthermore, device simulation increases development speed and reduces risks as well as uncertainties. The final output of device simulations is the electrical characteristics of a device. The obtained device properties are forwarded to circuit simulations, which predict the behavior of the final products, such as amplifiers, filters, inverters, and rectifiers.

### 1.3.3 Circuit Simulations

Circuit simulations use mathematical models with accurate modeling capabilities to replicate the behavior of an actual circuit, i.e., combination of electronic components, such as resistors, transistors, capacitors, inductors, and diodes. The ultimate goal of circuit simulations is to improve the design and the overall operation efficiency of circuits before they are actually fabricated. Typical circuit simulation types are: Analog, digital, mixed-signal, and piecewise linear, which differ in their underlying algorithms. A circuit simulator can be used for various types of simulations, such as: transient, noise, and Monte Carlo analysis, which all provide different kinds of information about the circuit.

### 1.3.4 TCAD Tools

TCAD simulation tools are critical to address the full complexity of semiconductor technologies including design rules, parasitic effects, operation in harsh environments, and more. Currently available tools include 1D, 2D, and 3D simulators and support a large variety of application scenarios along the entire TCAD simulation chain, starting from process simulations over device simulations and ultimately to circuit simulations. Current major suppliers of TCAD tools are: Cogenda, Crosslight, Global TCAD Solutions, Silvaco, Synopsys, and Tiberlab. In this thesis, Silvaco's Victory Process [53] and Victory Device [54] simulators are used.

Victory Process is a general purpose process simulator for applications including etching and deposition, implantation, annealing, and stress simulation. Etching and deposition can be performed via geometrical models for fast structure prototyping or with physical models for detailed process analysis. The simulator provides fast analytical models as well as a very accurate Monte Carlo method for ion implantation. Annealing steps include a comprehensive set of doping diffusion models and a hierarchy of oxidation models.

Victory Device is a simulator, which is used to predict electrical, optical, and thermal behavior of semiconductor devices. It provides a physics-based modular and extensible platform to analyze direct and alternating current as well as the time domain responses for devices manufactured with various materials. It offers an advanced tetrahedral meshing engine for fast and accurate discretization of complex 3D geometries for rapid-prototyping.

## 1.4 Research Goals

The significant progress of SiC material development achieved in recent years opened the possibility to utilize unique features of SiC-based devices. However, advanced and SiC-specific modeling techniques have to be developed in order to optimize device properties and device fabrication steps. The goal of this work is, therefore, to introduce novel modeling approaches and extend simulation capabilities of thermal oxidation and dopant activation for SiC-based devices. In particular:

1. Oxidation growth rate coefficients for certain crystal orientations are missing or are inconsistent across the literature. A full set of oxidation coefficients will enable accurate simulations of SiC oxidation.
2. In order to be able to perform multi-dimensional simulations of SiC oxidation a direction-dependent oxidation model is necessary. A novel method, besides the currently available oxidation models, is needed in order to obtain unknown oxidation growth rates for arbitrary crystal directions.
3. The SiC oxidation models, which are typically expressed as differential equations, depend on initial conditions. Therefore, a detailed investigation of the initial oxidation stages of SiC is required to accurately determine initial oxide thicknesses.
4. Beside the SiC oxidation challenges, an accurate prediction of doping profiles in SiC is currently not available. The temperature-dependent activation rate of dopants must be investigated and an accurate modeling approach must be found.
5. The activation of dopants is not at all trivial, but rather highly dependent on the process parameters such as total doping concentration, annealing time, ambient gas concentration, and implantation temperature. Therefore, an appropriate approach to include various doping dependences in simulations is necessary.

One of the biggest challenges of this work is the lack of available experimental data, which does not provide the whole picture needed for investigations. In addition, the physics behind oxidation and activation mechanisms is not fully understood and impossible to predict without further investigations. Several phenomena are purely SiC-specific, therefore, the chemical mechanisms, physical processes, and computational models cannot be directly inherited from other semiconductor materials.

### 1.4.1 Research Setting

The research presented in this work was conducted within the scope of the Christian Doppler Laboratory for High Performance Technology Computer-Aided Design. The Christian Doppler Association funds cooperations between companies and research institutions pursuing application-orientated basic research. In this case, the cooperation was established between the Institute for Microelectronics at the TU Wien and Silvaco Inc., a company developing and providing electronic device automation and TCAD software tools.

## 1.5 Outline

This thesis addresses in particular modeling and simulation challenges of the two important fabrication processes of SiC, i.e., thermal oxidation and electrical activation of dopants.

Chapter 2 reviews the thermal oxidation of SiC, starting with the characteristics, properties, and structure of SiO<sub>2</sub>, followed by the fundamentals of the oxidation mechanisms. Next, the oxidation models, i.e., the Deal-Grove model, Massoud's model, and the Si and C emission model, are described in detail. The core of this chapter discusses growth rate coefficients, fitting, and calibration as well as the parametric and explicit expression of the unique interpolation method. Process simulations utilizing the obtained parameters and the proposed interpolation method are presented as well. Finally, ReaxFF molecular dynamics simulations and analyses of the early stage of the SiC oxidation are presented.

Chapter 3 reviews the electrical activation of dopants in SiC, first introducing fundamentals of semiconductor physics, which is needed to obtain donor or acceptor concentrations from ionized impurity concentrations. Next, the activation models, i.e., activation ratio model, semi-empirical model, and transient model, are presented. Each of the models includes a mathematical description, calibrations relative to experimental data, characterization of methodology, and finally process simulations followed by device simulations to validate the results.

Chapter 4 provides conclusions.

## 2 Thermal Oxidation

This chapter discusses key contributions made to modeling and understanding of SiC oxidation mechanisms, in particular, oxidation growth rates, orientation-dependent interpolation method, and first principle simulations. But first, fundamentals of the thermal oxidation process are introduced in the following.

One of the essential steps in fabrication of electronic devices is thermal oxidation [1], which is a chemical process to produce ten to hundred nanometer thick oxide layers, usually SiO<sub>2</sub>, on the surface of a wafer. The produced SiO<sub>2</sub> layers find their application in insulating and protecting layers as well as gate oxides of MOSFETs. The oxidation technique forces an oxidizing agent to diffuse into the wafer at high temperatures (usually above 700°C) in an oxidizing environment, such as O<sub>2</sub>, steam, or nitric oxide (NO) [44]. A native oxide layer of a thickness of up to 2 nm rapidly forms on the surface. After this initial native oxide layer, the oxidation rate is significantly reduced and the oxidation effectively stops after a final thickness in the order of a few hundreds of nanometer is reached. The oxidation stops when oxygen molecules at particular oxidation temperatures do not have enough energy to diffuse through the formed oxide layer, which acts as a passivation layer for the oxidation process [49].

Thermal oxidation is accomplished using an oxidation furnace which provides the heat needed to elevate the oxidizing ambient temperature. A furnace typically consists of 1) a cabinet, 2) a heating system, 3) a temperature measurement together with a control system, 4) fused quartz process tubes, where the wafers undergo oxidation, 5) a system for moving process gases in and out of the process tubes, and 6) a loading station used for loading (or unloading) wafers into (or from) the process tubes. The heating system usually consists of several heating coils which control the temperature around the furnace tubes. The wafers are placed in quartz glassware known as *boats* which are supported by fused silica paddles inside the process tube. A boat can contain many wafers, typically 50 or more. The oxidizing agent (O<sub>2</sub> or steam) then enters the process tube through its source end, subsequently diffusing to the wafers where the oxidation occurs. Typically, an additional gas species (e.g., NO) is added to the oxidizing ambient in order to increase the quality of the grown oxide, i.e., to reduce the density of interface traps [1], [55]. A schematic representation of a thermal oxidation furnace is shown in Figure 2.1.

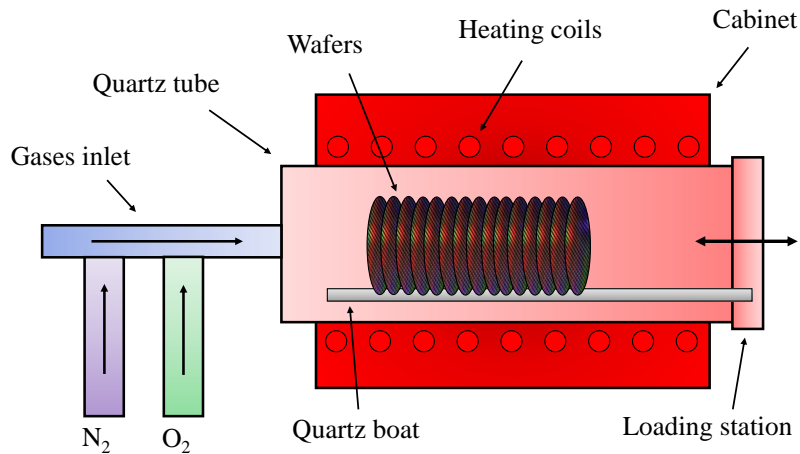


Figure 2.1: Schematic representation of a thermal oxidation furnace, which has control over the oxide growth conditions to ensure reproducibility and quality of the oxide layers.

$\text{SiO}_2$  layers can be also produced with various deposition techniques, e.g., CVD which is typically less expensive compared to thermal oxidation. However, for the deposition process it is extremely challenging to be able to accurately control deposition for oxide thicknesses below 10 nm. Another disadvantage is the poor electrical property of the interface between a deposited oxide layer and the underlying material (e.g., Si or SiC). In addition, the density of the deposited oxide is lower compared to one of the thermally grown oxide [44]. The details of the thermal oxidation mechanism and the properties of  $\text{SiO}_2$  are discussed in detail in the following sections.

## 2.1 Silicon Dioxide

$\text{SiO}_2$  offers many desired properties and advantages for semiconductor electronic devices, particularly MOSFETs.  $\text{SiO}_2$  layers can be grown thermally on many desired semiconductor materials (such as Si and SiC) and are resistant to most of the chemicals used in device fabrication processes [44]. Oxide layers can be in addition relatively easily patterned and selectively dry or wet etched. Commonly, oxides are used to prevent in- or out-diffusion of dopants or other impurities from the wafer [49].  $\text{SiO}_2$  has an indispensable thermal stability for process and device integration (up to  $1600^\circ\text{C}$ ). Furthermore,  $\text{SiO}_2$  is an excellent insulator with a wide-bandgap of  $\approx 8.9$  eV and a high dielectric strength of  $\approx 10^7$  V/cm [56]. The key properties of  $\text{SiO}_2$  are shown in Table 2.1. The bandgap of  $\text{SiO}_2$  is more than seven times larger compared to Si, which makes it very suitable for, e.g., dielectric isolation.

The structure of  $\text{SiO}_2$  is constructed of four oxygen atoms and a single Si atom in the centre of a tetrahedron. The length of a Si-O bond is normally  $1.62 \text{ \AA}$  and the distance between the oxygen atoms is  $2.62 \text{ \AA}$ . The distance between the two Si atoms, i.e., between the two unit cells, in a complete oxide structure is typically  $3.1 \text{ \AA}$ . The molecular structure of a single  $\text{SiO}_2$  molecule is shown in Figure 2.2.

Table 2.1: Relevant chemical and electrical properties of  $\text{SiO}_2$  including molar mass, melting point, thermal density, thermal conductivity, relative dielectric constant, and energy bandgap [56].

Molar Mass	60.08 g/mol
Melting Point	$1713^\circ\text{C}$
Thermal Density	$2.18 - 2.27 \text{ g/cm}^{-3}$
Thermal Conductivity	$3.2 \cdot 10^{-3} \text{ W/(cm K)}$
Relative Dielectric Constant	3.7 – 3.9
Dielectric Strength	$10^7 \text{ V/cm}$
Energy Bandgap	8.9 eV

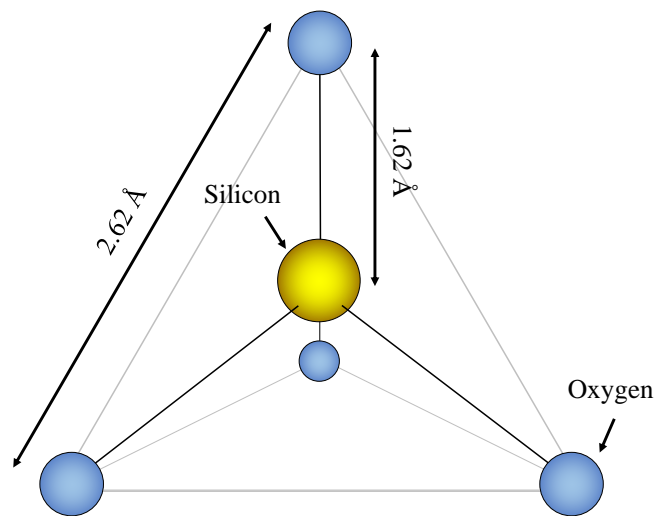
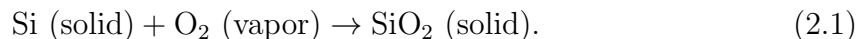


Figure 2.2: Molecular structure of  $\text{SiO}_2$ . The yellow sphere refers to Si and the blue spheres to O atoms. The Si-O and O-O bond lengths are  $1.62 \text{ \AA}$  and  $2.62 \text{ \AA}$ , respectively.

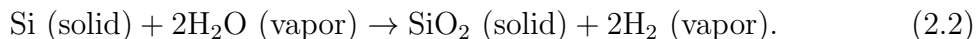
## 2.2 Fundamentals of the Oxidation Mechanism

Thermal oxidation of semiconductors (e.g., Si or SiC) is usually performed at temperatures between 800°C and 1400°C to artificially enhance the growth of the SiO<sub>2</sub> layers [1], [44]. The oxide-semiconductor interface thickness is in the majority of applications in the order of a few layers of atoms [36]. Semiconductor atoms are consumed in the oxidation process, thus the interface moves from the surface into the substrate during the oxidation process [57]. Because of the different molecule densities of semiconductor atoms compared to SiO<sub>2</sub>, the formed oxide typically expands in volume. If no mechanical boundary conditions are present, SiO<sub>2</sub> expands in all dimensions to accumulate oxygen atoms. The oxide practically grows into the wafer and on top of the wafer. For every thickness unit consumed of, e.g., Si, 2.2 thickness units of oxide will grow. Typically, after the oxidation approximately half of the oxide thickness will reside below the initial surface and half above it.

Depending on which oxidant species is used (O<sub>2</sub> or H<sub>2</sub>O), the thermal oxidation of SiO<sub>2</sub> may either be in the form of dry oxidation (wherein the oxidant is O<sub>2</sub>) or wet oxidation (wherein the oxidant is H<sub>2</sub>O). The reaction for dry (O<sub>2</sub> environment) oxidation of Si is governed by the chemical reaction

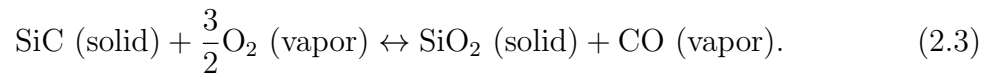


During dry oxidation, the Si wafer reacts with the ambient oxygen, forming a layer of SiO<sub>2</sub> on its surface. The dry oxidation rate is  $\approx 100$  nm/h, which results in high-quality oxide films with thicknesses of up to 100 nm. The reaction for wet (H<sub>2</sub>O environment) oxidation of Si is governed by the chemical reaction



In wet oxidation, hydrogen and oxygen gases are introduced into a torch chamber where they react to form water molecules which then enter the reactor where they diffuse toward the wafers. Oxides in a wet environment grow relatively fast compared to dry oxidation, which is the only advantage of the H<sub>2</sub>O oxidation. The reason for the fast growth is the higher oxidant solubility limit in SiO<sub>2</sub> for wet oxidation compared to dry oxidation. At 1000°C the typical solubility limit value for dry oxidation is  $5.2 \cdot 10^{16} \text{ cm}^{-3}$  and for wet oxidation  $3.0 \cdot 10^{19} \text{ cm}^{-3}$ . However, SiO<sub>2</sub> grown in a wet environment exhibits lower dielectric strength and more porosity to impurity penetration than SiO<sub>2</sub> grown in a dry environment. Therefore, wet oxidation is typically applied for thick (i.e.,  $> 100$  nm [58]) SiO<sub>2</sub>, particularly for insulation and passivation layers, where the electrical and chemical properties of the SiO<sub>2</sub> layers are not critical [1], [49]. The oxide grown in a dry environment has superior material characteristics and electrical properties, compared with oxides grown in other environments. For these reasons, the focus for the remainder of this work is on dry oxidation.

SiC is a compound semiconductor which can be thermally oxidized in a dry environment to form SiO<sub>2</sub>, similar to conventional Si [1]. The oxidation of Si is, however, considerably less complicated. The reaction for dry oxidation of SiC is governed by the chemical reaction



Thermal oxidation of SiC includes more rate-controlling steps compared to the oxidation of Si [59], [60], [61]. Those steps are: 1) Transport of molecular oxygen gas to the oxide surface, 2) in-diffusion of oxygen through the oxide film, 3) reaction with SiC at the SiO<sub>2</sub>/SiC interface, 4) out-diffusion of product gases through the oxide film, and 5) removal of product gases away from the oxide surface, shown in Figure 2.3. The last two steps are not involved in the oxidation of Si. The first and the last step are relatively fast and are not considered rate-controlling steps. In addition to the complex chemical reaction of SiC oxidation, SiC-based fabrication processes face many challenges due to SiC-based phenomena which are related to the complexity of the chemical structure and the crystal orientation. Therefore, it is extremely vital to understand and to be able to model and simulate, thus predict, SiC-related oxidation phenomena. For this reason numerous experimental and theoretical studies have been conducted in the recent decades, which laid the ground work for oxidation models, but still fell short in some aspects, e.g., crystal orientation dependence, as is discussed in the following.

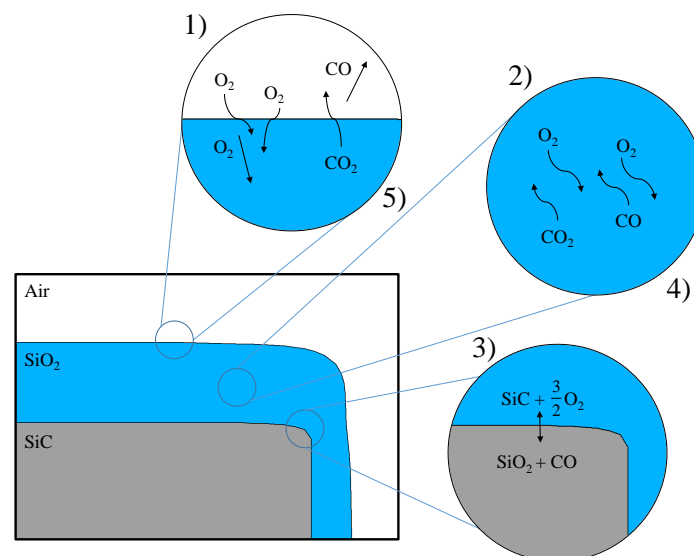


Figure 2.3: Schematic representation of the thermal oxidation process steps of SiC. 1) Solution of oxygen in the SiO<sub>2</sub>, 2) diffusion of oxygen through the SiO<sub>2</sub>, 3) reaction between SiC and O<sub>2</sub> at the SiC/SiO<sub>2</sub> interface, 4) diffusion of product gases through the SiO<sub>2</sub>, and 5) removal of product gases away from the SiO<sub>2</sub>.

## 2.3 Oxidation Models

The established macroscopic oxidation model for Si is the Deal-Grove model [62], which provides a relationship between the oxide thickness ( $X$ ) and the oxidation time ( $t$ ). The Deal-Grove model has also been applied in a modified form for the oxidation of SiC [63]. However, the oxidation growth cannot be described properly with the Deal-Grove model in the entire thickness region due to the rapid rate decrease in the initial oxidation stage for both Si [64], [65] and SiC [66], [67], [68], [69]. In order to represent the oxidation growth rates below an oxide thickness of a few tens of nanometers, Massoud's model [64], [65] has been proposed based on empirical observations. Both, in principal, successfully reproduce the growth rate data for SiC oxidation [70], [71], [72]. However, these modeling approaches lacked orientation dependence dictated by the SiC's crystal structure, which is presented in this work (cf. Section 2.5), in order to enable high accuracy 3D SiC process simulations [73]. Moreover, the exponential term of Massoud's model is not based on physical considerations, but only on fitting experimental results. To overcome this shortcoming, a Si and C emission model [69] has been proposed based on the interfacial Si and C emission phenomenon [74]. This model introduces Si and C emission into the oxide, which reduce the interfacial reaction rate [75]. However, the growth rate data is restricted to the Si-, C-, and a-face. Therefore, the orientation-dependent oxidation mechanism of SiC cannot be fully validated with experiments. For this reason, the initial oxidation process of SiC has been studied - and is presented in this work (cf. Section 2.7) - based on molecular-level simulations at various temperatures [76] and various SiC faces [77]. All of the oxidation models and molecular level investigations are described in detail in the following sections.

### 2.3.1 Deal-Grove Model

The basic Deal-Grove oxidation model has been proposed in the 1960s [62]. The model is solely based on two parameters, which are typically extracted from experiments. The model assumes a 1D structure and can be thus reasonably applied only to oxide films grown on planar substrates. The Deal-Grove model assumes that the oxidation process is dominated by the transport and interaction of the oxidant species: 1) The oxidant is transported from the gas ambient to the outer surface of the oxide, 2) the oxidant diffuses through the oxide film, and 3) the oxidant reaches the surface and reacts with Si to form SiO<sub>2</sub>, i.e., the reaction of the oxidation occurs. The three stages of the oxidation process are illustrated in Figure 2.4. Each of these steps is described as an independent flux  $F_1$ ,  $F_2$ , and  $F_3$ . The adsorption of the oxidant species through the surface of the oxide is

$$F_1 = h(C^* - C_0), \quad (2.4)$$

where  $h$  is the gas-phase transport coefficient,  $C^*$  the concentration of the oxidant in the gas ambient, and  $C_0$  the concentration of the oxidant at the SiO<sub>2</sub> surface.

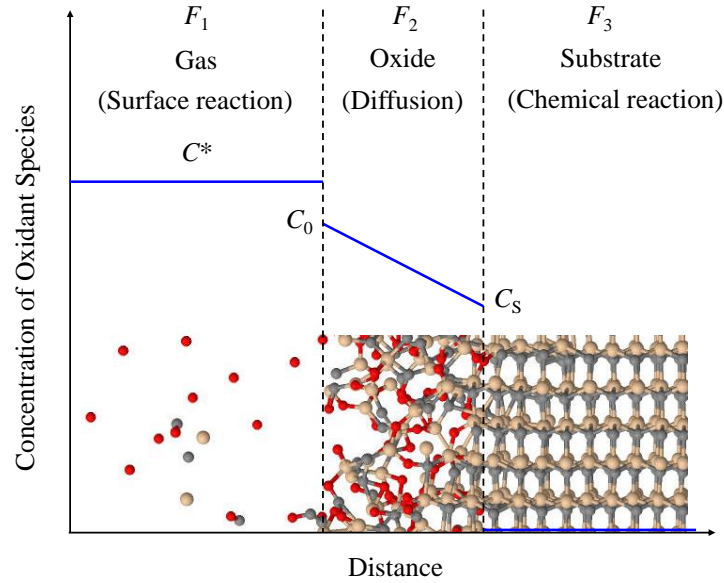


Figure 2.4: Illustration of the oxidation stages described by the Deal-Grove model.  $F_1$ ,  $F_2$ , and  $F_3$  are the three oxidation fluxes and  $C^*$ ,  $C_0$ , and  $C_S$  are the concentration of the oxidant in the gas ambient, the concentration of the oxidant at the oxide surface, and the concentration of the oxidant at the interface, respectively. The red, yellow, and gray spheres are O, Si, and C atoms, respectively. The blue lines refer to the concentration of oxidant species as a function of the distance.

Assuming saturation of the oxidation in the gas,  $C^*$  is effectively the solubility limit in the oxide and is related to the partial pressure in the atmosphere by Henry's law:

$$C^* = H \cdot p_x \quad (2.5)$$

$p_x$  is the partial pressure and  $H$  the solute-, solvent-, and temperature-dependent inverse Henry's law constant. During the oxidation process the diffusivity from the gas to the oxide surface of the oxidant species is much faster than the diffusion through the oxide and the chemical reaction at the surface. Therefore,  $F_1$  can be neglected when determining the overall oxidation kinetics.

The diffusion of the oxidant from the oxide surface to the oxide substrate interface is represented with the flux  $F_2$ . The diffusion is expressed by Fick's law:

$$F_2 = D \frac{\partial C}{\partial x} = D \frac{C_0 - C_S}{X} \quad (2.6)$$

$D$  the oxidant diffusion coefficient in the oxide,  $C_S$  the concentration of the oxidant at the interface, and  $X$  the thickness of the oxide film. Fick's law is valid under the assumption of steady state, i.e., when the variables which define the behavior of the system (concentration in this case) are not changing with time. Oxygen molecules

do not interact with  $\text{SiO}_2$  during the diffusion and maintain their molecular form. Thus, the diffusion process is straightforward, i.e.,  $\text{O}_2$  diffuses from the region of high concentration to the region of low concentration. Water vapor molecules, however, interact with  $\text{SiO}_2$  during the diffusion, thus, the diffusion process is rather complex.

The concentration of the consumed oxidant during the chemical reaction with Si atoms at the substrate surface is described with the flux  $F_3$ . The chemical oxidation reaction is given by

$$F_3 = k_s \cdot C_s, \quad (2.7)$$

where  $k_s$  is the surface rate coefficient. For the sake of simplicity, various reactions at the interface, such as Si-C bond breaking, Si-O bond formation, and  $\text{O}_2$  or  $\text{H}_2\text{O}$  bond dissociation, are here represented by a single reaction coefficient  $k_s$ . Since steady state conditions are assumed, the three fluxes representing the different stages of the oxidation process must be equal. The rate of the overall oxidation process is determined, i.e., limited, by the rate of the slowest process, such that

$$F_1 = F_2 = F_3 = \frac{C^{*}}{\frac{1}{k_s} + \frac{1}{h} + \frac{X}{D}}. \quad (2.8)$$

Since  $h$  is very large it can be neglected so that the oxidation reduces to a diffusion of oxidant followed by a chemical reaction. For a thin oxide ( $k_s X/D \ll 1$ ) the chemical reaction rate is the rate limiting step. On the other hand, for a thick oxide ( $k_s X/D \gg 1$ ) the rate limiting step is the diffusion.

The oxidation rate is proportional to the flux of the oxidant molecules and is represented by the first order differential equation

$$\frac{dX}{dt} = \frac{F}{N} = \frac{\frac{C^*}{N}}{\frac{1}{k_s} + \frac{1}{h} + \frac{X}{D}}, \quad (2.9)$$

where  $N$  (for dry  $\approx 2 \cdot 10^{22} \text{ cm}^{-3}$  and for wet oxidation  $\approx 4 \cdot 10^{22} \text{ cm}^{-3}$ ) is the number of oxidant species per unit volume of the grown oxide. The differential equation (2.9) is simplified to

$$\frac{dX}{dt} = \frac{B}{A + 2X}, \quad (2.10)$$

where

$$A = 2D \left( \frac{1}{k_s} + \frac{1}{h} \right) \quad (2.11)$$

and

$$B = 2D \frac{C^*}{N} \quad (2.12)$$

are the model parameters.  $B$  is known as the parabolic rate coefficient and

$$\frac{B}{A} = \frac{C^*}{N \left( \frac{1}{k_s} + \frac{1}{h} \right)} \quad (2.13)$$

is known as the linear rate coefficient of the Deal-Grove model. The linear rate coefficient (2.13) can be simplified under the assumption  $h \gg k_s$  to

$$\frac{B}{A} \simeq \frac{C^* k_s}{N}. \quad (2.14)$$

The parameters  $B$  and  $B/A$  are determined experimentally, because not all of the quantities in (2.11) and (2.13) are known. In particular  $k_s$  is determined by a lot of hidden physical processes associated with the numerous interface reactions. For thin oxides ( $X < 50$  nm) the dominant Deal-Grove parameter is the parabolic rate coefficient ( $B$ ) and for thick oxides ( $X > 50$  nm) the dominant parameter is the linear rate coefficient ( $B/A$ ).

In order to obtain an analytical solution of the oxide thickness, the first order differential equation (2.9) is rewritten in the form

$$(A + 2X) dX = B dt \quad (2.15)$$

and integrated over time from 0 to  $t$  and over the oxide thickness from  $X_{\text{init}}$  to  $X$ , such that

$$\int_{X_{\text{init}}}^X (A + 2X) dX = B \int_0^t dt. \quad (2.16)$$

The solution of the integral yields a quadratic equation:

$$X^2 + AX = B(t + \tau) \quad (2.17)$$

$\tau$  is the initial oxide thickness-dependent characteristic time of the initial oxidation given by

$$\tau = \frac{X_{\text{init}}^2 + AX_{\text{init}}}{B}. \quad (2.18)$$

The oxidation time for a desired oxide thickness can be estimated by

$$t = \frac{X^2 - X_{\text{init}}^2}{B} + \frac{X - X_{\text{init}}}{B/A}. \quad (2.19)$$

The oxide thickness for a desired oxidation time can be estimated by the solution of the quadratic equation

$$X = \frac{A}{2} \left( \sqrt{1 + \frac{4B}{A^2} (t + \tau)} - 1 \right). \quad (2.20)$$

For very long oxidation times, where  $t \gg \tau$  and  $t \gg A^2/4B$ , the oxide thickness is estimated as

$$X \simeq \sqrt{B \cdot t}. \quad (2.21)$$

For very short times, with  $t \ll A^2/4B$ , the oxide thickness is estimated as

$$X \simeq \frac{B}{A} (t + \tau). \quad (2.22)$$

It is clear by now that the Deal-Grove model yields a simple relationship between the oxide thickness and the oxidation time, which can be determined in a straightforward fashion. In addition, the computational effort for the oxide thickness calculation is, compared to the otherwise necessary solution of the diffusion equation, negligible. Therefore, calculating the oxide thickness is very desirable as it does not significantly increase simulation runtimes. However, as device sizes and geometries began to shrink, the limitations of the Deal-Grove model became evident. It has been observed experimentally that the oxidation growth for the initial stage of oxidation and thin oxide layers is much faster than predicted by the Deal-Grove model [1].

### 2.3.2 Massoud's Model

For both Si and SiC the oxidation mechanism for an oxide thickness  $< 50$  nm is extremely fast and non-linear [64], [65], [66], [67], [68], [69]. The causes for the increased oxidation rate are parallel oxidation mechanisms such as Si interstitials injected into the oxide, oxygen vacancies, diffusion of atomic oxygen, surface oxygen exchange, and the effects of a finite non-stoichiometric transition region between amorphous SiO<sub>2</sub> and Si. In order to include these oxidation phenomena in the initial stage of the oxidation, the Deal-Grove model has been extended with Massoud's model [64], [65], which is more accurate, but also a lot more complex.

Massoud's model is practically the Deal-Grove model with the addition of two exponential terms, which refer to the initial and intermediate oxidation regime [64]. The SiO<sub>2</sub> growth rate is thus

$$\frac{dX}{dt} = \frac{B}{A + 2X} + C_1 e^{-\frac{X}{L_1}} + C_2 e^{-\frac{X}{L_2}}. \quad (2.23)$$

$B$  and  $B/A$  are the parabolic and the linear rate coefficients, respectively, as defined by the Deal-Grove model, but their values are completely different for Massoud's model [64]. The two exponential terms represent the rate enhancement in the thin regime. It has been found that the first decaying exponential term  $C_1 \exp(-X/L_1)$  affects the fit only slightly for oxide thicknesses up to  $\approx 10$  nm [64]. Neglecting this term results in errors of less than 5%, therefore, the empirical expression often includes only the exponential term  $C_2 \exp(-X/L_2)$  in addition to the linear-parabolic term. Massoud's model is thus commonly expressed as

$$\frac{dX}{dt} = \frac{B}{A + 2X} + C e^{-\frac{X}{L}}, \quad (2.24)$$

where  $C$  is the initial enhancement parameter and  $L$  the characteristic length.

Massoud's model can be expressed as [78]

$$\frac{dX}{dt} = \frac{B + K_1 e^{-\frac{t}{\tau_1}} + K_2 e^{-\frac{t}{\tau_2}}}{A + 2X}, \quad (2.25)$$

in order to obtain an analytical solution.  $K_1$  and  $K_2$  are the pre-exponential constants and  $\tau_1$  and  $\tau_2$  the time constants. Inverting (2.25) gives a convenient expression

$$(A + 2X) dX = \left( B + K_1 e^{-\frac{t}{\tau_1}} + K_2 e^{-\frac{t}{\tau_2}} \right) dt, \quad (2.26)$$

which is then integrated over time from 0 to  $t$  and over the oxide thickness from  $x_{init}$  to  $X$ , such that

$$\int_{X_{init}}^X (A + 2X) dX = \int_0^t \left( B + K_1 e^{-\frac{t}{\tau_1}} + K_2 e^{-\frac{t}{\tau_2}} \right) dt. \quad (2.27)$$

The solution of the integral yields

$$X^2 + A \cdot X = B \cdot t + M_1 \left( 1 - e^{-\frac{t}{\tau_1}} \right) M_2 \left( 1 - e^{-\frac{t}{\tau_2}} \right) + M_0, \quad (2.28)$$

where

$$M_0 = X_{init}^2 + A \cdot X_{init}, \quad (2.29)$$

$$M_1 = K_1 \cdot \tau_1, \quad (2.30)$$

and

$$M_2 = K_2 \cdot \tau_2. \quad (2.31)$$

Solving (2.28) yields an analytic expression for the oxide thickness as a function of time:

$$X = -\frac{A}{2} + \sqrt{\left(\frac{A}{2}\right)^2 + B \cdot t + M_1 \left( 1 - e^{-\frac{t}{\tau_1}} \right) M_2 \left( 1 - e^{-\frac{t}{\tau_2}} \right) + M_0} \quad (2.32)$$

This expression can quite accurately describe the oxidation mechanism of Si and SiC, particularly for very thin oxide layers. However, the exponential term in Massoud's model is considered *non-physical*<sup>1</sup>, therefore, in order to represent all parameters as physical quantities, another modeling approach is necessary, which is discussed in the following section.

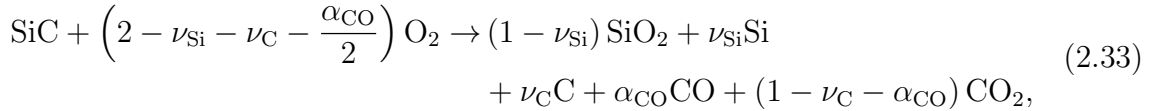
<sup>1</sup>A model is considered *non-physical* when its parameters are empirical, i.e., do not refer to any of the physical quantities, such as, e.g., diffusion coefficients, reaction rates, or solubility limits.

### 2.3.3 C and Si Emission Model

Among the various Si oxidation models which describe the enhancement in the initial stage of oxidation [74], [79], [80], the interfacial Si emission model shows the best ability to accurately fit the experimental oxidation growth rate data. According to this model, Si atoms are emitted as interstitials into the oxide layer accompanied by oxidation of Si, which is caused by the strain due to the expansion of the Si lattice during the oxidation. The oxidation rate at the interface is initially large and is suppressed by the accumulation of emitted Si atoms near the interface with increasing oxide thickness, i.e., the oxidation rate is not constant, but is a function of the oxide thickness. In the Deal-Grove model and in Massoud's model, it is considered that the oxide growth occurs only or mainly at the Si-oxide interface. However, according to the interfacial Si emission model [74], oxidation can occur inside the SiO<sub>2</sub> layer as well. In addition, for very thin oxide layers some of the emitted Si atoms can diffuse through the oxide layer and reach the oxide surface where diffused Si atoms are then instantly oxidized.

Since the density of Si atoms in 4H-SiC ( $4.8 \cdot 10^{22} \text{ cm}^{-3}$  [81]) is almost equal to the density of Si atoms in Si ( $5.0 \cdot 10^{22} \text{ cm}^{-3}$  [1]) and the residual carbon is unlikely to exist at the oxide-SiC interface in the early stage of SiC oxidation [82], the stress near or at the interface is considered to be almost identical to the oxidation of Si. Therefore, the atomic emission due to the interfacial stress also accounts for the growth enhancement for the oxidation of SiC. In addition, for the oxidation of SiC, the C emission must be taken into account as well.

The Si and C emission model has been recently proposed for the oxidation of SiC [69], which takes into account both Si and SiC emission into the oxide layer. The emission of Si and C leads to a reduction of the interfacial reaction rate. The reaction equation for SiC oxidation can be written as [82]



where  $\alpha_{\text{CO}}$  is the production ratio of CO and  $\nu_{\text{Si}}$  and  $\nu_{\text{C}}$  the emission ratio of Si and C, respectively. The interfacial reaction rate  $k$  is based on the assumption that the concentration of interstitials does not exceed the solubility limit [69]:

$$k = k_0 \left(1 - \frac{C_{\text{Si}}^{\text{I}}}{C_{\text{Si}}^0}\right) \left(1 - \frac{C_{\text{C}}^{\text{I}}}{C_{\text{C}}^0}\right) \quad (2.34)$$

$k_0$  is the initial interfacial oxidation rate,  $C_{\text{Si}}^{\text{I}}$  is the concentration of Si interstitials,  $C_{\text{C}}^{\text{I}}$  is the concentration of C interstitials,  $C_{\text{Si}}^0$  is the solubility limit of Si, and  $C_{\text{C}}^0$  is the solubility limit of C. This equation implies that the growth rate in the initial stage of oxidation is reduced, because the accumulation rates for Si and C interstitials should

be different from each other. Hence, the oxidation time, when the concentration of interstitials saturates, is different between Si and C interstitials.

The diffusion equations are given as [82]

$$\begin{aligned}\frac{\partial C_{\text{Si}}}{\partial t} &= \frac{\partial}{\partial x} \left( D_{\text{Si}} \frac{\partial C_{\text{Si}}}{\partial x} \right) - R_1 - R_2, \text{ where} \\ R_1 &= \eta C_{\text{Si}}^{\text{S}} C_{\text{O}}^{\text{S}} \text{ and} \\ R_2 &= \kappa_1 C_{\text{Si}} C_{\text{O}} + \kappa_2 C_{\text{Si}} C_{\text{O}}^2,\end{aligned}\tag{2.35}$$

$$\begin{aligned}\frac{\partial C_{\text{C}}}{\partial t} &= \frac{\partial}{\partial x} \left( D_{\text{C}} \frac{\partial C_{\text{C}}}{\partial x} \right) - R'_1 - R'_2, \text{ where} \\ R'_1 &= \eta' C_{\text{C}}^{\text{S}} C_{\text{O}}^{\text{S}} \text{ and} \\ R'_2 &= \kappa'_1 C_{\text{C}} C_{\text{O}} + \kappa'_2 C_{\text{C}} C_{\text{O}}^2,\end{aligned}\tag{2.36}$$

and

$$\begin{aligned}\frac{\partial C_{\text{O}}}{\partial t} &= \frac{\partial}{\partial x} \left( D_{\text{O}} \frac{\partial C_{\text{O}}}{\partial x} \right) - R_1 - R'_1 - R_2 - R'_2 - R_3, \text{ where} \\ R_3 &= h (C_{\text{O}}^{\text{S}} - C_{\text{O}}^{\text{O}}).\end{aligned}\tag{2.37}$$

$C_{\text{Si}}$ ,  $C_{\text{C}}$ , and  $C_{\text{O}}$  are the concentrations of Si, C, and O, respectively.  $C_{\text{Si}}^{\text{S}}$ ,  $C_{\text{C}}^{\text{S}}$ , and  $C_{\text{O}}^{\text{S}}$  are the concentrations of Si, C, and O at the oxide surface, respectively.  $D_{\text{Si}}$ ,  $D_{\text{C}}$ , and  $D_{\text{O}}$  are the diffusion coefficients of Si, C, and O, respectively.  $\eta$  is the oxidation rate of Si interstitials on the oxide surface and  $\eta'$  the oxidation rate of C interstitials on the oxide surface.  $\kappa_1$  and  $\kappa_2$  are the oxidation rates of Si interstitials on the oxide surface and  $\kappa'_1$  and  $\kappa'_2$  the oxidation rates of C interstitials on the oxide surface.  $R_2$  and  $R'_2$  represent the absorption of interstitials inside the oxide and are each assumed to consist of two terms [83].

The boundary conditions are determined from the chemical reaction of SiC oxidation (2.33), such that [69]

$$D_{\text{Si}} \frac{\partial C_{\text{Si}}}{\partial x} \Big|_{x=0} = -\nu_{\text{Si}} k C_{\text{O}}^{\text{I}},\tag{2.38}$$

$$D_{\text{C}} \frac{\partial C_{\text{C}}}{\partial x} \Big|_{x=0} = -\nu_{\text{C}} k C_{\text{O}}^{\text{I}},\tag{2.39}$$

and

$$D_{\text{O}} \frac{\partial C_{\text{O}}}{\partial x} \Big|_{x=0} = \left( 2 - \nu_{\text{Si}} - \nu_{\text{C}} - \frac{\alpha_{\text{CO}}}{2} \right) k C_{\text{O}}^{\text{I}}.\tag{2.40}$$

It should be noted that the oxidation rate in the thick oxide region is limited solely by the in-diffusion of the oxidant [70], and that the out-diffusion of CO in SiO<sub>2</sub> is much faster than that of O<sub>2</sub> [69]. Thus, it is assumed that the diffusion of CO is independent of the oxidation growth rate.

### 2.3.4 Summary of Oxidation Models

Each of the described oxidation models has its own advantages and disadvantages, including computational effort and accuracy of predicting the oxide thickness. Taking all the variabilities in account, the most appropriate approach for process TCAD simulations is currently Massoud's model due to the balance between computational costs and accuracy. The computational effort of Massoud's model is lower compared to the C and Si emission model, especially when the model is recalculated for many ( $> 10^3$ ) crystal directions in 3D simulations. On the other hand, the accuracy of Massoud's model is higher compared to the Deal-Grove model, in particular for the initial oxide thicknesses. Therefore, Massoud's model is used as the starting point for the modeling approach throughout the remainder of this work.

## 2.4 Growth Rates

Particularly important for the thermal oxidation of SiC is the dependence of the oxidation growth rates on the crystal orientation [67], [84], [85], which has significant consequences for non-planar device structures. For instance, the orientation dependence has a very high impact on the trench design of U-MOSFETs [86], where the oxide is located on all crystallographic faces [19]. In this case the oxide growth thicknesses will vary depending on the particular face, requiring advanced high-accuracy multi-dimensional modeling to correctly predict the oxide formation of the overall device. It is thus essential to carefully distinguish between the different crystal orientations of SiC. The highest difference in the growth rates of oxidation is between the top, i.e., (0001) Si-face, and the bottom, i.e., (000 $\bar{1}$ ) C-face [67], [84], [85]. The oxidation of SiC varies also with other common crystallographic faces, e.g., (1 $\bar{1}$ 00) m- and (11 $\bar{2}$ 0) a-face [87], [88].

Recently, several experimental investigations of SiC oxidation of different crystallographic faces have been performed [58], [63], [70], [89], [90], but some of the published time-dependent oxide thicknesses are inconsistent. Certain measurements from different publications vary up to a factor of three for the same material and oxidation environment. Available experimental and theoretical data has been thus collected and evaluated [72] to provide a full picture of the oxidation parameters and enable further progress in modeling and simulation of SiC-based devices.

The collected data is shown in Figures 2.5, 2.6, 2.7, and 2.8. The solid lines are fits using Massoud's model and the data points are measured values obtained from Gupta *et al.* [89], Goto *et al.* [70], Song *et al.* [63], Hosoi *et al.* [58], Kakubari *et al.* [90], and Shenoy *et al.* [91]. For all the investigated oxidation temperatures, the oxide thickness is largest for the C-face followed by the m-, a-, and Si-face.

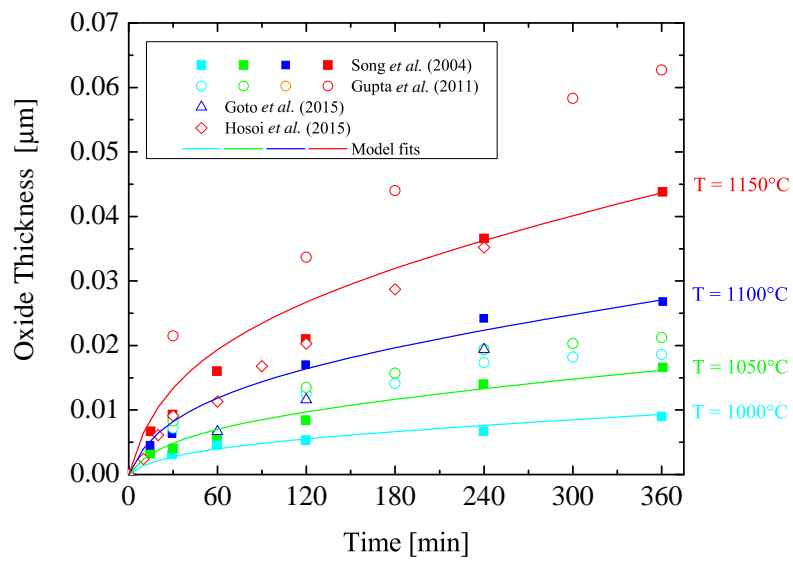


Figure 2.5: Oxide thicknesses as a function of time for various temperatures of dry thermal oxidation of the 4H-SiC (0001) Si-face. The solid lines are fits by (2.24), the symbols are measurements, and the colors indicate various temperatures.

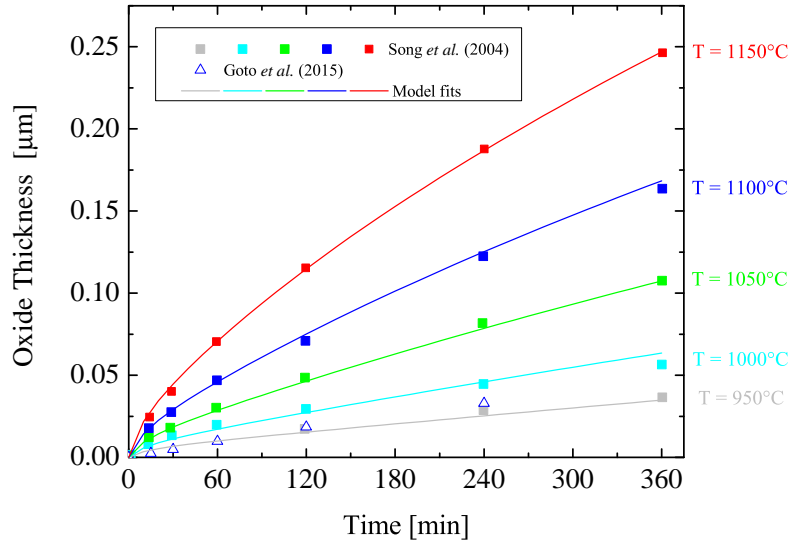


Figure 2.6: Oxide thicknesses as a function of time for various temperatures of dry thermal oxidation of the 4H-SiC (1120) a-face. The solid lines are fits by (2.24), the symbols are measurements, and the colors indicate various temperatures.

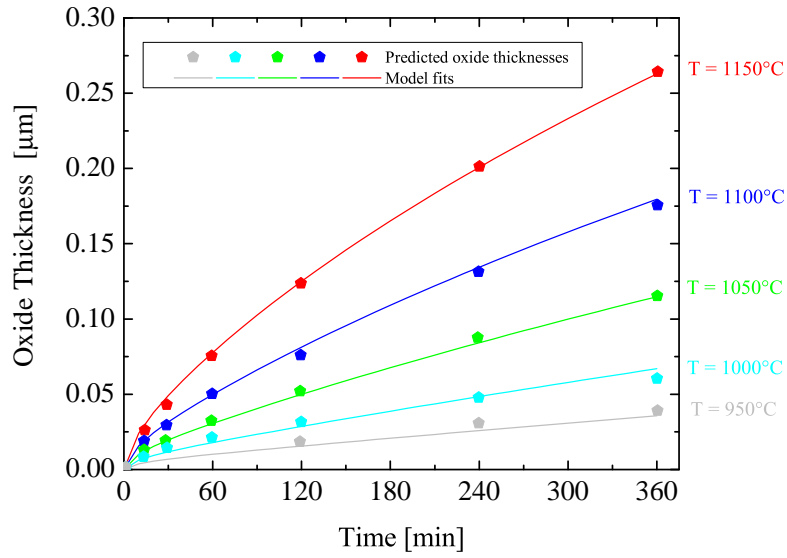


Figure 2.7: Oxide thicknesses as a function of time for various temperatures of dry thermal oxidation of the 4H-SiC ( $1\bar{1}00$ ) m-face. The solid lines are fits by (2.24), the symbols are predicted oxide thicknesses, and the colors indicate various temperatures.

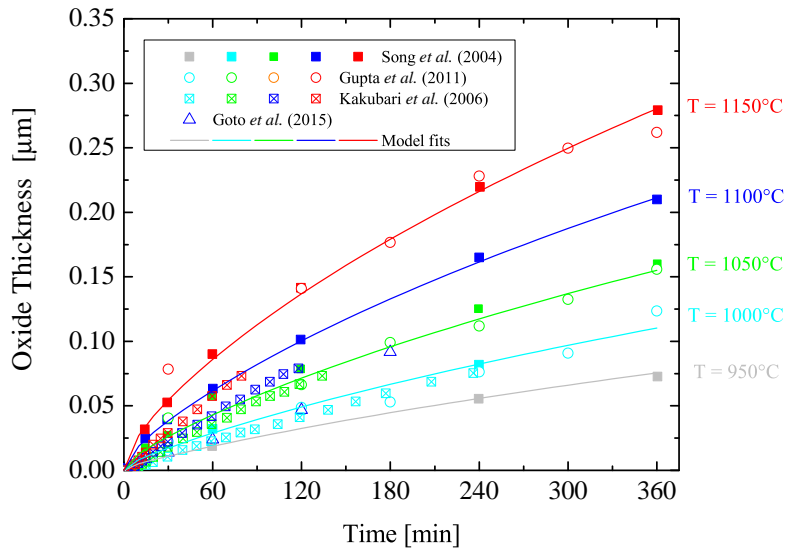


Figure 2.8: Oxide thicknesses as a function of time for various temperatures of dry thermal oxidation of the 4H-SiC ( $000\bar{1}$ ) C-face. The solid lines are fits by (2.24), the symbols are measurements, and the colors indicate various temperatures.

The growth of the oxide on SiC depends on various factors, e.g., cut-off angle, doping density, and crystal quality, which are the reasons for the various differences of experimental results. The most severe inconsistencies are observed in the measurements of Si-oriented SiC oxidation, as can be clearly seen in Figure 2.5. Therefore, only the data sets which yield conclusive results for the same oxidation environments and crystal orientations are fitted. The fitted curves are deviating less than 5% from the chosen measurements in the entire thickness region ( $2X \ll A$  and  $2X \gg A$ ), considering different surface orientations and a typical temperature range from 950 to 1150°C.

As there are no measurement sets available for the  $(1\bar{1}00)$  m-face orientation, the oxidation kinetics for the m-face is predicted (Figure 2.7) according to the oxide thicknesses of the a-face [88]. The prediction is based on the oxide thickness ratio between the m- and a-face  $X^{(1\bar{1}00)}(t = 720 \text{ min})/X^{(11\bar{2}0)}(t = 720 \text{ min}) = 1.073$ . Accordingly, the m-face kinetics is calculated from the oxidation kinetics of the a-face [92].

The processes of SiC oxidation can be presented by time-dependent oxide thicknesses ( $X(t)$ ) or growth rates ( $dX/dt(t)$ ), and/or thickness-dependent growth rates ( $dX/dt(X)$ ) [64], [65]. All of the fits use an industry-proven procedure, i.e., the time-dependent oxide thickness data is fitted with the differential expression of Massoud's model (2.24). The very well known fourth-order Runge-Kutta method [93], [94] is used to find a numerical approximation for the solution of the ordinary differential equation. The numerical integration of Massoud's model includes the following growth rate coefficients:  $B/A$ ,  $B$ ,  $C$ , and  $L$ , whose values must be correctly set for accurate fitting. Thus, a fitting algorithm with an auto-step size adjustment is typically used to ensure the best fit [95]. The ratio of the SiC oxidation process highly depends on the temperature, i.e., all of the growth rate coefficients  $B/A$ ,  $B$ ,  $C$ , and  $L$  are temperature-dependent. The relation between the absolute temperature  $T$  and the rate constant  $k$  is typically given by an Arrhenius equation [96].

### 2.4.1 Arrhenius Equation

Rates of chemical reactions depend on various physical quantities, e.g., temperature and pressure. The collision theory and transition state theory implies that chemical reactions typically proceed faster at higher temperature or pressure and slower at lower temperature or pressure. The molecules move faster as the temperature increases and therefore collide more frequently, which changes the properties of the involved chemical reactions.

In order to mathematically describe and analyze the temperature dependence of chemical reaction rate coefficients, they are typically expressed with an Arrhenius equation and displayed as an Arrhenius plot, i.e., logarithm of coefficient as a function of the inverse temperature [96]. The Arrhenius equation has an important application in

determining activation energies of chemical reactions and is used to model the temperature variation of diffusion coefficients, population of crystal vacancies, creep rates, and many other thermally-induced processes or reactions. The Arrhenius equation is given in the form

$$k = Z e^{-\frac{E_a}{k_B T}}, \quad (2.41)$$

where  $Z$  is the pre-exponential factor,  $E_a$  the activation energy of the reaction,  $k_B$  the Boltzmann constant, and  $T$  the absolute temperature. Alternatively, the Arrhenius equation may be expressed as

$$k = Z e^{-\frac{E_a}{RT}}, \quad (2.42)$$

where  $R$  is the ideal gas constant.

Taking the natural logarithm of the Arrhenius equation (2.41) yields

$$\ln k = -\frac{E_a}{k_B T} + \ln Z. \quad (2.43)$$

The logarithmic representation has the same form as the linear function

$$Y = KX + M, \quad (2.44)$$

where

$$Y = \ln k, \quad (2.45)$$

$$K = -\frac{E_a}{k_B}, \quad (2.46)$$

$$X = \frac{1}{T}, \quad (2.47)$$

and

$$M = \ln Z. \quad (2.48)$$

The linear expression of the Arrhenius equation is commonly used to determine  $E_a$  and  $Z$  of a specific chemical reaction by a linear fitting method [94].

The most common fitting approach for the linear function is the linear regression model [97] with a single explanatory variable [98], [99]. The linear regression model takes into account one independent and one dependent variable of the 2D sample of points and finds the best fit of the linear function according to the ordinary least squares method [100]. The linear regression tends to minimize the sum of the errors between the values of the fitting function and the data sets. The least-squares method thus finds its optimum, when the error *Err*, i.e., sum of the squared residuals,

$$Err = \sum_{i=1}^n R_i^2 \quad (2.49)$$

is minimal. The residual is defined as the difference between the actual value of the dependent variable  $Y_i$  and the value predicted by the fitting function according to the independent variable  $X_i$ . The residual is thus

$$R_i = Y_i - f(X_i). \quad (2.50)$$

With a simple linear regression analysis and the linear expression of the Arrhenius equation (2.43) any temperature-dependent parameter can be fitted. With this approach one is able to obtain  $E_a$  and  $Z$  for each of the oxidation growth rate coefficients.

## 2.4.2 Calibrated Parameters

The growth rate coefficient  $B$  of Massoud's model describes the diffusivity in  $\text{SiO}_2$ . Therefore,  $B$  is determined by the nature of the oxide. Thus,  $B$  is not crystal orientation-dependent, but is identical for all SiC orientations. Since converting a SiC molecule into  $\text{SiO}_2$  and CO (as in the case for SiC oxidation) consumes 1.5 times the amount of oxygen than converting Si into  $\text{SiO}_2$  only (as in the case for Si oxidation),  $B$  is assumed to be 1/1.5 of that of Si [70]

$$B = \frac{2D_{\text{O}}^{\text{SD}}}{1.5}, \quad (2.51)$$

where  $D_{\text{O}}^{\text{SD}}$  is the oxygen self-diffusivity in  $\text{SiO}_2$  for the Si oxidation. The diffusivity is in general temperature-dependent and can be predicted by an Arrhenius equation [101]

$$D_{\text{O}}^{\text{SD}} = D_0 e^{\left(-\frac{E_a^{\text{SD}}}{k_{\text{B}}T}\right)}, \quad (2.52)$$

where  $D_0$  is the diffusion coefficient and  $E_a^{\text{SD}}$  is the activation energy. In the case of Si oxidation,  $D_0 = 192 \mu\text{m}^2 \text{min}^{-1}$  and  $E_a^{\text{SD}} = 1.64 \text{ eV}$ , as reported in Kageshima *et al.* [101]. Accordingly, the value of  $B$  is assumed to be

$$B = 256 \cdot e^{\left(-\frac{1.64 \text{ eV}}{k_{\text{B}}T}\right)} \mu\text{m}^2 \text{min}^{-1}. \quad (2.53)$$

The rest of the growth rate coefficients ( $B/A$ ,  $C$ , and  $L$ ) are highly orientation-dependent. These are determined with the fitting procedure as shown in Figures 2.5, 2.6, 2.7, and 2.8. The temperature dependence of the parabolic growth rate coefficient  $B$ , the linear growth rate coefficient  $B/A$ , the initial enhancement parameter  $C$ , and the characteristic length  $L$  are shown in Figures 2.9, 2.10, 2.11, and 2.12, respectively.

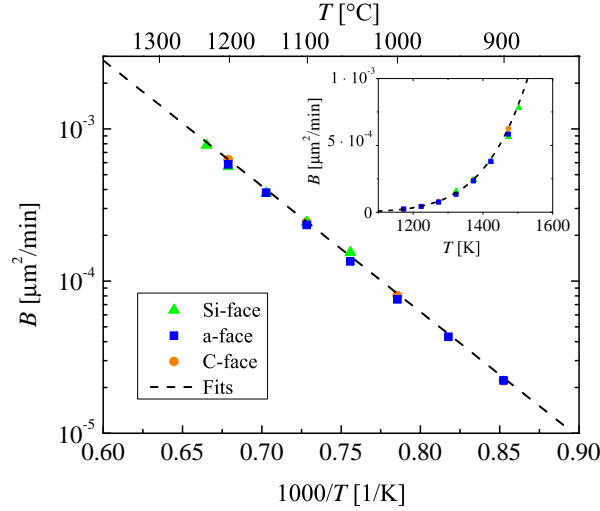


Figure 2.9: Temperature-dependent parabolic growth rate coefficient  $B$  for the (0001) Si- (green triangles), the  $(11\bar{2}0)$  a- (blue squares), the  $(1\bar{1}00)$  m- (red diamonds), and the  $(000\bar{1})$  C-face (orange circles) of 4H-SiC dry thermal oxidation. The data sets for the Si-, a-, and C-face (symbols) are obtained from experimental findings [70]. The dashed lines represent fits by (2.53). The inset figure shows linear  $y$  axis and non-reciprocal  $x$  axis.

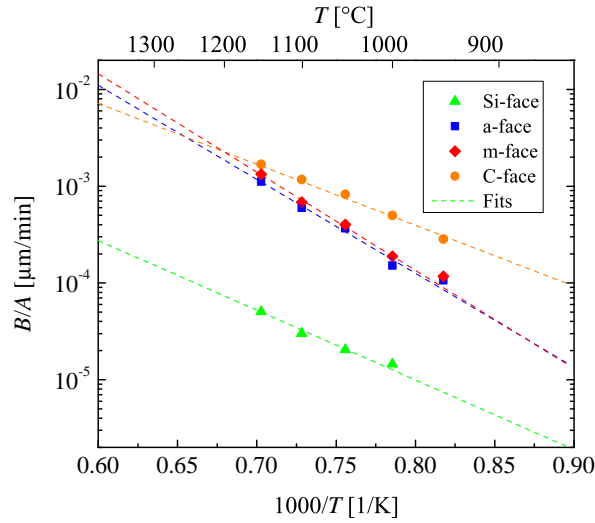


Figure 2.10: Temperature-dependent linear growth rate coefficient  $B/A$  for the (0001) Si- (green triangles), the  $(11\bar{2}0)$  a- (blue squares), the  $(1\bar{1}00)$  m- (red diamonds), and the  $(000\bar{1})$  C-face (orange circles) of 4H-SiC dry thermal oxidation. The rate coefficients at various temperatures (symbols) are obtained by fitting Massoud's model to the data shown in Figures 2.5, 2.6, 2.7, and 2.8. The dashed lines represent fits by the Arrhenius equation (2.43).

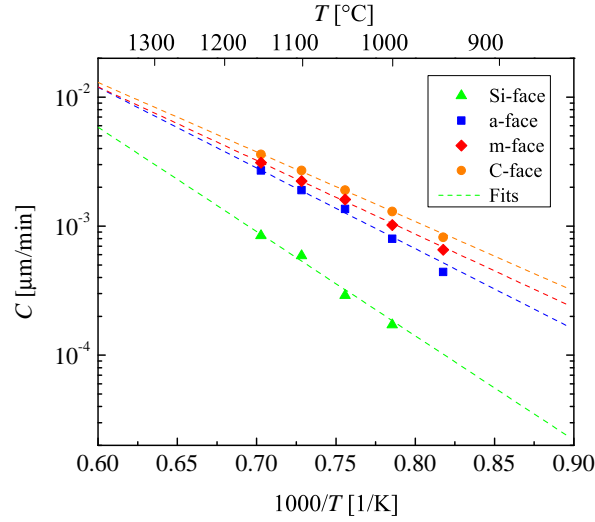


Figure 2.11: Temperature-dependent initial enhancement parameter  $C$  for the (0001) Si- (green triangles), the  $(11\bar{2}0)$  a- (blue squares), the  $(1\bar{1}00)$  m- (red diamonds), and the  $(000\bar{1})$  C-face (orange circles) of 4H-SiC dry thermal oxidation. The rate coefficients at various temperatures (symbols) are obtained by fitting Massoud's model to the data shown in Figures 2.5, 2.6, 2.7, and 2.8. The dashed lines represent fits by the Arrhenius equation (2.43).

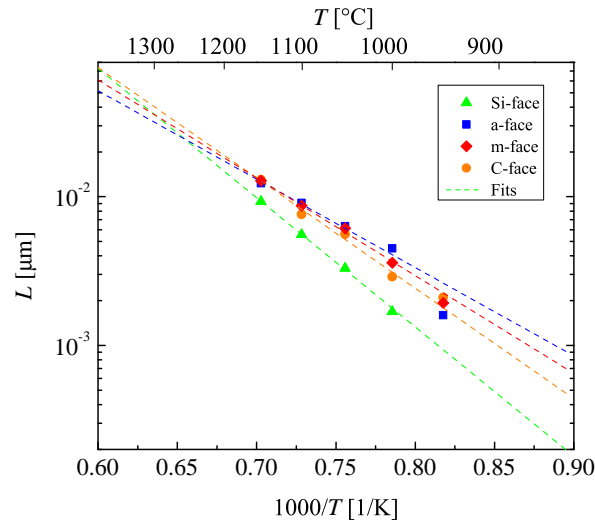


Figure 2.12: Temperature-dependent characteristic length  $L$  for the (0001) Si- (green triangles), the  $(11\bar{2}0)$  a- (blue squares), the  $(1\bar{1}00)$  m- (red diamonds), and the  $(000\bar{1})$  C-face (orange circles) of 4H-SiC dry thermal oxidation. The rate coefficients at various temperatures (symbols) are obtained by fitting Massoud's model to the data shown in Figures 2.5, 2.6, 2.7, and 2.8. The dashed lines represent fits by the Arrhenius equation (2.43).

The slopes of the Arrhenius plots of the Si- and the C-face (Figure 2.10) are almost identical, i.e., the values of the activation energies  $E_a$  are comparable for both orientations. The activation energy of the linear growth rate coefficient defines the interfacial reaction rate and is strongly correlated with the crystal structure of the oxidizing surface [89], [102]. Additionally, it is evident that the slopes of the Arrhenius plot of the a- and m-face are almost identical as well. Therefore, the activation energies are expected to be similar for surfaces with similar structures, which is verified by Figure 2.10.

The crystal structure of 4H-SiC is almost identical for the Si-face (top) and C-face (bottom), as well as for the a- (one side) and m-face (another side of the crystal). Comparing this observation with the thermal oxidation of Si, the interface chemical reaction is almost the same for the Si- and the C-face [103]. Nevertheless, the oxidation growth rates for the Si and the C-face are different as the areal density of atoms and the mechanical stress effects at the interface play a crucial role in the oxidation, which can be explained by the magnitude of the pre-exponential factor of the linear growth rate coefficient [63]. This is in agreement with recent theoretical findings [72], where the differences in the growth rates of the Si- and the C-face are mainly significant in the pre-exponential factor  $Z$ , which is an order of magnitude larger for the C-face compared to the Si-face. Figure 2.10 also shows that the activation energies of the m- and a-face are higher than the activation energies of the C- and the Si-face. Additionally, the results in Figure 2.10 suggest that the difference of the linear growth rate coefficient between the a- and m-face is negligible for the low temperature regime, which is in agreement with experimental findings [86].

Figure 2.11 shows that the growth rate enhancement parameter for thin oxides for all four crystallographic faces is temperature-dependent. These results suggest that the initial oxidation growth rate is highest for the C-face, followed by the m, a, and Si-face orientation. By comparing the results of Figures 2.10 and 2.11 it becomes clear that the ratios of the growth rate coefficients between the four crystallographic faces are different. This suggests that the temperature dependence of the initial and the linear growth rates is diverse. The values of  $B/A$  are in the same order of magnitude than the values of  $C$ , hence, the contribution of the initial oxide growth enhancement cannot be neglected [66], [68]. This fact is in alignment with the already established knowledge that the Deal-Grove model cannot accurately predict the oxidation kinetics for SiC.

The results in Figure 2.12 suggest that also the characteristic length  $L$  is temperature- and orientation-dependent.  $L$  is determined by the oxidation and the diffusion coefficient of  $\text{SiO}_2$  interstitials and the emission ratios of Si and C interstitials. An increase in the diffusion coefficient leads to an increase of  $L$ , while an increase of the oxidation coefficient or the emission ratio of interstitials leads to a reduction of  $L$  [70]. The results in Figure 2.12 are consistent with the reports from experimental findings [70], [80], which suggest that a temperature increase is more significant for the diffusion coefficient than the oxidation coefficient or emission ratios.

Higher values of  $L$  are observed for the C-face orientation than for the Si-face for the temperature regime below 1265°C, which is consistent with the predictions that the emission ratio for the Si-face is significantly larger than that for the C-face [71], [104]. Interestingly, higher values of  $L$  for the m- and the a-face than the ones for the C-face are in addition observed for  $T < 1265^\circ\text{C}$ , i.e., the initial growth enhancement is larger for the m- and the a-face for this temperature regime. It is believed that the reason for this phenomenon is a higher diffusion coefficient, lower emission ratio, and lower oxidation coefficient of the m- and the a-face compared to the C-face [72]. Results in Figure 2.12 also suggest that the above mentioned relations are reversed for temperatures above 1265°C. In addition, the differences in  $L$  between the Si and the C-face at very high oxidation temperatures are lower than 5%. Therefore, in the high-temperature region the value of  $L$  for both these faces is approximately the same.

An overview of the activation energies and the pre-exponential factors of the Arrhenius plots for all four inspected crystallographic faces is provided in Table 2.2. As discussed before, the pre-exponential factor has a significant role in the temperature dependence of the SiC oxidation kinetics. Therefore, it is always necessary to present Arrhenius plots, enabling to consider  $E_a$  together with  $Z$ .

With these validated parameters (Table 2.2) it is now possible to accurately calculate multi-dimensional 4H-SiC oxidation kinetics. The predicted oxidation growth rates as a function of oxide thickness for the Si-, a-, m-, and C-face at various relevant temperatures ( $T = 950, 1000, 1050, 1100, \text{ and } 1150^\circ\text{C}$ ) are shown in Figure 2.13. The calculations suggest that the initial enhancement of the oxide growth is strongest for the Si-face. Furthermore, at low temperatures the differences in the growth rates between the m- and the a-face orientations are less than 5%.

Table 2.2: Activation energies and pre-exponential factors of the Arrhenius plots for the (0001) Si-, (11 $\bar{2}$ 0) a-, (1 $\bar{1}$ 00) m-, and (000 $\bar{1}$ ) C-face of 4H-SiC dry thermal oxidation. The linear rate coefficient  $B/A$ , the initial enhancement parameter  $C$ , and the characteristic length  $L$  have been obtained by fitting Eq. (2.43) to the data presented in Figure 2.10, 2.11, and 2.12.

4H-SiC face	$B/A$		$C$		$L$	
	$E_a$ [eV]	$Z$ [ $\mu\text{m}/\text{min}$ ]	$E_a$ [eV]	$Z$ [ $\mu\text{m}/\text{min}$ ]	$E_a$ [eV]	$Z$ [ $\mu\text{m}$ ]
Si	1.429	5.751	1.604	412.9	1.724	$1.190 \cdot 10^4$
a	1.927	$7.404 \cdot 10^3$	1.241	67.51	1.180	189.5
m	2.015	$1.791 \cdot 10^4$	1.132	31.84	1.305	539.8
C	1.249	42.70	1.069	22.22	1.473	$2.096 \cdot 10^3$

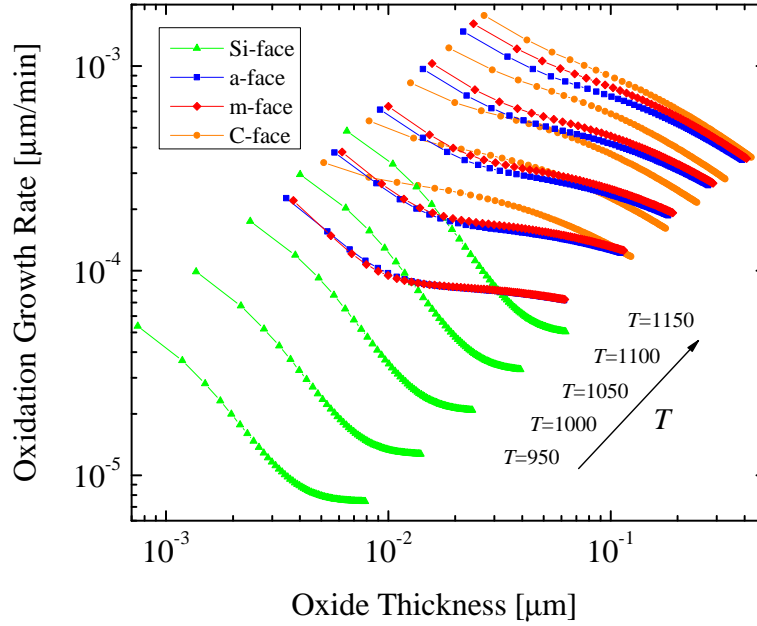


Figure 2.13: Oxide growth rates as a function of the oxide thickness at various temperatures for the (0001) Si- (green triangles),  $(11\bar{2}0)$  a- (blue squares),  $(1\bar{1}00)$  m- (red diamonds), and  $(000\bar{1})$  C-face (orange circles) of 4H-SiC dry thermal oxidation.

Additionally, the growth rate of the C-face is significantly larger compared to the other orientations at low temperatures, e.g.,  $T = 950^\circ\text{C}$ , the average growth rates for the Si-, a-, m-, and C-face are  $0.12 \cdot 10^{-4}$ ,  $0.90 \cdot 10^{-4}$ ,  $0.93 \cdot 10^{-4}$ , and  $1.82 \cdot 10^{-4} \mu\text{m}/\text{min}$ , respectively. On the other hand, this difference is less pronounced at higher temperatures, e.g.,  $T = 1150^\circ\text{C}$ , the average growth rates for the Si-, a-, m-, and C-face are  $0.93 \cdot 10^{-4}$ ,  $5.70 \cdot 10^{-4}$ ,  $6.02 \cdot 10^{-4}$ , and  $6.39 \cdot 10^{-4} \mu\text{m}/\text{min}$ , respectively.

The saturation of the oxidation process depends on the temperature and pressure as well as on the chemical nature of the substances. The derivatives of the curves shown in Figure 2.13 indicate that the saturation of the oxide growth is highest, i.e., the oxidation process is hindered the most, for Si-oriented SiC. This is consistent with experimental and theoretical reports [66], [69], [70]. The calculations corroborate that the saturation of SiC oxidation is indeed orientation-dependent. However, in order to describe the oxidation in an arbitrary crystal direction, an extension of the oxidation models is necessary.

## 2.5 Interpolation Method

The available oxidation models alone fail to predict the oxide growth for 3D structures due to their 1D nature. An approach which extends these models by incorporating the crystal direction dependence into the oxidation growth rates has thus been developed [73], [92] and is discussed in the following.

The geometrical aspects of SiC can be mathematically described according to basic crystallography [105] and experimental findings [86], [88]. A unit cell of the hexagonal crystal structure includes six  $(1\bar{1}00)$  m-faces and six  $(11\bar{2}0)$  a-faces symmetric with respect to the  $z$  axis, while there is only one  $(0001)$  Si-face on the top and one  $(000\bar{1})$  C-face on the bottom of the crystal structure.

To obtain the oxidation growth rate for an arbitrary crystal direction, a direction-dependent interpolation method [92] is utilized. This interpolation method computes a growth rate for a given crystal direction based on a set of known growth rate values. The known growth rates have been discussed in the previous section (cf. Section 2.4), i.e., the growth rates of the Si-, m-, a-, and C-face, which correspond to the  $(0001)$ ,  $(1\bar{1}00)$ ,  $(11\bar{2}0)$ , and  $(000\bar{1})$  crystal directions, respectively [63], [70], [87]. These four oxidation growth rates are input arguments for the interpolation method.

The interpolation method consists of a symmetric star shape in the  $x$ - $y$  plane and a tangent-continuous union of two half-ellipses in  $z$  direction. The method yields a symmetry in the  $x$ - $y$  plane such that the oxidation growth rates in direction of a- and m-faces repeat six times with an enclosed angle of  $\pi/6$ . A schematic representation of the interpolation in the  $x$ - $y$  and  $x$ - $z$  plane is shown in Figure 2.14. The blue lines refer to the interpolation between the known growth rates, indicated with the cross symbols. The direction and the length of the arrows represent crystal directions toward SiC faces and oxidation growth rate values, respectively. A less accurate linear interpolation could be considered as well, shown with the dotted black lines and sharp edges, which would also fit the geometry of SiC. However, the non-linear method offers considerable higher accuracy [92]. The interpolation method can be represented in a parametric or an explicit expression. Both approaches are discussed in the following sections.

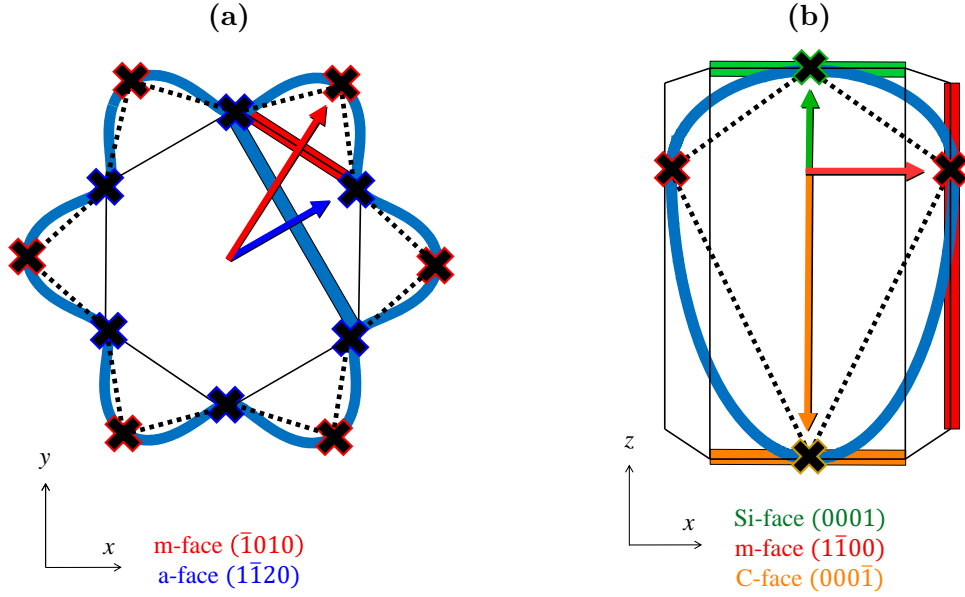


Figure 2.14: Schematic representation of the interpolation method in the (a)  $x$ - $y$  and (b)  $x$ - $z$  plane. A linear (black dotted) and a non-linear (blue line) interpolation is calculated according to four known growth rate values (black crosses) of Si- (green), m- (red), a- (blue), and C-face (orange square). Colored arrows represent crystal directions towards the corresponding faces. The arrow lengths are proportional to the oxidation growth rates.

### 2.5.1 Parametric Expression

For plotting surfaces of higher dimensions, the most convenient representation of the interpolation method in 3D space is the parametric expression, written as [73]

$$\begin{aligned}
 x &= (k_y + (k_x - k_y) \cos^2(3t)) \cos(t) \cos(u), \\
 y &= (k_y + (k_x - k_y) \cos^2(3t)) \sin(t) \cos(u), \\
 z &= k_z \sin(u),
 \end{aligned} \tag{2.54}$$

where  $x$ ,  $y$ , and  $z$  are the Cartesian coordinates,  $t \in [0, 2\pi]$  and  $u \in [-\pi/2, \pi/2]$  are the arbitrary parametric variables, and  $k_x$ ,  $k_y$ , and  $k_z$  are the oxidation growth rates in directions of  $x$ ,  $y$ , and  $z$ , respectively. In this case the following values are considered:  $k_x = k_m$ ,  $k_y = k_a$ , and  $k_z = k_C$  or  $k_{Si}$ .

As shown in several studies [69], [70], [79], the oxide growth on the top and the bottom of the SiC crystal is different, thus the positive and the negative  $z$  coordinates are calculated separately, yielding

$$\begin{aligned}
 z &= k_z^+ \sin(u) \text{ for } u \geq 0 \text{ and} \\
 z &= k_z^- \sin(u) \text{ for } u < 0.
 \end{aligned} \tag{2.55}$$

$k_z^+$  and  $k_z^-$  correspond to the growth rates in the direction of the Si- and C-face, respectively. Thus, it is defined that  $k_z^+ = k_{\text{Si}}$  and  $k_z^- = k_C$ .

The parametric expression of the interpolation method (2.54) is utilized to calculate, for example, linear oxidation growth rates ( $B/A$ ) in 3D space, shown in Figure 2.15. Calculations are performed with the known oxidation parameters at  $T = 1100^\circ\text{C}$ , i.e.,  $k_{\text{Si}} = 1.81 \text{ nm/h}$ ,  $k_a = 35.9 \text{ nm/h}$ ,  $k_m = 41.0 \text{ nm/h}$ , and  $k_C = 70.2 \text{ nm/h}$  (cf. Section 2.4.2) [72].

The growth rate surface is given by a nonlinear interpolation between these known growth rate values and follows the geometry of SiC, i.e., the crystallographic planes tangent to the growth rate surface at  $k_{\text{Si}}$ ,  $k_m$ ,  $k_a$ , and  $k_C$  are parallel to the corresponding faces. The distance from the origin  $(0,0,0)$  to any point on the growth rate surface gives the oxidation rate in direction to this point. For example, if we consider to calculate a single oxidation growth rate in direction of  $t = 1/4\pi$  and  $u = 1/4\pi$ , the result according to (2.54) is:  $k(x) = 19.23 \text{ nm/h}$ ,  $k(y) = 19.23 \text{ nm/h}$ , and  $k(z) = 1.28 \text{ nm/h}$ . The final oxidation growth rate is the distance from the origin to  $(x, y, z)$ :  $(19.23^2 + 19.23^2 + 1.28^2)^{1/2} \text{ nm/h} = 27.22 \text{ nm/h}$ .

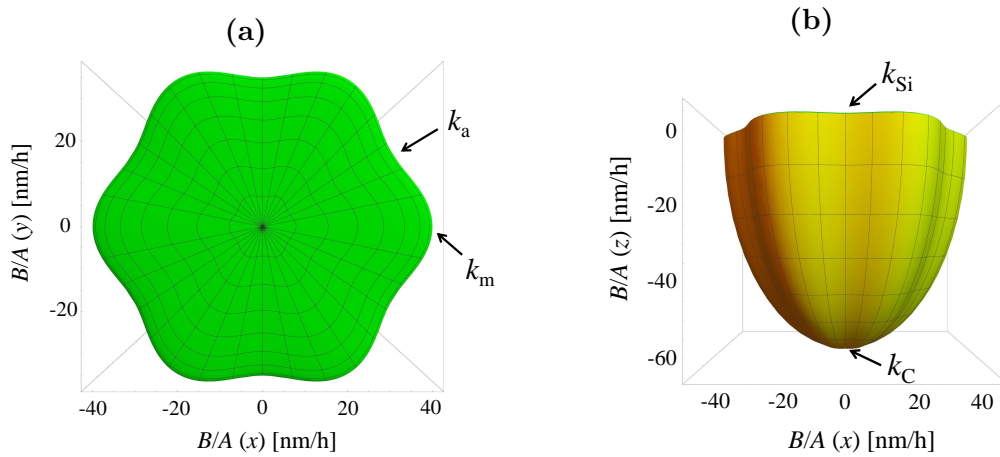


Figure 2.15: 3D calculations of the linear oxidation growth rates  $B/A$  obtained with the parametric expression of the interpolation method. The figure shows (a) the top and (b) the front view of the growth rates' surface. An arbitrary direction growth rate is calculated according to the four known growth rates ( $k_{\text{Si}}$ ,  $k_m$ ,  $k_a$ , and  $k_C$ ) shown with the black arrows. The surface colors show calculations for positive (green) and negative (orange)  $z$  direction. The calculations are performed for oxidation at  $T = 1100^\circ\text{C}$ .

### 2.5.2 Explicit Expression

The parametric expression of the interpolation method can be converted into an explicit expression, which describes the surface as the zero set of equation  $f(x, y, z) = 0$ , where  $x$ ,  $y$ , and  $z$  are the vector coordinates of the arbitrary direction of interest. The explicit expression follows the geometry of the hexagonal structure just like the parametric expression, but returns a value in the range from 0 to 1. The explicit expression is thus

$$f(x, y, z) = \left(2(x^2 + y^2)^3 - (x^2 + y^2)^4 - x^2(x^2 - 3y^2)^2\right) + z^2. \quad (2.56)$$

The direction vector  $\vec{v}(x, y, z)$  must be normalized, i.e., vector length  $|\vec{v}| = 1$ . Using expression (2.56), the growth rate coefficients are rewritten into an interpolation method such that [106]

$$\begin{aligned} k(x, y, z) = k_y + (k_x - k_y) & \left(2(x^2 + y^2)^3 \right. \\ & - (x^2 + y^2)^4 \\ & \left. - x^2(x^2 - 3y^2)^2\right) \\ & + (k_z - k_y)z^2. \end{aligned} \quad (2.57)$$

Including the four known growth rate values in the 3D interpolation method and treating the positive and the negative  $z$  coordinates separately yields

$$\begin{aligned} k(x, y, z) = k_a + (k_m - k_a) & \left(2(x^2 + y^2)^3 \right. \\ & - (x^2 + y^2)^4 \\ & \left. - x^2(x^2 - 3y^2)^2\right) \\ & + (k_{\text{Si}} - k_a)z^2 \text{ for } z \geq 0 \text{ or} \\ & + (k_{\text{C}} - k_a)z^2 \text{ for } z < 0. \end{aligned} \quad (2.58)$$

$k_{\text{Si}}$ ,  $k_{\text{m}}$ ,  $k_{\text{a}}$ , and  $k_{\text{C}}$  are the four known growth rate values, which correspond to the Si-, m-, a-, and C-face, respectively.

The explicit representation is more general and more suitable for 1D and 2D calculations, because it is more closely related to the concepts of constructive solid geometry and is typically represented with  $x$  and  $y$  coordinates. However, the parametric form is more convenient for 3D plotting and remains dominant in computer graphics and geometrical modeling due to the ability to reduce the number of independent variables, i.e., it replaces the coordinates  $x$ ,  $y$ , and  $z$  with two parametric variables  $t$  and  $u$ .

Schematic representations of the hexagonal crystal structure and the variables for the following calculations are shown in Figure 2.16. 2D calculations are typically performed either in the  $x$ - $y$ ,  $x$ - $z$ , or  $(x+y)/2$ - $z$  plane. The input of the interpolation method is an arbitrary crystal direction vector  $\vec{v}$  contained in the  $x$ - $y$  or  $x$ - $z$  plane for which the oxidation growth rate has to be computed. Denoting the angle between  $\vec{v}$  and the  $x$  axis by  $\alpha$  in  $x$ - $y$  plane or by  $\beta$  in  $x$ - $z$  plane yields the following relations

$$\begin{aligned} x &= |\vec{v}| \cos \alpha, \\ y &= |\vec{v}| \sin \alpha, \end{aligned} \quad (2.59)$$

and

$$\begin{aligned} x &= |\vec{v}| \cos \beta, \\ z &= |\vec{v}| \sin \beta. \end{aligned} \quad (2.60)$$

The explicit expression of the interpolation method (2.58) is utilized for calculations of arbitrary oxidation growth rates in 2D space. For example, the linear growth rates ( $B/A$ ) of the thermal SiC oxidation, shown in Figure 2.17, are calculated with the known growth rate parameters at  $T = 1100^\circ\text{C}$ , i.e.,  $k_{\text{Si}} = 1.81 \text{ nm/h}$ ,  $k_{\text{a}} = 35.9 \text{ nm/h}$ ,  $k_{\text{m}} = 41.0 \text{ nm/h}$ , and  $k_{\text{C}} = 70.2 \text{ nm/h}$  (cf. Section 2.4.2) [72]. Calculations are performed in the  $x$ - $y$  and  $x$ - $z$  plane using normalized crystal direction vector coordinates  $x$ ,  $y$ , and  $z$  as input for the interpolation method. The combination of vector coordinates ( $x, y$  or  $x, z$ ) define the crystal direction for which the oxide thickness is calculated. The considered vectors cover the whole  $x$ - $y$  and  $x$ - $z$  plane of the given crystal directions, which is clearly seen by the gray circle below the plots.

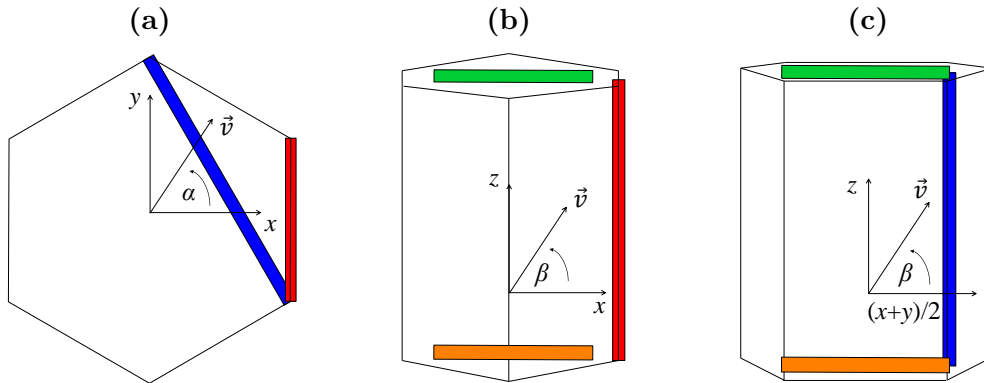


Figure 2.16: Schematic representation of the hexagonal crystal structure in the (a)  $x$ - $y$ , (b)  $x$ - $z$ , and (c)  $(x+y)/2$ - $z$  plane.  $\vec{v}$  is the crystal direction vector,  $\alpha$  is an angle in the  $x$ - $y$  plane, and  $\beta$  is an angle in the  $x$ - $z$  or  $(x+y)/2$ - $z$  plane. The blue, red, green, and orange squares represent the a-, m-, Si-, and C-face, respectively.

The thicknesses of SiC thermal oxidation in 2D space are calculated with Massoud's model (cf. Section 2.3.2) and the interpolation method for the growth rate parameters  $B/A$ ,  $C$ , and  $L$ . The oxide thicknesses as a function of the vector coordinates  $x$ ,  $y$ , and  $z$  (calculated for the  $x$ - $y$  and  $x$ - $z$  plane) are shown in Figure 2.18. In the first plot six maxima and six minima are observed, which correspond to the m- and a-face, respectively. The final oxide thickness in the direction of the m-face is approximately 288 nm and in the direction of the a-face 273 nm. On the second plot one maximal and one minimal oxide thickness is observed, which correspond to the C- and the Si-face, respectively. The final oxide thickness in the direction of the Si-face is approximately 39 nm and in the direction of the C-face 327 nm. These results are in a good agreement with experimental findings [88].

In order to allow for a straightforward comparison between theoretical calculations and experimental data, the oxide thicknesses  $X$  are normalized with the maximal oxide thickness  $X_{\max}$ , such that

$$\hat{X} = X/X_{\max}. \quad (2.61)$$

Thus,  $\hat{X} = 1$  corresponds to the maximum oxide thickness and  $\hat{X} = 0$  corresponds to no oxide on the surface of SiC. The main goal of such a comparison is to validate and corroborate the ratios between the growth rates for various crystal directions. The oxide thicknesses as a function of  $\alpha$  and  $\beta$ , i.e., the angle between the crystal direction vector and the  $x$  axis, are shown in Figure 2.19. The calculations are performed for an angle ranging from  $0^\circ$  to  $360^\circ$  for both planes. The calculated results for the normalized oxide thicknesses are in good agreement with available measurements [87].

Moreover, these results provide the basis for multi-dimensional simulations of dry oxidation of 4H-SiC. 2D and 3D simulations can thus be augmented by the interpolation method for the oxidation growth rates, where the only limiting factor is the set of known growth rate values, which is optimally obtained from measurements. The fact that the only limiting factor of the interpolation method is the four extreme growth rates in the Cartesian directions expands the applicability of this approach beyond SiC. It is very likely that the same interpolation method can be utilized for predicting oxidation growth rates for other semiconductor materials, which possess the same hexagonal crystal structure as SiC.

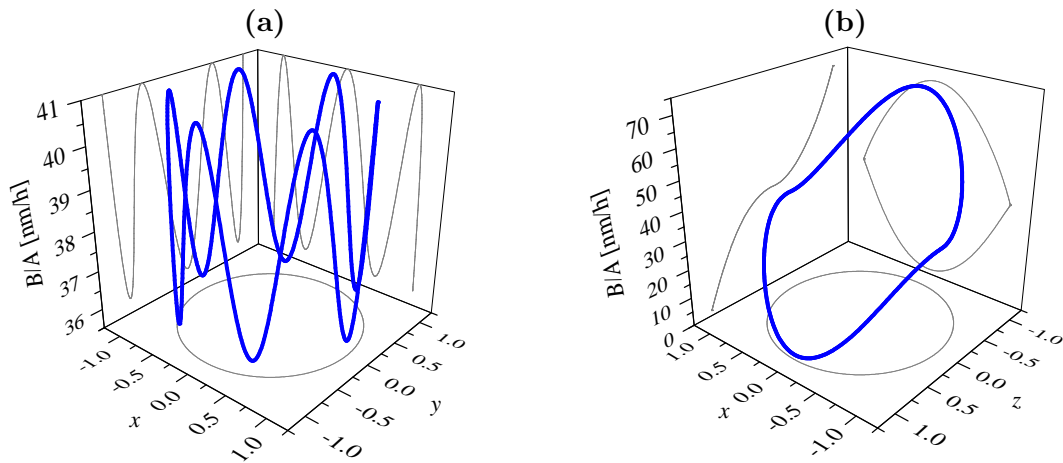


Figure 2.17: 2D calculations of the linear growth rates  $B/A$  in the (a)  $x$ - $y$  and (b)  $x$ - $z$  plane obtained with the explicit expression of the interpolation method.  $x$ ,  $y$ , and  $z$  are normalized crystal direction vector coordinates. The calculations are performed for oxidation at  $T = 1100^\circ\text{C}$ .

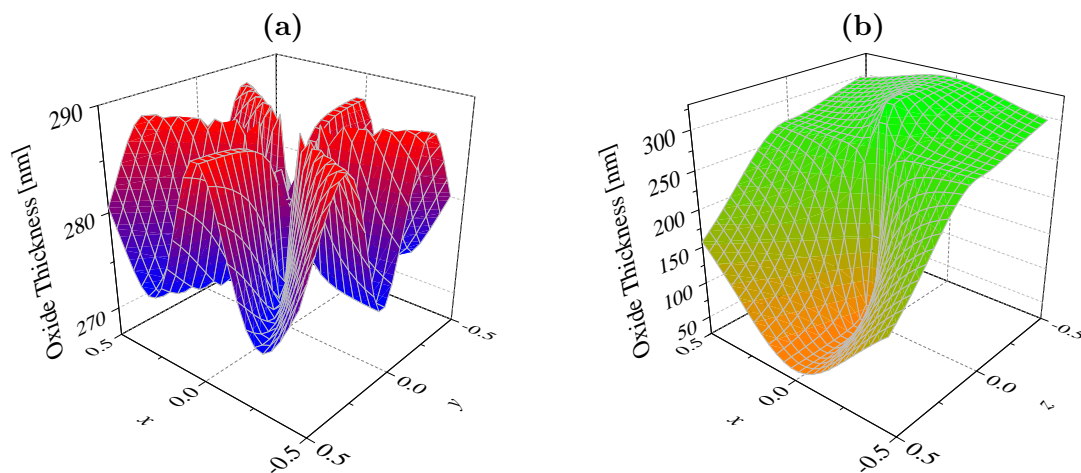


Figure 2.18: 2D calculations of the oxide thicknesses in the (a)  $x$ - $y$  and (b)  $x$ - $z$  plane. The figures show the final oxide thicknesses as a function of the normalized crystal direction vector coordinates  $x$ ,  $y$ , and  $z$ . The red, blue, orange, and green colors represent oxide thicknesses for the m-, a-, C-, and Si-face, respectively. The calculations are performed for oxidation at  $T = 1100^\circ\text{C}$  for 720 min.

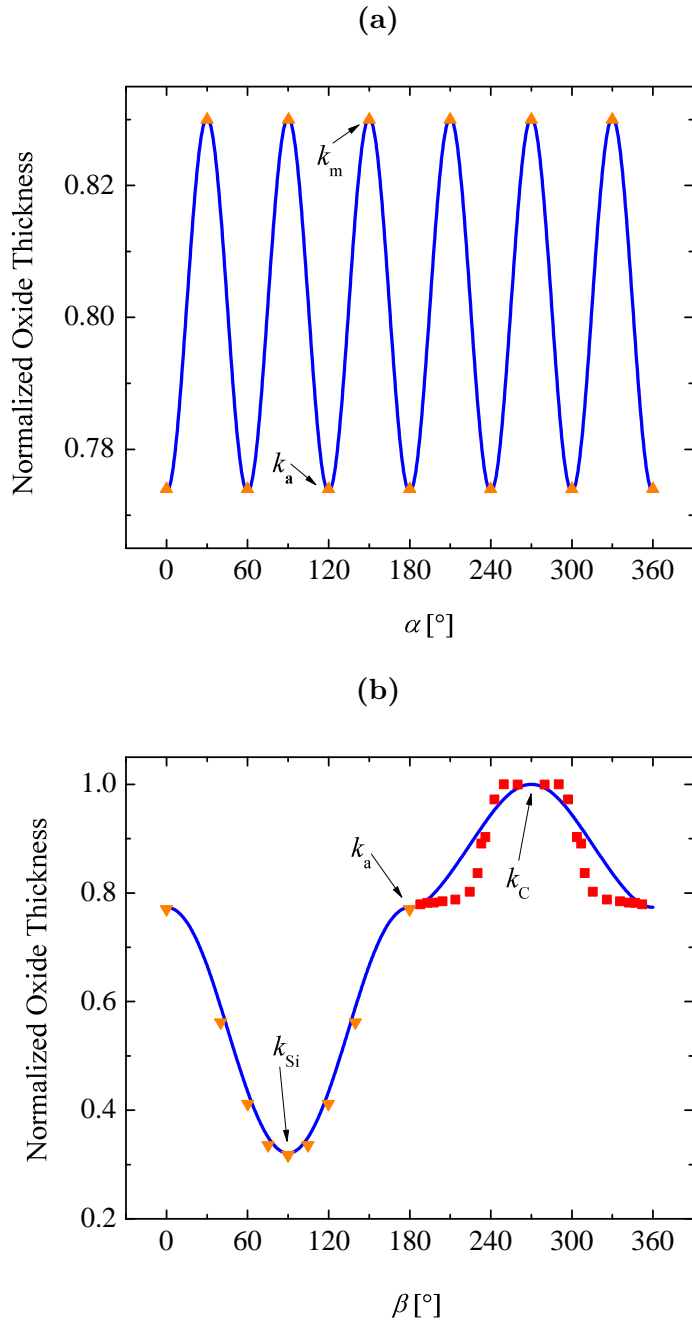


Figure 2.19: Normalized oxide thicknesses as a function of angle (a)  $\alpha$  in  $x$ - $y$  plane and (b)  $\beta$  in  $x$ - $z$  plane as shown in Figure 2.16. The oxide thickness is normalized with the maximal oxide thickness to enable a direct comparison between calculations and experiments. The blue solid lines are calculations performed with Massoud's model and the presented interpolation method. The orange triangles and red squares are measurement results [86], [88]. The black arrows indicate the known growth rates for the interpolation method, i.e.,  $k_m$ ,  $k_a$ ,  $k_{Si}$ , and  $k_C$ .

## 2.6 Orientation-Dependent Oxidation Model

Considering the above discussed Massoud's model (cf. Section 2.3.2), the calibrated oxidation growth rates (cf. Section 2.4.2), and the developed 3D interpolation method (cf. Section 2.5), the full expression of the orientation-dependent oxidation model is written as

$$\frac{dX(x, y, z)}{dt} = \frac{B}{A^{3D} + 2X} + C^{3D} e^{-\frac{x}{L^{3D}}}, \text{ with} \quad (2.62)$$

$$B = D_0 e^{\left(-\frac{E_a^{SD}}{k_B T}\right)} \mu\text{m}^2 \text{ min}^{-1}, \quad (2.63)$$

$$\begin{aligned} A^{3D} &= \frac{B}{B/A} = \\ &= B \left[ Z_{B/A}^{\text{a-face}} e^{\left(-\frac{E_{a,B/A}^{\text{a-face}}}{k_B T}\right)} \right. \\ &\quad + \left( Z_{B/A}^{\text{m-face}} e^{\left(-\frac{E_{a,B/A}^{\text{m-face}}}{k_B T}\right)} - Z_{B/A}^{\text{a-face}} e^{\left(-\frac{E_{a,B/A}^{\text{a-face}}}{k_B T}\right)} \right) f(x, y) \\ &\quad + \left. \left( Z_{B/A}^{\text{Si-face}} e^{\left(-\frac{E_{a,B/A}^{\text{Si-face}}}{k_B T}\right)} - Z_{B/A}^{\text{a-face}} e^{\left(-\frac{E_{a,B/A}^{\text{a-face}}}{k_B T}\right)} \right) z^2 \right]^{-1} \text{ for } z \geq 0 \text{ or} \\ &\quad + \left. \left( Z_{B/A}^{\text{C-face}} e^{\left(-\frac{E_{a,B/A}^{\text{C-face}}}{k_B T}\right)} - Z_{B/A}^{\text{a-face}} e^{\left(-\frac{E_{a,B/A}^{\text{a-face}}}{k_B T}\right)} \right) z^2 \right]^{-1} \text{ for } z < 0, \end{aligned} \quad (2.64)$$

$$\begin{aligned} C^{3D} &= Z_C^{\text{a-face}} e^{\left(-\frac{E_{a,C}^{\text{a-face}}}{k_B T}\right)} \\ &\quad + \left( Z_C^{\text{m-face}} e^{\left(-\frac{E_{a,C}^{\text{m-face}}}{k_B T}\right)} - Z_C^{\text{a-face}} e^{\left(-\frac{E_{a,C}^{\text{a-face}}}{k_B T}\right)} \right) f(x, y) \\ &\quad + \left( Z_C^{\text{Si-face}} e^{\left(-\frac{E_{a,C}^{\text{Si-face}}}{k_B T}\right)} - Z_C^{\text{a-face}} e^{\left(-\frac{E_{a,C}^{\text{a-face}}}{k_B T}\right)} \right) z^2 \text{ for } z \geq 0 \text{ or} \\ &\quad + \left( Z_C^{\text{C-face}} e^{\left(-\frac{E_{a,C}^{\text{C-face}}}{k_B T}\right)} - Z_C^{\text{a-face}} e^{\left(-\frac{E_{a,C}^{\text{a-face}}}{k_B T}\right)} \right) z^2 \text{ for } z < 0, \end{aligned} \quad (2.65)$$

$$\begin{aligned}
 L^{3D} = & Z_L^{\text{a-face}} e^{\left(-\frac{E_{\text{a,L}}^{\text{a-face}}}{k_B T}\right)} \\
 & + \left( Z_L^{\text{m-face}} e^{\left(-\frac{E_{\text{a,L}}^{\text{m-face}}}{k_B T}\right)} - Z_L^{\text{a-face}} e^{\left(-\frac{E_{\text{a,L}}^{\text{a-face}}}{k_B T}\right)} \right) f(x, y) \\
 & + \left( Z_L^{\text{Si-face}} e^{\left(-\frac{E_{\text{a,L}}^{\text{Si-face}}}{k_B T}\right)} - Z_L^{\text{a-face}} e^{\left(-\frac{E_{\text{a,L}}^{\text{a-face}}}{k_B T}\right)} \right) z^2 \text{ for } z \geq 0 \text{ or} \\
 & + \left( Z_L^{\text{C-face}} e^{\left(-\frac{E_{\text{a,L}}^{\text{C-face}}}{k_B T}\right)} - Z_L^{\text{a-face}} e^{\left(-\frac{E_{\text{a,L}}^{\text{a-face}}}{k_B T}\right)} \right) z^2 \text{ for } z < 0,
 \end{aligned} \tag{2.66}$$

and

$$f(x, y) = (2(x^2 + y^2)^3 - (x^2 + y^2)^4 - x^2(x^2 - 3y^2)^2). \tag{2.67}$$

$x$ ,  $y$ , and  $z$  are vector coordinates for the desired direction of oxidation. The subscripts B/A, C, and L refer to Massoud's model parameters. This modified oxidation model enables to fully simulate thermal oxidation of arbitrary 2D and 3D structures with a high precision in all crystal directions. The orientation-dependent oxidation model (i.e., the calibrated parameters and the interpolation method) was implemented into Silvaco's Victory Process simulator [53] and is evaluated in the following section based on 3D simulations of SiC thermal oxidation for various simulation setups.

### 2.6.1 Process Simulations

An exemplary 3D simulation of the thermal oxidation of an arbitrary SiC structure is shown in Figure 2.20 and its 2D cross-sections in Figure 2.21. The simulation results clearly demonstrate that the oxide thickness on the C-face is the thickest and the oxide on the Si-face is the thinnest. The oxide in the  $x$  direction, i.e., m-face, is approximately 10% thicker than the oxide in the  $y$  direction, i.e., a-face. Despite the fact that the thickness difference of the m- and the a-face seems negligible, the small variations in the oxide thicknesses still play a significant role in the design of MOS devices, in particular for non-planar devices such as U-MOSFET [107], due to the high oxide thickness-dependent device characteristics.

Figure 2.22 depicts additional 3D simulations by using a sphere-shaped plot for direct comparison with measurement results [88]. The shown optical micrographs have been obtained with Rutherford backscattering spectrometry (RBS). The SiO<sub>2</sub> thickness is determined based on the width of the RBS spectrum corresponding to Si atoms in SiC and O atoms in SiO<sub>2</sub>. The experimental results show a remarkable anisotropic coating with SiO<sub>2</sub>, which can be seen from the optical micrographs, i.e., spheres.

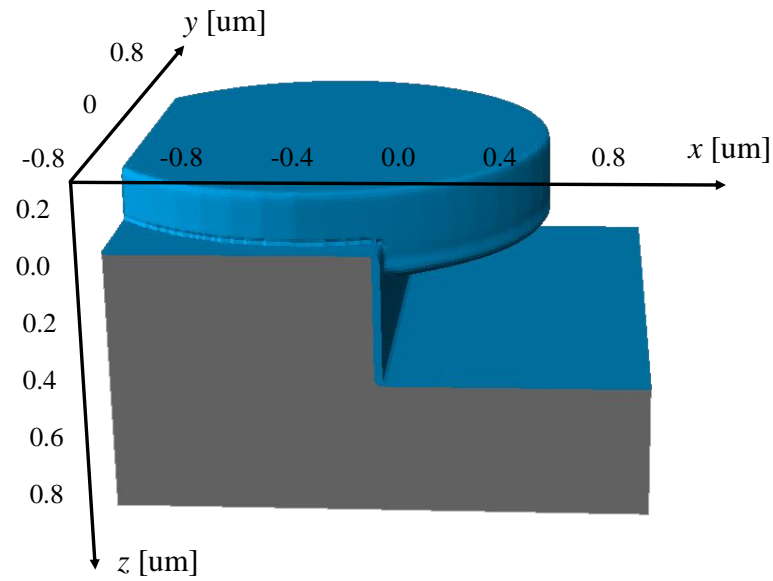


Figure 2.20: 3D simulation of dry thermal oxidation of SiC. The simulation is performed for the (0001) Si-face at  $T = 1100^\circ\text{C}$  for 120 min. The gray areas represent 4H-SiC and the blue areas the grown  $\text{SiO}_2$ .

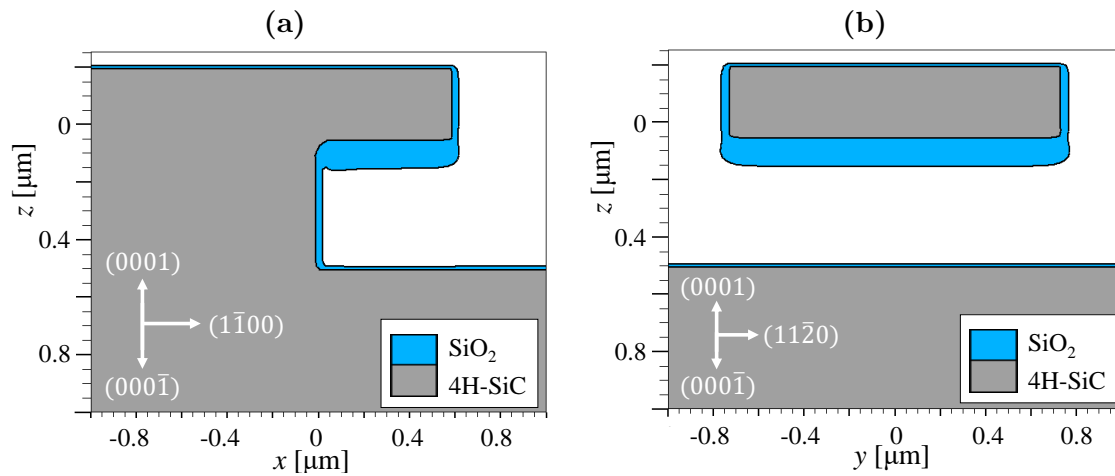


Figure 2.21: 2D cross-sections of the conducted 3D simulations of dry thermal oxidation (cf. Figure 2.20). **(a)**  $x$ - $z$  cross section at  $y = 0.0 \mu\text{m}$  and **(b)**  $y$ - $z$  cross section at  $x = 0.2 \mu\text{m}$ . Note the different oxide thicknesses based on different directions.

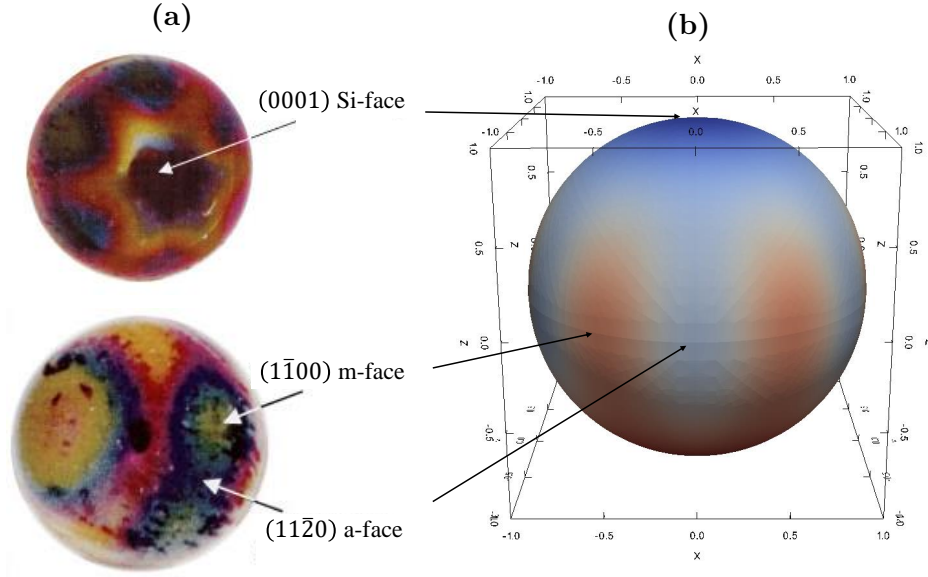


Figure 2.22: **(a)** Measurement results (optical micrographs) of an oxidized SiC from Christiansen *et al.* [88]. The contrast of colors is due to the light interference with the different oxide thickness. **(b)** The sphere of SiC oxide thicknesses obtained with the developed interpolation-based modeling method. The colors represent calculated thicknesses towards corresponding crystal directions. The simulations have been performed for (0001) Si-face at  $T = 1100^\circ\text{C}$  for 720 min.

The experimental study has thus identified the two polar regions (assigned to the Si- and C-face) and an equatorial zone, which shows six maxima and six minima. It was determined that the maximum of the oxide thickness corresponds to the m-face and the minimum to the a-face. Therefore, a six-fold symmetry yields a star-shaped directional dependence. This observation indicates that the initial assumption of the interpolation method, i.e., a symmetric star shape in the  $x$ - $y$  plane and a tangent-continuous union of two half-ellipses in  $z$  direction, are equitable.

Another analysis evaluates a step-like shape of a SiC substrate, which is reproduced from the experimental work of Hosoi *et al.* [108] to establish a frame of reference. The experimental research utilized atomic force microscopy (AFM) to measure the SiC surface thickness before and after oxidation. The thermal oxidation, in both experiment and simulation, is performed for the most common industry-related SiC oxidation setup, i.e., a (0001) Si-face substrate with  $4^\circ$  off-axis angle in a dry ambient at  $1100^\circ\text{C}$ , shown in Figure 2.23.

It is clearly seen from the results that the oxidation in the direction of the a-face is stronger than in the direction of the Si-face. The time evolution confirms that the SiC/SiO<sub>2</sub> interface is heavily influenced by oxidation mechanisms [109], i.e., the interface is deformed and moves towards inside the substrate for  $\approx 0.15 \mu\text{m}$  within 720 min.

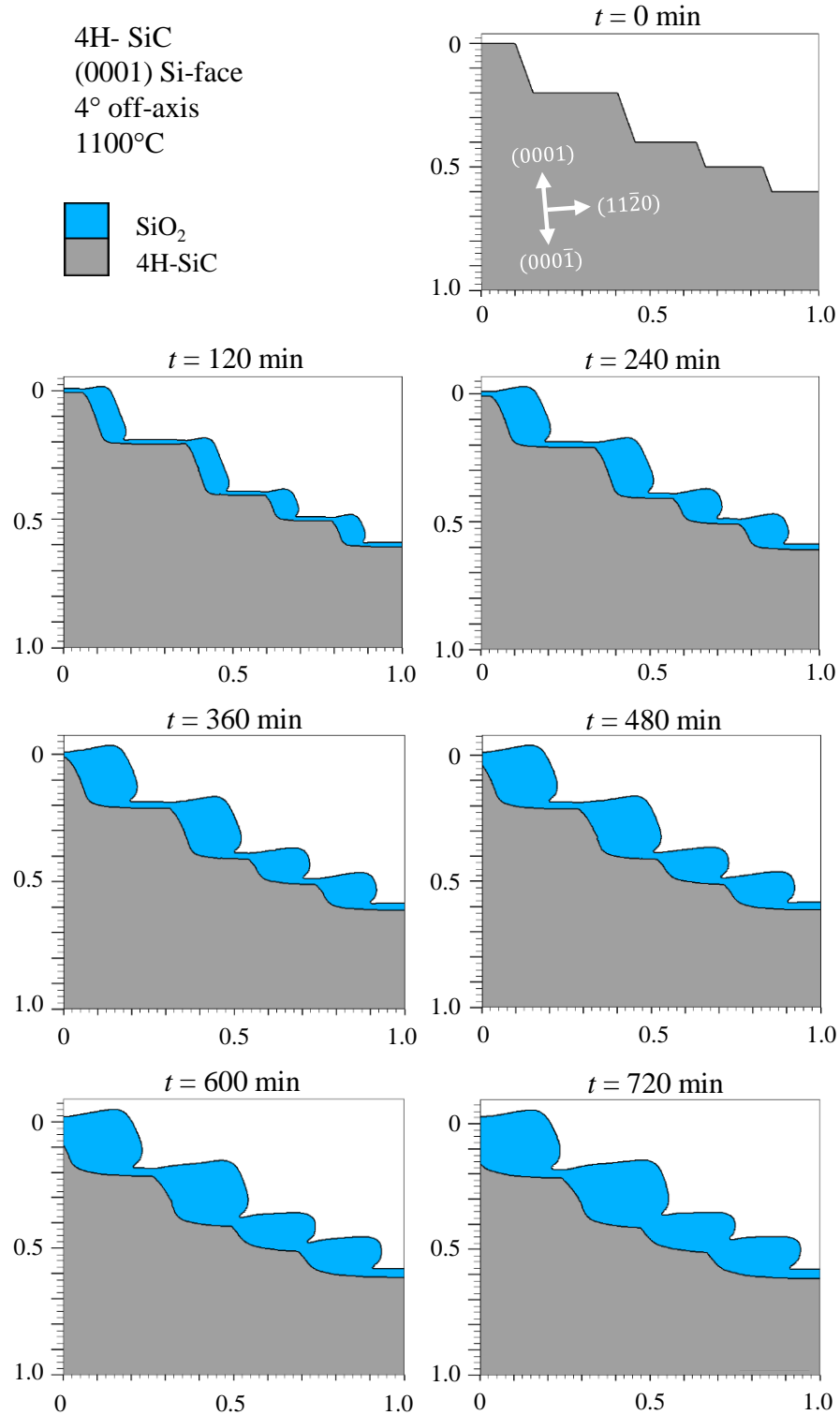


Figure 2.23: Simulations of thermal oxidation of a step-like shaped 4H-SiC. The simulation is performed for a (0001) Si-face 4° off-axis substrate at  $T = 1100^\circ\text{C}$ . The results show the time evolution of the SiC oxidation for every 120 min. The gray and the blue shapes refer to the 4H-SiC and SiO<sub>2</sub>, respectively.

Comparing the simulation results with the measurement results [108] demonstrates a very good agreement, justifying the importance of the calibrated oxidation growth rate parameters and the discussed multi-dimensional interpolation method.

The final verification is based on transmission electron microscopy (TEM) measurements of a macrostep at the  $\text{SiO}_2/\text{SiC}$  interface from Woerle *et al.* [110]. Epitaxial layers formed by step-controlled epitaxial growth are an important example of a surface requiring a substrate cut, which is several degrees off-angle for high-purity epitaxies [111]. At the same time, however, this growth technique can lead to the formation of several nanometer high macrosteps [112], [113] with faces perpendicular to either the (0001) or  $(11\bar{2}0)$  direction. The TEM image of the  $\text{SiO}_2/\text{SiC}$  interface and the corresponding results from simulations are shown in Figure 2.24.

A TEM analysis of  $4^\circ$  off-axis (0001) Si-face 4H-SiC with a  $5\ \mu\text{m}$  thick n-type epitaxial layer has been performed. The substrate has been first cleaned and then oxidized in dry ambient at  $1050^\circ\text{C}$  for 4 hours. In order to protect the  $\text{SiO}_2$  during lamella preparation, a 500 nm thick aluminium layer has been deposited on the oxide before the focused ion-beam treatment. The TEM lamella has been oriented along  $(11\bar{2}0)$  direction, perpendicular to the step-flow of the epitaxial layer and taken from a region of the sample where isolated macrosteps were present. From the TEM image, the oxide thickness at the terrace and riser were determined to be 7 nm and 11 nm, respectively.

In parallel to the experimental investigation, the oxidation growth process has been simulated using the developed modeling approach and the Victory Process simulator. The results predict the oxide thickness at the terrace and riser to be 7.54 nm and 11.2 nm, respectively: These results are in good agreement, in particular at the riser (cf. Figure 2.24). Finally, the experimental results suggest that variations in the oxide thickness due to the surface morphology of off-axis 4H-SiC epilayers must be considered for a complete picture of the reliability-limiting factors of thermally grown oxides on SiC [110].

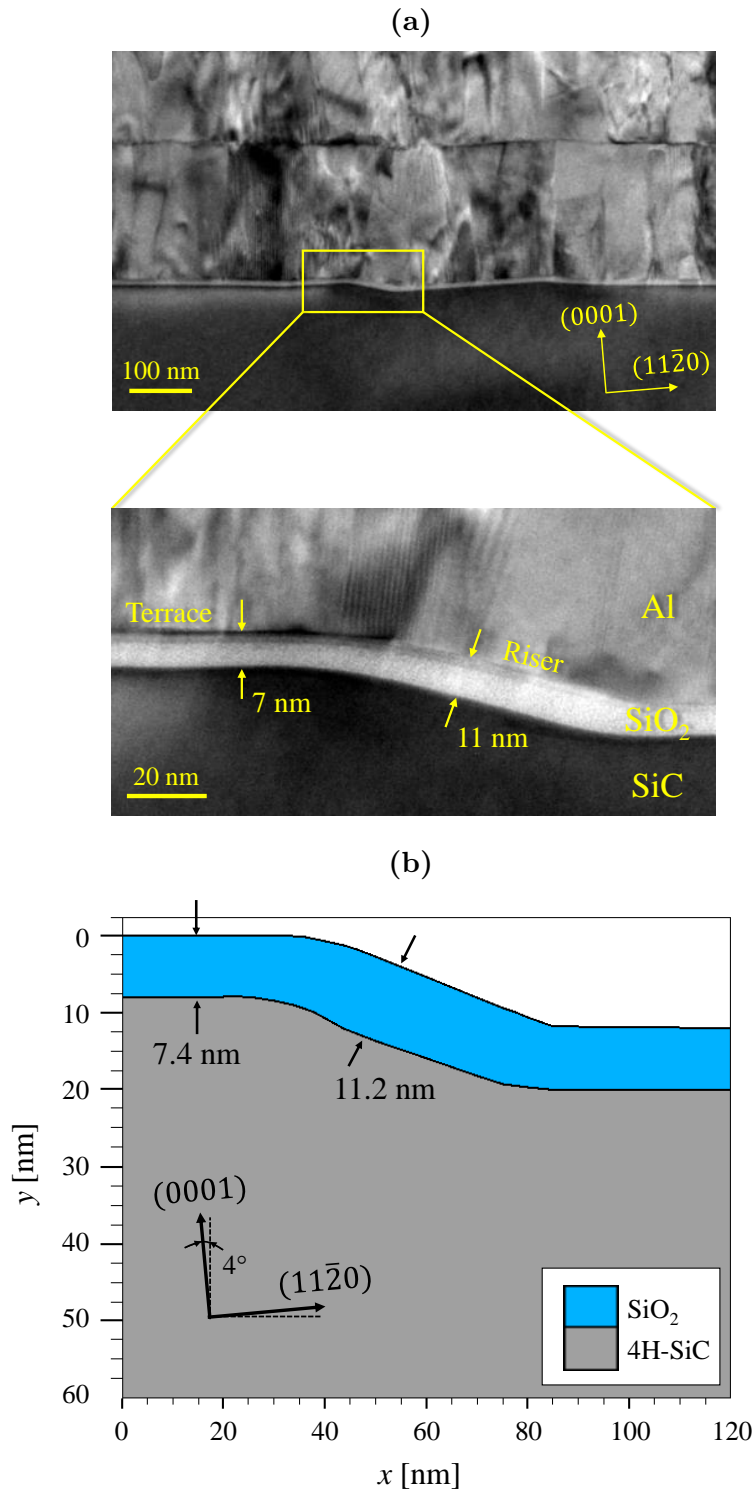


Figure 2.24: (a) TEM cross-section of the SiO<sub>2</sub>/SiC interface and the close-up image of a macrostep [110]. (b) Results of the oxide growth simulations for this specific surface morphology, showing a good agreement with the measured oxide thicknesses.

## 2.7 Molecular Dynamics Simulations of Orientation Dependences

Heretofore, the macroscopic oxidation models, parameters, and methods to improve 2D and 3D simulations have been discussed, but not the oxidation kinetics on the atomistic level. Within this work's context, molecular dynamics (MD) simulations enable first principles investigations of the early stages of the oxidation process, where experimental methods fail to provide the necessary data, due to technical limitations. The main limitation of oxide thickness measurements is a low accuracy of measurements of the oxide growth on very short time scales or oxide thicknesses below 5 nm. The first principles approach is thus essential in order to further develop macroscopic physical models and to estimate initial oxide thicknesses for macroscopic models.

Computational methods on atomic or molecular levels provide powerful ways to explore, develop, and optimize novel materials. Such methods, commonly based on quantum mechanics (QM) [114], are computationally very expensive and can thus be reasonably applied only to small-sized atomic systems, typically containing a few tens of atoms. To overcome this issue, QM structure and energy data can be used to train empirical force fields in order to reduce the computational effort [76]. Therefore, a novel empirical reactive force-field (ReaxFF) method [115], [116] can be utilized. The ReaxFF method replaces harmonic bonds of conventional MD with bond orders and energies that depend on interatomic distances, which thus reduces simulation time by several orders of magnitude [117], [118], [119], [120].

The parameters involved in the ReaxFF potential functions must be parametrized against high-level *ab initio* calculations and experimental results. The potentials for the atoms involved in the SiC oxidation, i.e., Si/C/O, have been previously developed, calibrated, and parametrized [76], [121], [122]. State-of-the-art implementations of ReaxFF, e.g., provided by the large-scale atomic/molecular massively parallel simulator (LAMMPS) [123], have demonstrated reasonable computational efficiency and accuracy. Furthermore, LAMMPS is distributed as an open-source code and supports parallel computing via OpenMP and MPI. In order to take advantage of the parallel computing features, the analyses presented in the following were executed on the Vienna Scientific Cluster (VSC-3) [124], which consists of 2020 nodes, each equipped with two 8-core Intel Xeon E5-2650v2 2.6 GHz processors (total of 16 physical/32 logical cores per node) and 64 GB of main memory.

An evaluation of the parallelization backends of LAMMPS (i.e., USER-OMP package, including OpenMP and MPI) shows better performance with a pure MPI approach, compared to using a hybrid MPI - OpenMP approach. The benchmark of an example MD simulation for various atom numbers is shown in Figure 2.25. Despite the relatively low parallel efficiency of the simulations (i.e., 35 % in the best case), the LAMMPS' USER-OMP package enables a significant reduction of the overall simulation runtime (e.g., from 18 days to 4 days for  $10^4$  particles).

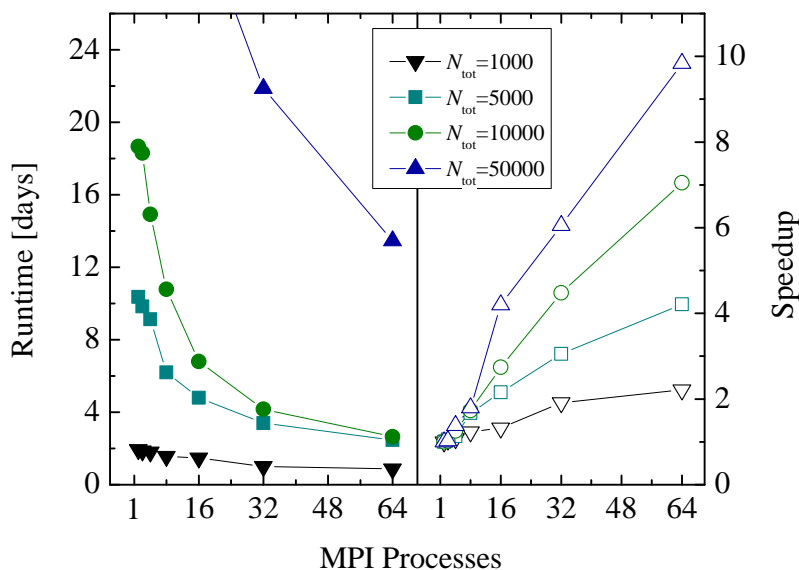


Figure 2.25: Runtime and speedup of LAMMPS simulations as a function of MPI processes for various total number of atoms  $N_{tot}$ . The benchmarks have been recorded on VSC-3 for pure MPI, i.e., 1 OpenMP thread and 16 MPI processes per core.

### 2.7.1 Simulation Setup

The goal is to investigate several layers of  $\text{SiO}_2$  and to shed light on the oxide growth differences of various SiC orientations. Therefore, 1 ns oxide growth is simulated with  $2 \cdot 10^6$  timesteps using a step size of 0.5 fs. The number of atoms involved in the simulations must be properly limited in order to be able to perform the desired number of timesteps. On the other hand, the number of  $\text{O}_2$  molecules must be high enough to ensure a constant gas flow. For this reason, numerous control simulations have been performed with respect to various simulation sizes to ensure that the product gases in the air do not further affect the oxidation and that an adequate number of  $\text{O}_2$  molecules is available at every timestep of the simulation. The initial structure setup consists of approximately 10 SiC layers in  $x$  and  $y$  directions and 27 SiC layers in  $z$  direction. The space on top of the substrate is three times the height of the crystal with uniform random distribution of  $\text{O}_2$  molecules, indicating dry air conditions for the thermal oxidation. The schematic representation of the  $3 \cdot 3 \cdot 24 \text{ nm}^3$  simulation domain is shown in Figure 2.26. The total number of particles in all simulations is approximately  $10^4$ , out of which  $\approx 3600$  are Si and C atoms. The surfaces of SiC are not initially passivated, as the passivated surfaces could affect the investigation of the orientation dependence of the initial oxidation growth rates [125].

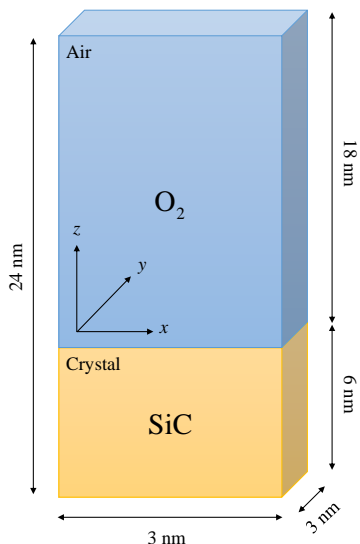


Figure 2.26: Schematic representation of the simulation setup. The simulation domain is composed of two cuboids, namely air and crystal. The air includes only  $O_2$  molecules and the crystal only SiC compounds.

All simulations are performed in the canonical ensemble, depending on the absolute temperature, number of particles, and volume (NVT). The boundary conditions are periodic in  $x$  and  $y$  directions and reflective in  $z$  direction, to avoid undesired oxidation on the bottom of the substrate. The temperature of the simulations is controlled with the Berendsen thermostat [126] with a temperature damping constant of 100 fs. Simulations are performed with four common industry-focused oxidation temperatures:  $T = 900, 1000, 1100,$  and  $1200^\circ\text{C}$ . In order to investigate orientation dependence, four different initial structures are prepared, which represent the four considered SiC faces, shown in Figure 2.27.

## 2.7.2 Simulation Results and Analyses

The structural evolution of the SiC/ $O_2$  system is shown in Figure 2.28 for  $10^3, 10^4, 10^5,$  and  $10^6$  fs, respectively. The time evolution clearly shows all of the oxidation process steps: 1) transport of  $O_2$  to the oxide surface, 2) in-diffusion of  $O_2$  through the oxide film, 3) reaction of  $O_2$  and SiC at the  $SiO_2/SiC$  interface, 4) out-diffusion of carbon oxide (CO) through the oxide film, and 5) removal of the product gases away from the oxide surface. To follow the oxidation process, the number of O atoms in the SiC crystal ( $N_O^{SiC}$ ) and air ( $N_O^{Air}$ ) is analyzed. The evolution of the O atoms reacting with the SiC structure for the four crystallographic faces at  $T = 900, 1000, 1100,$  and  $1200^\circ\text{C}$  is shown in Figure 2.29.

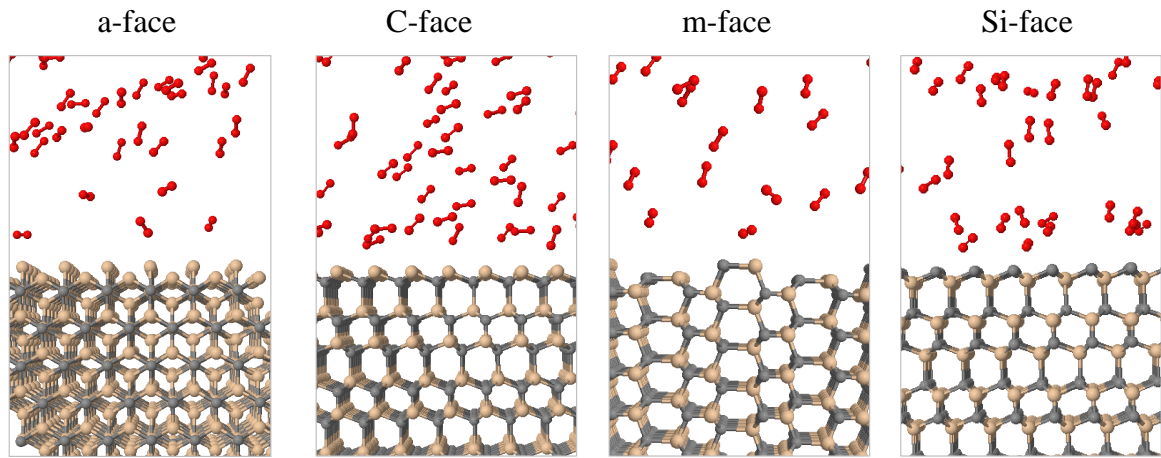


Figure 2.27: Simulation snapshots of initial structures of the SiC/O<sub>2</sub> interfaces for a- ( $11\bar{2}0$ ), C- ( $000\bar{1}$ ), m- ( $1\bar{1}00$ ), and Si- ( $0001$ ) oriented SiC at time=0.

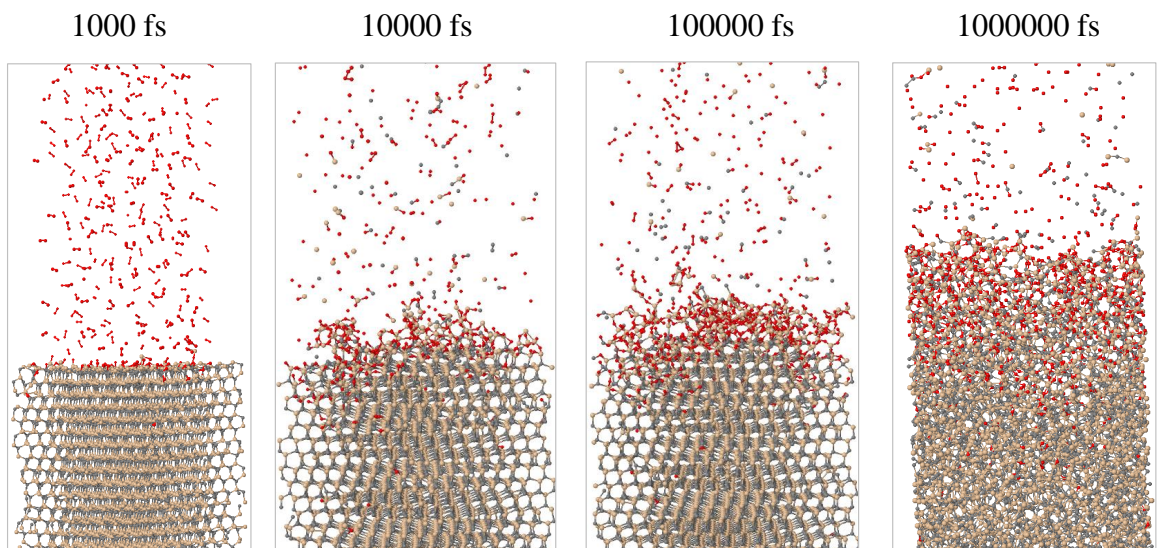


Figure 2.28: Simulation snapshots of the structural evolution of the SiC ( $0001$ ) Si-face oxidation process for  $t = 10^3$ ,  $10^4$ ,  $10^5$ , and  $10^6$  fs at  $T = 1100^\circ\text{C}$ . The timestep is 1 fs.

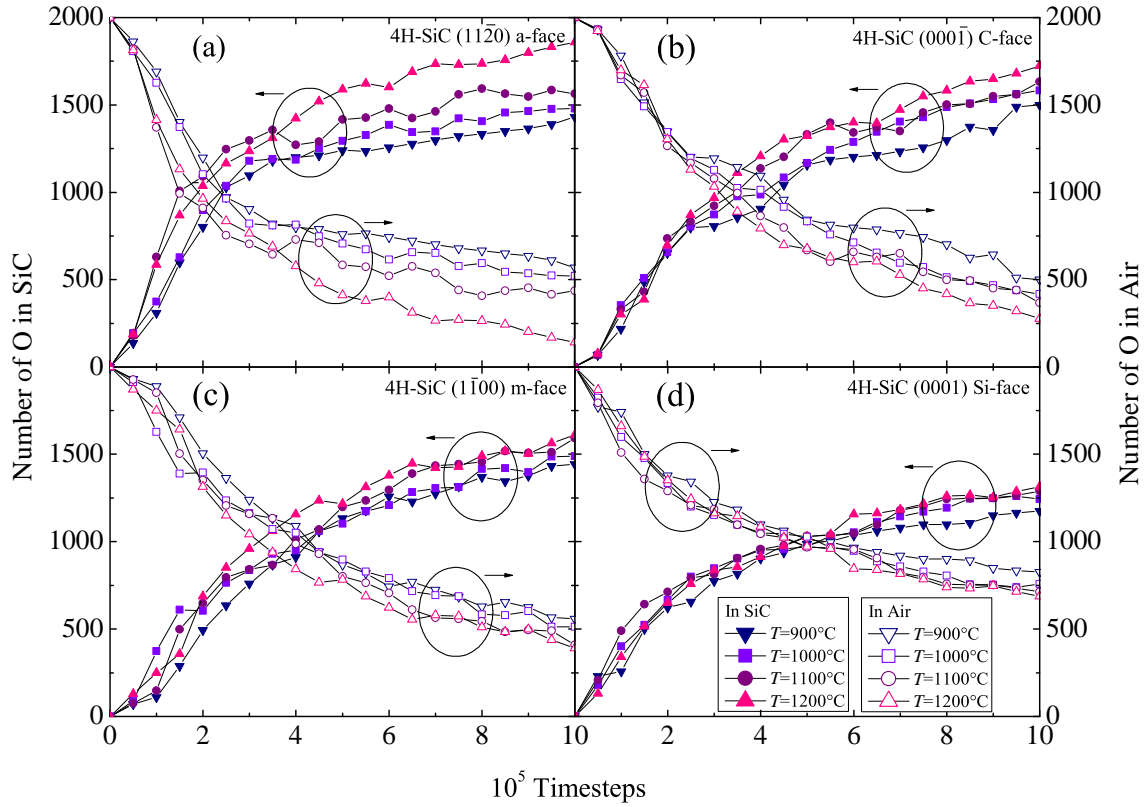


Figure 2.29: Time evolution of the number of O atoms in the SiC crystal (closed symbols, left axis) and air (open symbols, right axis) for the (a) a-, (b) C-, (c) m-, and (d) Si-face. The colors refer to various oxidation temperatures in the range from 900 to 1200°C.

It is clearly evident that the concentration of the O atoms in SiC is increasing with time, which indicates a successful oxidation process. As the  $\text{SiO}_2$  is formed on top of the crystal, the chemical reaction is passivated, which is evident by the decreasing slope of the curves. The formed oxide affects the in-diffusion of the  $\text{O}_2$  and the out-diffusion of the product gases through the oxide film, therefore, the oxidation process is decelerated.

Another essential figure of merit is the time evolution of the number of Si ( $N_{\text{Si}}^{\text{SiC}}$ ) and C ( $N_{\text{C}}^{\text{SiC}}$ ) atoms in the SiC crystal. The results for the four SiC faces and for the four investigated temperatures are shown in Figure 2.30. Si and C in this case are traced as single atoms, but are in fact diffused out of the crystal as product gases. The oxidation temperature clearly affects the diffusion of the Si, C, and O species, which confirms that even the early stage of the oxidation mechanism, i.e.,  $< 1$  ns, is temperature-dependent.

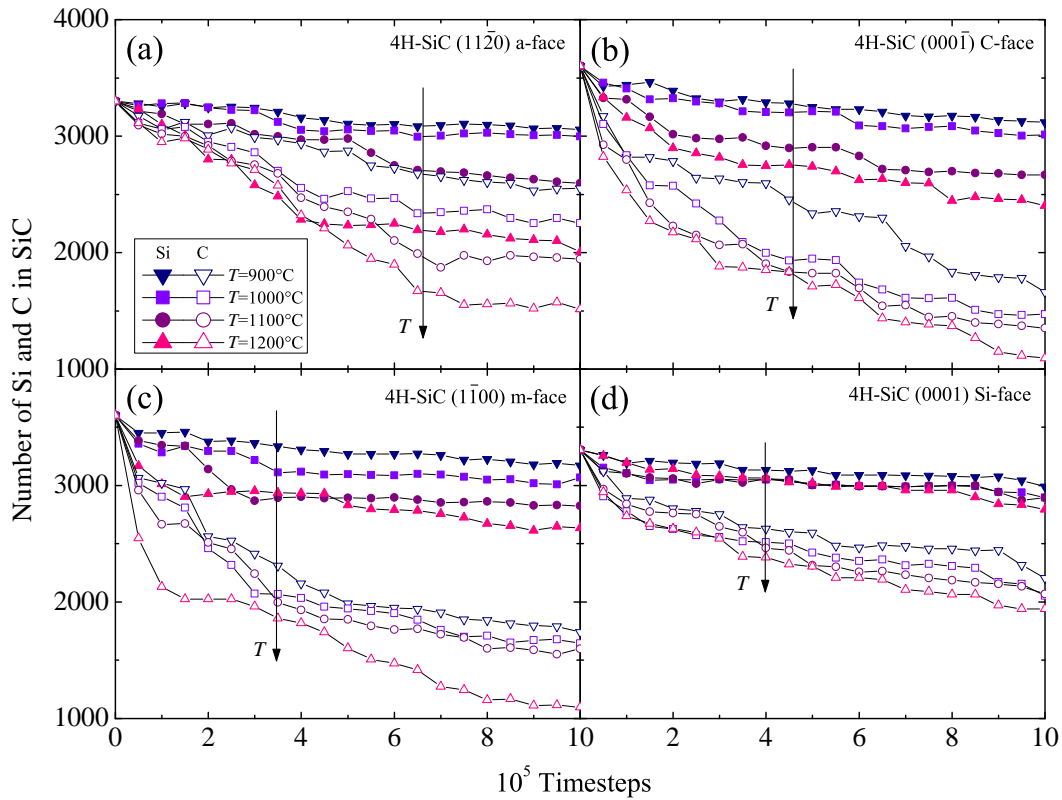


Figure 2.30: Time evolution of the number of Si (closed symbols) and C (open symbols) atoms in the SiC crystal for the (a) a-, (b) C-, (c) m-, and (d) Si-face. The colors refer to various oxidation temperatures in the range from 900 to 1200°C.

The Figure 2.30 additionally suggest that the out-diffusion of the C interstitials is higher than the one of the Si interstitials. This is in agreement with previous reports [69] and confirms the assumption of the Si and C emission model [75], [102], that the accumulation of the C interstitials becomes saturated prior to that of the Si interstitials. In addition, C and Si emission suppresses the interfacial reaction rate during oxidation.

The impact of the anisotropy on the oxide thickness is further investigated for the particular case of 1100°C, as seen in Figure 2.31 for the four crystallographic faces. The oxide thickness is calculated for each time step of the simulation. The results show that even after a very short time of oxidation (i.e., 1 ns) the thickness of the oxide grows up to 2.7 nm. This suggests that the initial oxidation is taking place almost instantaneously relative to the industry-focused oxidation times and clarifies the assumption of the macroscopic models [70], [72], [75], that the oxide thickness at  $t = 0$  is approximately 2-5 nm.

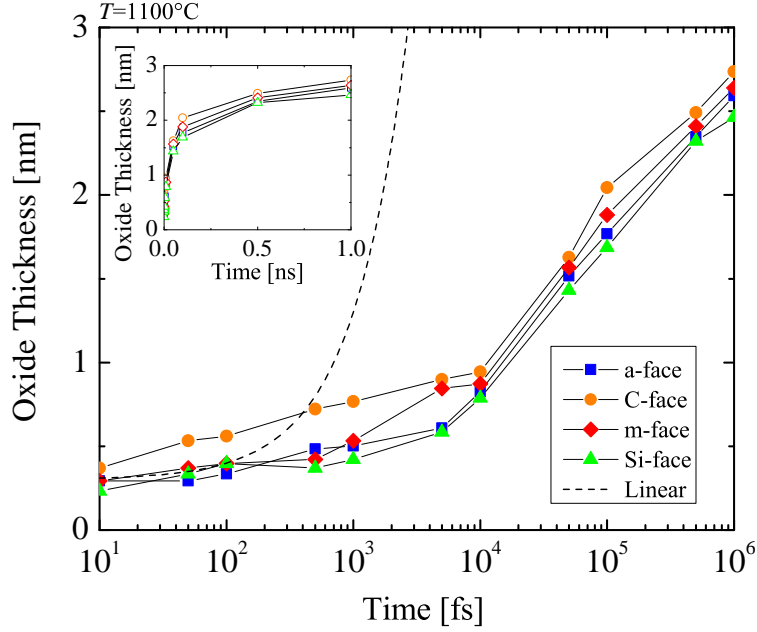


Figure 2.31: Time evolution of the oxide thickness for the a-, C-, m-, and Si-face at  $T = 1100^\circ\text{C}$ . The dashed line shows a symbolic assumption of inaccurate linear growth of the  $\text{SiO}_2$  thickness. The inset figure uses a linear  $x$  axis.

A symbolic linear growth rate (dashed line) with the slope of  $1 \cdot 10^{-3}$  nm/fs and the intercept 0.3 nm highlights the difference between the simulation results and a hypothetical but inaccurate linear assumption. This clearly shows that a linear growth rate cannot be assumed. Comparing the oxide evolution with linear growth, it is evident that the growth rate is significantly reduced as the oxide layer grows. Thus, it can be concluded that the relationship between the oxide thickness and time is non-linear for the early stage of the oxidation.

In addition, the emitted Si and C species are normalized as  $R_{\text{Si}} = N_{\text{Si}}^{\text{emitted}}/N_{\text{Si}}^{\text{tot}}$  and  $R_{\text{C}} = N_{\text{C}}^{\text{emitted}}/N_{\text{C}}^{\text{tot}}$ , respectively, where  $N^{\text{emitted}}$  is the number of emitted and  $N^{\text{tot}}$  the total number of Si or C. The time evolution of the normalized emission and the emission rates of Si and C are shown in Figure 2.32. The results suggest differences between the four crystallographic faces and indicate that  $R_{\text{C}}$  is approximately three times higher than  $R_{\text{Si}}$  across the whole time scale. An unexpected peak has been observed for the emission rates between 10 and 100 ps, regardless of the crystal orientation. It appears, that at times  $< 10$  ps the oxidation mechanism does not yet require an emission of the Si and C species. On the other hand, for times  $> 100$  ps the emission is considerably decelerated due to the formation of the  $\text{SiO}_2$  layer. However, the oxidation rate appears not to be limited by the diffusion of the Si and C interstitials, but is limited by the reaction of the surface oxidation.

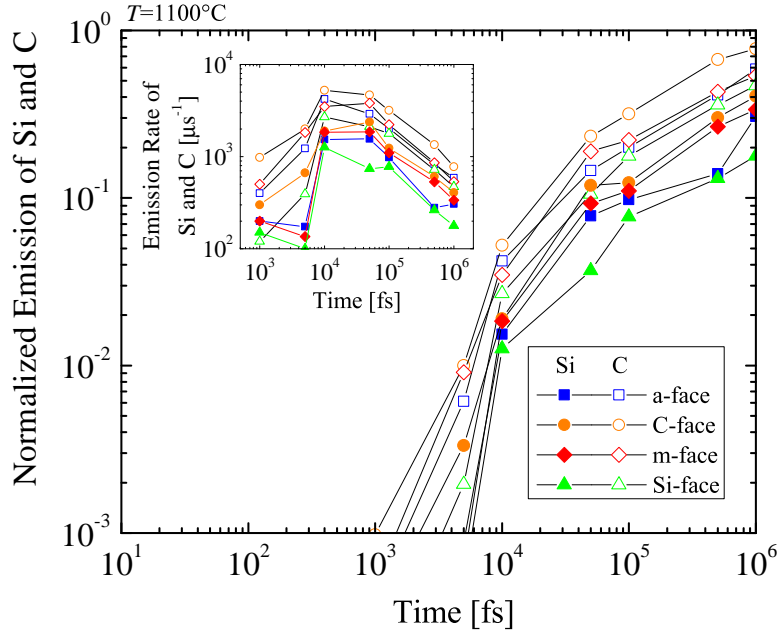


Figure 2.32: Time evolution of the emitted Si (closed) and C (open symbols) atoms for the a-, C-, m-, and Si-face at  $T = 1100^\circ\text{C}$ . The inset figure shows the emission rates of Si and C.

To investigate the orientation-dependent oxidation further, the growth rates of SiC oxidation ( $dX/dt$ ) [127] are calculated at  $t = 10^1, 10^2, 10^3, 10^4, 10^5,$  and  $10^6$  fs, respectively, as shown in Figure 2.33. It is evident, that the oxidation rate decreases exponentially with time. In fact, the growth rates are extremely high at the beginning, when the oxide layer has not been formed yet due to the absence of rate limiting barriers, such as, e.g., substantial mass transport. Therefore, the rates are comparable with the relative movement of the  $\text{O}_2$  molecules in air. The orientation dependence of the SiC oxidation is evident during the entire simulation. In particular, the C-face has by far the highest growth rate, followed by the m- and the a-face, and finally the Si-face with the lowest oxidation rate. This sequence is consistent with the currently available macroscopic models [63], [70], [72] and experimental findings [87], [89], [90]. Normalized growth rates show that the orientation dependence is highest at the beginning and decreases with the growing oxide. This implies, that the passivation of the oxidation mechanism due to the in-diffusion of  $\text{O}_2$  and the out-diffusion of product gases through the grown oxide layer is not orientation-dependent. Goto *et al.* [70] suggested that the growth rates of the surface oxidation of SiC correspond to the number of Si-C broken bonds, i.e., one Si-C back-bond for the C-face, two Si-C back-bonds for the a-face, and three Si-C back-bonds for the Si-face, yielding growth rate ratios of the C-face : a-face : Si-face close to 1 : 2 : 3. The results for the different crystal structures from the simulations in Figure 2.27 are in agreement with assumptions from macroscopic modeling.

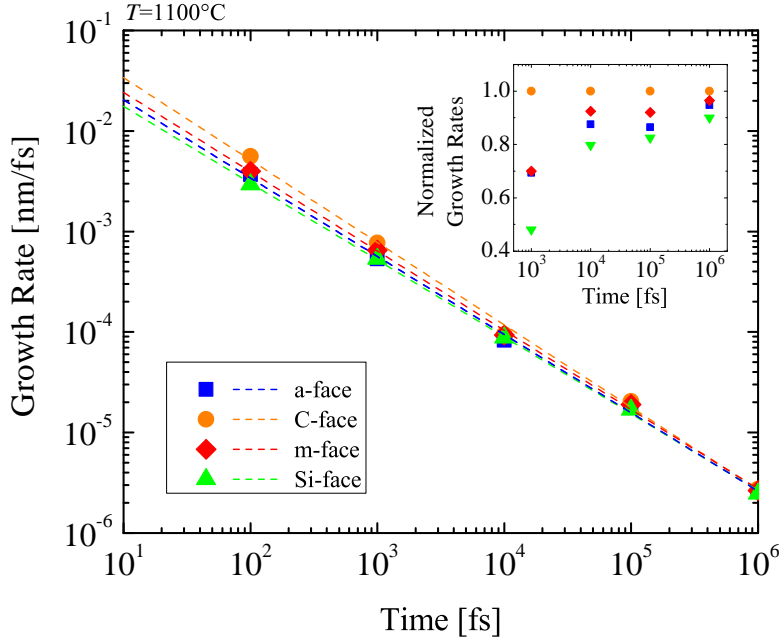


Figure 2.33: Time evolution of the oxidation growth rate for the a-, C-, m-, and Si-face at  $T = 1100^\circ\text{C}$ . The dashed lines are best linear fits of the log-log figure to guide the eye. The inset figure shows normalized growth rates according to the SiC orientation.

Referring back to Figures 2.29 and 2.30, equivalent ratios between the three faces are observed. On the other hand, the reason for the growth rates for the m-face being 5 – 10% higher than for the a-face is still not fully understood and should be investigated further. Homo-epitaxial layers of m-face SiC are currently not available, therefore, experimental findings are not available.

In addition, growth rates as a function of the oxide thicknesses are calculated for temperatures  $T = 900, 1000, 1100,$  and  $1200^\circ\text{C}$ , shown in Figure 2.34. The results show that the growth rates below 3 nm are extremely high and decrease exponentially. The slopes of the curves do not decrease, which, according to the Si and C emission theory [75], suggests that the surface oxidation is the rate limiting step, rather than the interface oxidation or diffusion. Note, for thin oxides (below 10 nm) the rate-limiting step cannot be exactly determined. Unfortunately, comparing MD results to results from macroscopic models [63], [70], [75] is not possible, as these focus on thicknesses above 10 nm, which is not feasible with current first principles simulation capabilities due to the required simulation times in the regime of several months.

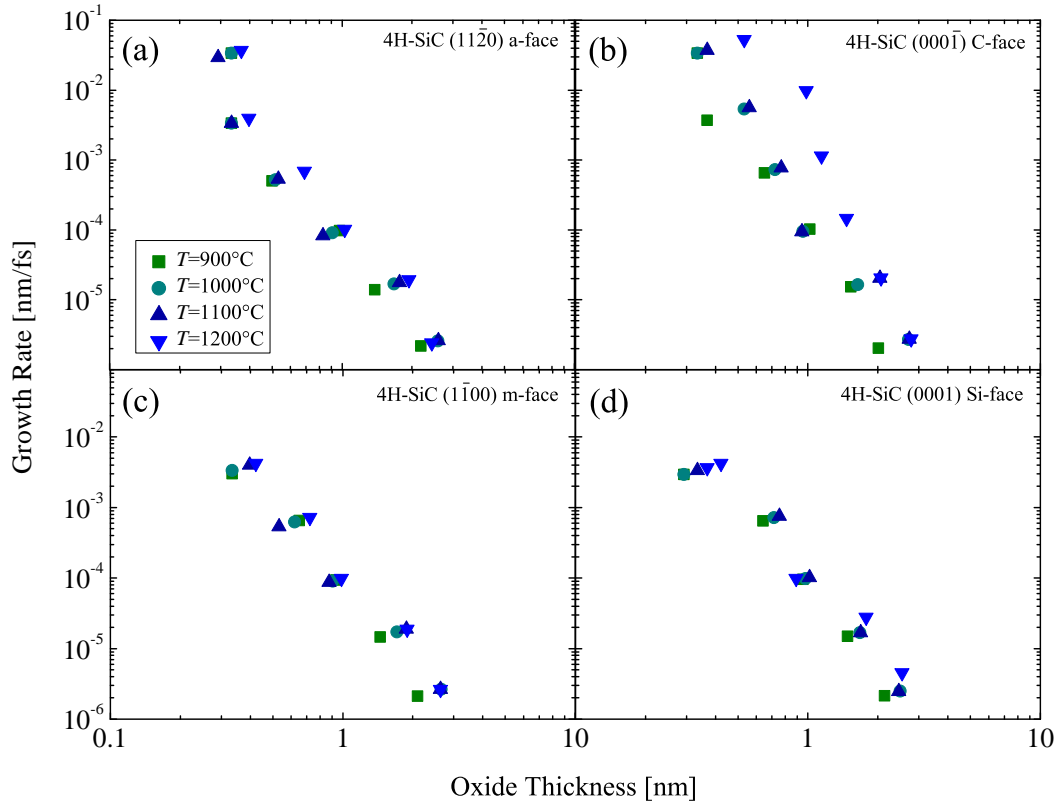


Figure 2.34: Growth rate of the oxidation process as a function of the oxide thickness for the (a) a-, (b) C-, (c) m-, and (d) Si-face. The colors refer to various oxidation temperatures in the range from 900 to  $1200^{\circ}\text{C}$ .

To summarize, the discussed findings prove that MD simulations contribute to the development of orientation-dependent SiC oxidation models [73], which are in turn fundamental for device fabrication simulators, e.g., Silvaco's Victory Process simulator [53]. As has been pointed out already in several instances, it is crucial for device fabrication modeling to accurately predict oxidation growth of SiC by incorporating the geometry of the oxide. In addition, the presented results promote the advancement of the theory of SiC oxidation. As an outlook, investigations of various oxidation atmospheres, e.g., nitric oxide (NO) [55], are of further interest due to a potentially reduced trap density in  $\text{SiO}_2$  and other (yet unknown) effects. Finally, a deeper fundamental understanding of the oxidation mechanisms will enable performance improvements of emerging SiC-based devices.

## 2.8 Summary of Research Achievements

In summary, within the scope of SiC oxidation, the following research goals have been achieved:

1. A full set of dry SiC oxidation growth rate coefficients for the (0001) Si-, (11 $\bar{2}$ 0) a-, (1 $\bar{1}$ 00) m-, and (000 $\bar{1}$ ) C-face has been obtained, which enables high-accuracy simulations of SiC oxidation [72].
2. A novel 3D interpolation method to compute oxidation growth rate coefficients for arbitrary crystal direction has been developed and calibrated. The direction-dependent interpolation method captures oxidation anisotropy of SiC and thus enables the simulation of SiC oxidation for arbitrary crystal orientations and device structures [73].
3. The initial SiC oxidation stages (in the regime of ns) have been investigated in order to extend the understanding of the orientation-dependent oxidation mechanisms and to better estimate initial (i.e., native) oxide thicknesses from first principles simulations [77].

# 3 Dopant Activation

This chapter will discuss key contributions made to modeling and understanding of dopant activation mechanisms in SiC, in particular, a model to predict activation ratios as well as a semi-empirical and a transient activation model. But first, fundamentals of the dopant activation process are introduced in the following.

Semiconductor impurities can be either unintentional, due limited quality control of fabrication steps, or intentional, to provide free charge carriers and to specifically design the electrical properties of the semiconductor material. The intentional introduction of impurities into an intrinsic semiconductor is called *doping*. In order to generate free carriers in a semiconductor, it is necessary for the implanted impurities to donate electrons to the conduction band (in which case they are called donors) or to provide holes to the valence band (in which case they are called acceptors) [15].

A typical doping technique for SiC applications is ion implantation [128], which must be followed by other processing steps in order to activate the implanted dopants. The activation typically takes place during a thermal annealing step, which is typically performed at elevated temperatures (900-2200°C), in order to eliminate vacancy defects by facilitating the movement of impurity species from interstitial to substitution lattice sites, as shown in Figure 3.1. Moreover, the amorphization damage from implantation is repaired during the annealing step, consequently, the crystal structure is recrystallized [129].

Impurities are divided in two groups, namely shallow and deep impurities. The ionization of shallow impurities typically requires energy levels in the order of the thermal energy ( $k_B T$ ) or less. Deep impurities, however, require significantly more energy than the thermal energy to ionize, which means that only a fraction of the impurities present in a semiconductor will contribute free carriers. Deep impurities, which are more than five times the thermal energy ( $> 5 \cdot k_B T$ ) away from either band edge, are very unlikely to be ionized. These are called traps and can be effective recombination centers in which carriers (electrons and holes) annihilate each other [15].

Impurity doping in SiC is primarily accomplished through the introduction of N and P for n-type and Al and B for p-type doping. The properties of these dopants are shown in Table 3.1. Dopants in SiC incorporate themselves into either cubic (k) or hexagonal (h) lattice sites [130]. 4H-SiC includes an equal number of cubic and hexagonal sites which experience different surroundings and therefore enforce various activation energies.

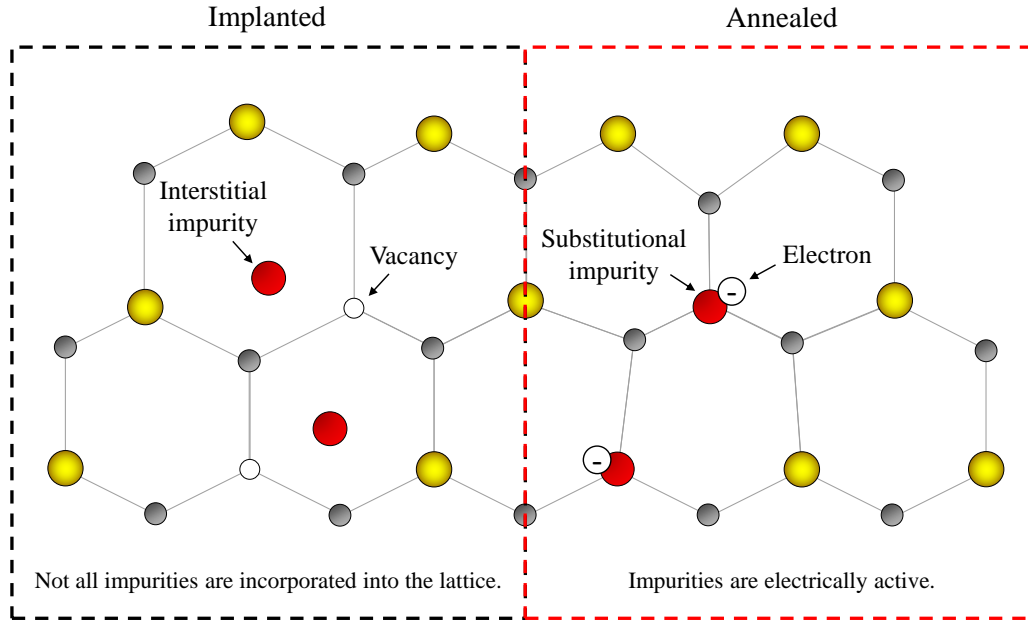


Figure 3.1: Schematic representation of the implanted and annealed impurities in SiC indicating differences in electrical activity due to the change in the crystal lattice. The yellow, gray, white, and red spheres represent Si, C, vacancies, and impurities, respectively.

Table 3.1: Chemical properties of typical SiC dopants. p and n stand for acceptor- and donor-type doping, respectively.

Element	Symbol	Group	Relative Mass	Doping Type
Aluminium	Al	3	26.98	p
Boron	B	3	10.81	p
Nitrogen	N	5	14.01	n
Phosphorus	P	5	30.97	n

## 3.1 Fundamentals of Carrier Concentration

In order to investigate electrical properties of SiC, its doping levels, and activation of implanted species, it is necessary to understand fundamental aspects of carrier concentration in semiconductors. As mentioned above, shallow impurities are ionized with energies  $\approx k_B T$ , for which it can be assumed that the ionization of impurities is always 100% [24]. This implies that the free carrier concentration approximately equals the impurity concentration. Therefore, for donors the electron concentration  $n$  equals the donor concentration  $N_D$

$$n \approx N_D \quad (3.1)$$

and for acceptors the hole concentration  $p$  equals the acceptor concentration  $N_A$

$$p \approx N_A. \quad (3.2)$$

In compensated semiconductors the carrier concentration is approximately equal to the difference between the donor and acceptor concentration [131]. For donors this yields

$$n \approx N_D - N_A, \text{ if } N_D > N_A \quad (3.3)$$

and for acceptors

$$p \approx N_A - N_D, \text{ if } N_A > N_D. \quad (3.4)$$

### 3.1.1 General Analysis of Impurities

Here a so called *general analysis* is considered, which in contrary to a regular analysis takes into account that ionization of impurities is not always 100%, as for deep impurities, but is rather given by the impurity distribution function [132]. The general analysis of incomplete impurity ionization assumes no net charge in semiconductors. This implies that the total concentration of positively charged particles (holes or ionized donors  $N_D^+$ ) must equal the total concentration of negatively charged particles (electrons or ionized acceptors  $N_A^-$ ), such that

$$n + N_A^- = p + N_D^+. \quad (3.5)$$

In order to obtain expressions for the carrier concentrations we have to integrate the density of states multiplied with the corresponding carrier distribution function over the energy space [51]. The electron concentration is thus

$$n = \int_{E_C}^{\infty} \rho_C(E) \cdot f_D \cdot dE, \quad (3.6)$$

where  $E_C$  is the bottom edge of the conduction band,  $\rho_C$  is the density of states in the conduction band, and  $f_D$  the distribution function for donors. Similarly, the hole concentration is

$$p = \int_{-\infty}^{E_V} \rho_V(E) \cdot f_A \cdot dE, \quad (3.7)$$

where  $E_V$  is the top edge of the valence band,  $\rho_V$  is the density of states in the valence band, and  $f_A$  the distribution function for acceptors.

The concentration of carriers is obtained by integrating the density of states per unit energy over all possible energies within a band. The density of states in a semiconductor is obtained by solving the Schrödinger equation for the particles in the semiconductor using the simple particle-in-a box model [24]. This model assumes that the particle is free to move within the material and that the band structure is parabolic and isotropic [51]. For an electron which behaves as a free particle with an effective mass  $m_e^*$  and Planck constant  $h$ , the density of states in the conduction band is given by [133]

$$\rho_C = \frac{8\pi\sqrt{2}}{h^3} m_e^{*3/2} \sqrt{E - E_C} \text{ for } E \geq E_C. \quad (3.8)$$

The effective mass of electrons for density of state calculations is  $m_e^* = \sqrt[3]{m_M m_K m_L}$ .  $m_M$  and  $m_K$  are the effective masses in directions perpendicular to the c-axis and  $m_L$  is the effective mass in direction along the hexagonal c-axis in the Brillouin zone. For a hole, which behaves as a free particle with the effective mass of holes  $m_h^*$ , the density of states in the valence band is given by

$$\rho_V = \frac{8\pi\sqrt{2}}{h^3} m_h^{*3/2} \sqrt{E_V - E} \text{ for } E \leq E_C, \quad (3.9)$$

The effective mass of holes for density of states calculations is  $m_h^* = \sqrt[3]{m_M m_K m_L}$ .

The thermal energy and the position of the impurity level within the bandgap affects the ionization of the impurities. Statistical thermodynamics is used to obtain the probability of the ionization of the impurities, described with the modified Fermi-Dirac distribution function [132]. A filled donor energy level contains only one electron, which can have either spin up or spin down, while having two electrons with opposite spin in one level is not allowed. A distribution function for donors is thus

$$f_D = \frac{1}{1 + g_D e^{\frac{E_F - E_D}{k_B T}}}, \quad (3.10)$$

where  $g_D$  is the spin degeneracy factor of donors,  $E_F$  the Fermi level,  $E_D$  ionization energy of donors,  $k_B$  the Boltzmann constant, and  $T$  the absolute temperature. On the other hand, the distribution function for acceptors differs due to the two-fold degenerate valence band of SiC, thus the function is given by

$$f_A = \frac{1}{1 + g_A e^{\frac{E_A - E_F}{k_B T}}}, \quad (3.11)$$

where  $g_A$  is the spin degeneracy factor of acceptors and  $E_A$  the ionization energy of acceptors.

Both of these apply in general for degenerate (i.e., heavily doped) semiconductors. However, non-degenerate semiconductors are lightly doped semiconductors, which by definition follow the approximation that the Fermi energy is at least  $3k_B T$  away from either the valence or the conduction band edge. This definition allows for a replacement of the Fermi distribution function with a simpler exponential function, i.e., the Maxwell-Boltzmann distribution function [133]. The distribution function for donors in non-degenerate semiconductors is thus

$$f_D = e^{\frac{E_F - E_D}{k_B T}} \quad (3.12)$$

and for acceptors

$$f_A = e^{\frac{E_A - E_F}{k_B T}}. \quad (3.13)$$

The electron concentration can be now analytically solved by integrating (3.6) over all possible states, i.e., from the bottom of the conduction band to infinity

$$n \cong \int_{E_C}^{\infty} \frac{8\pi\sqrt{2}}{h^3} m_e^{*3/2} \sqrt{E - E_C} e^{\frac{E_F - E}{k_B T}} dE. \quad (3.14)$$

The approximate solution of the integral for electrons is thus

$$n \cong N_C e^{\frac{E_F - E_C}{k_B T}}, \quad (3.15)$$

where  $N_C$  is the effective density of states in the conduction band [50]

$$N_C = 2M_C \left( \frac{2\pi m_e^* k_B T}{h^2} \right)^{3/2}. \quad (3.16)$$

$M_C$  is the number of equivalent minima in the conduction band. Similarly for the holes, (3.7) is written as

$$p \cong \int_{-\infty}^{E_V} \frac{8\pi\sqrt{2}}{h^3} m_h^{*3/2} \sqrt{E_V - E} e^{\frac{E - E_F}{k_B T}} dE. \quad (3.17)$$

The analytical solution of the integral for holes is thus

$$p \cong N_V e^{\frac{E_V - E_F}{k_B T}}, \quad (3.18)$$

where  $N_V$  is the effective density of states in the valence band [50]

$$N_V = 2 \left( \frac{2\pi m_h^* k_B T}{h^2} \right)^{3/2}. \quad (3.19)$$

### 3.1.2 Charge Neutrality Equation

The analysis of the non-degenerate two-type semiconductors can be further expanded with the assumption that an intrinsic carrier concentration is much smaller than the doping concentration and that the compensating acceptors (donors) are fully ionized, i.e.,  $N_A^+ = N_A$  ( $N_D^+ = N_D$ ). This assumption yields the very well known charge neutrality equation with the Boltzmann approximation [50] for n-type doping

$$n = N_D^+ - N_A^{\text{cp}} = \frac{N_D}{1 + n \frac{g_D}{N_C} e^{\frac{E_D}{k_B T}}} - N_A^{\text{cp}}, \quad (3.20)$$

where  $N_A^{\text{cp}}$  is the concentration of the compensating acceptors. Similarly, the charge neutrality equation for p-type doping is

$$p = N_A^- - N_D^{\text{cp}} = \frac{N_A}{1 + p \frac{g_A}{N_V} e^{\frac{E_A}{k_B T}}} - N_D^{\text{cp}}, \quad (3.21)$$

where  $N_D^{\text{cp}}$  is the concentration of the compensating donors.

The implicit expressions (3.20) and (3.21) can be simplified to explicit expressions via the solution of the quadratic equation. The derivative of the charge neutrality equation for the n-type doped semiconductor is thus

$$n = \frac{1}{2} \left( \frac{N_C}{g_D} e^{\frac{E_D}{k_B T}} - N_A^{\text{cp}} + \sqrt{\left( N_A^{\text{cp}} - \frac{N_C}{g_D} e^{\frac{E_D}{k_B T}} \right)^2 + 4 \frac{N_C}{g_D} e^{\frac{E_D}{k_B T}} N_D} \right) \quad (3.22)$$

and for the p-type doped semiconductor

$$p = \frac{1}{2} \left( \frac{N_V}{g_A} e^{\frac{E_A}{k_B T}} - N_D^{\text{cp}} + \sqrt{\left( N_D^{\text{cp}} - \frac{N_V}{g_A} e^{\frac{E_A}{k_B T}} \right)^2 + 4 \frac{N_V}{g_A} e^{\frac{E_A}{k_B T}} N_A} \right). \quad (3.23)$$

In order to obtain donor (acceptor) concentrations and activation energies, the charge neutrality equation is typically fitted over the electron (hole) concentrations as a function of sample temperature.

### 3.1.3 Charge Neutrality Fitting

Data for fitting must be based on identical material properties (e.g., polytypes<sup>1</sup> and orientations) of SiC and processing techniques in order to enable a meaningful investigation of the impact of annealing on the electrical activation. Furthermore, the fabrication process parameters and techniques of the data must be identical, i.e., 1) implantation temperatures, 2) annealing ambient (commonly argon (Ar)), 3) heating method (furnace or microwave), and 4) Hall measurement technique.

The charge neutrality fits are performed to obtain the donor ( $N_D$ ) or the acceptor ( $N_A$ ) concentration. It is typically assumed that the active concentration  $C_{\text{act}} = N_D$  for n-type and  $C_{\text{act}} = N_A$  for p-type doping. The fitting parameters are the ionization energy ( $E_D$  or  $E_A$ ) and the concentration of compensation ( $N_A^{\text{cp}}$  or  $N_D^{\text{co}}$ ) [135], [136]. Two donor (or acceptor) species are necessary to fit the experimental data. These species are attributed to donors (acceptors) that reside at hexagonal (h) and cubic (k) Si lattice sites. The total concentration of donors  $N_D$  (acceptors  $N_A$ ) is given by the sum of donors (acceptors) at hexagonal and cubic lattice sites.

The ionization energy ( $E_D$  or  $E_A$ ) of the implanted species is determined by the charge neutrality fitting. For P-implanted SiC the ionization energy is in average 45 meV for hexagonal and 90 meV for cubic lattice sites [137]. For N-implanted SiC the ionization energy is in average 33 meV for hexagonal and 89 meV for cubic lattice sites [138]. For Al and B-implanted SiC the total ionization energy is in the range of 191 – 230 meV and 285 – 390 meV [139]. The ionization energies are summarized in Table 3.2. The variations in ionization energies originate mostly from numerical errors due to the fitting algorithm and measurement errors due to the Hall measurement methods. The compensation concentrations are for each of the data sets different and depend on the intrinsic doping. See the provided references in Table 3.2 for a particular data set for details. The material parameters of SiC for the charge neutrality equation are described in Chapter 2, see Table 1.3.

Despite the similar electrical activation ratio of 4H- and 6H-SiC, the effective mass and the number of conduction band minima differ. The number of equivalent minima in the conduction band is 3 for 4H- [140] and 6 for 6H-SiC [141]. The effective mass is in general temperature- and polytype-dependent [30]. Thus, for charge neutrality fitting the temperature-dependent effective masses of electrons and holes for 4H- and 6H-SiC are considered, shown in Figure 3.2. The effective mass of electrons for 4H-SiC is close to constant  $0.4 e_0 - 0.5 e_0$ , while for 6H-SiC the effective mass varies from  $0.5 e_0$  up to  $0.8 e_0$ . The effective mass of holes is highly temperature-dependent for  $T < 200$  K, but for  $T > 200$  it becomes constant. In the temperature range  $T < 200$  K the effective mass of holes is higher for 6H-SiC ( $2.8 e_0$ ), compared to 4H-SiC ( $2.5 e_0$ ). Moreover, the degeneracy factors are different for certain SiC dopants. The value of the degeneracy factor is 2 for N [141] and 4 for P [140], Al [142], and B [143] dopants.

<sup>1</sup>Electrical activation between the hexagonal SiC structures, i.e., 6H- and 4H-SiC, is close to equal [134].

The data for the charge neutrality fitting is obtained from experimental results [138], [140], [141], [144] for P- and N-implanted (n-type) SiC and [143], [145], [146], [147] for Al- and B-implanted (p-type) SiC. The collection of these data sets for various annealing temperatures  $T_A$  of the n- and p-type SiC is shown in Figures 3.3 and 3.4, respectively, where the solid lines indicate the charge neutrality fits.

Table 3.2: Ionization energies of P, N, Al, and B dopants in 4H-SiC. h and k refer to the species residing at hexagonal and cubic lattice sites, respectively.

Dopant	Ionization Energy [meV]	Reference
P	43 – 48 (h)	[137], [140], [144]
	87 – 95 (k)	[137], [140], [144]
N	32 – 34 (h)	[138], [140], [144]
	80 – 92 (k)	[138], [140], [144]
Al	191 – 230 (h+k)	[139], [148]
B	285 – 390 (h+k)	[139], [143]

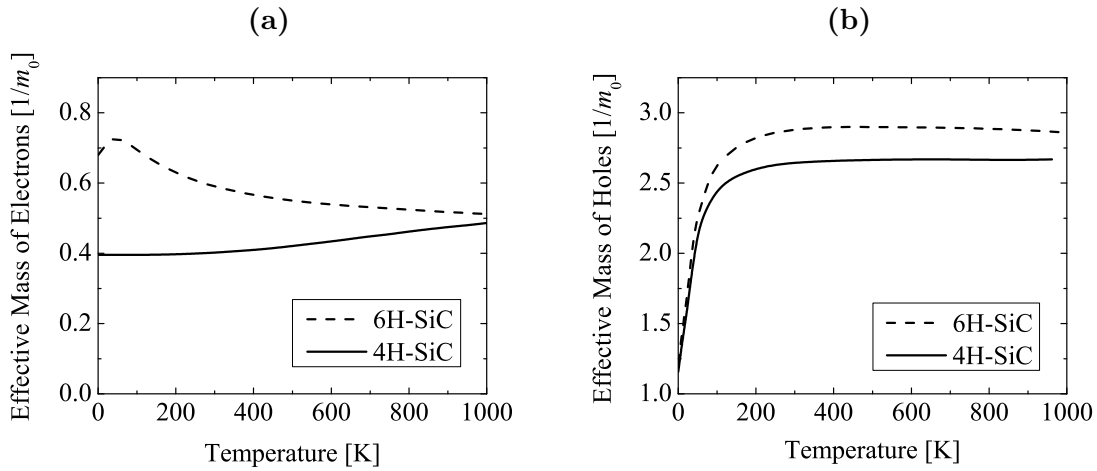


Figure 3.2: Effective mass of **(a)** electrons and **(b)** holes as a function of temperature for 6H- (dashed) and 4H-SiC (solid lines) [30]. The effective masses are stated in units of the rest mass of an electron  $m_0 = 9.11 \cdot 10^{31}$  kg.

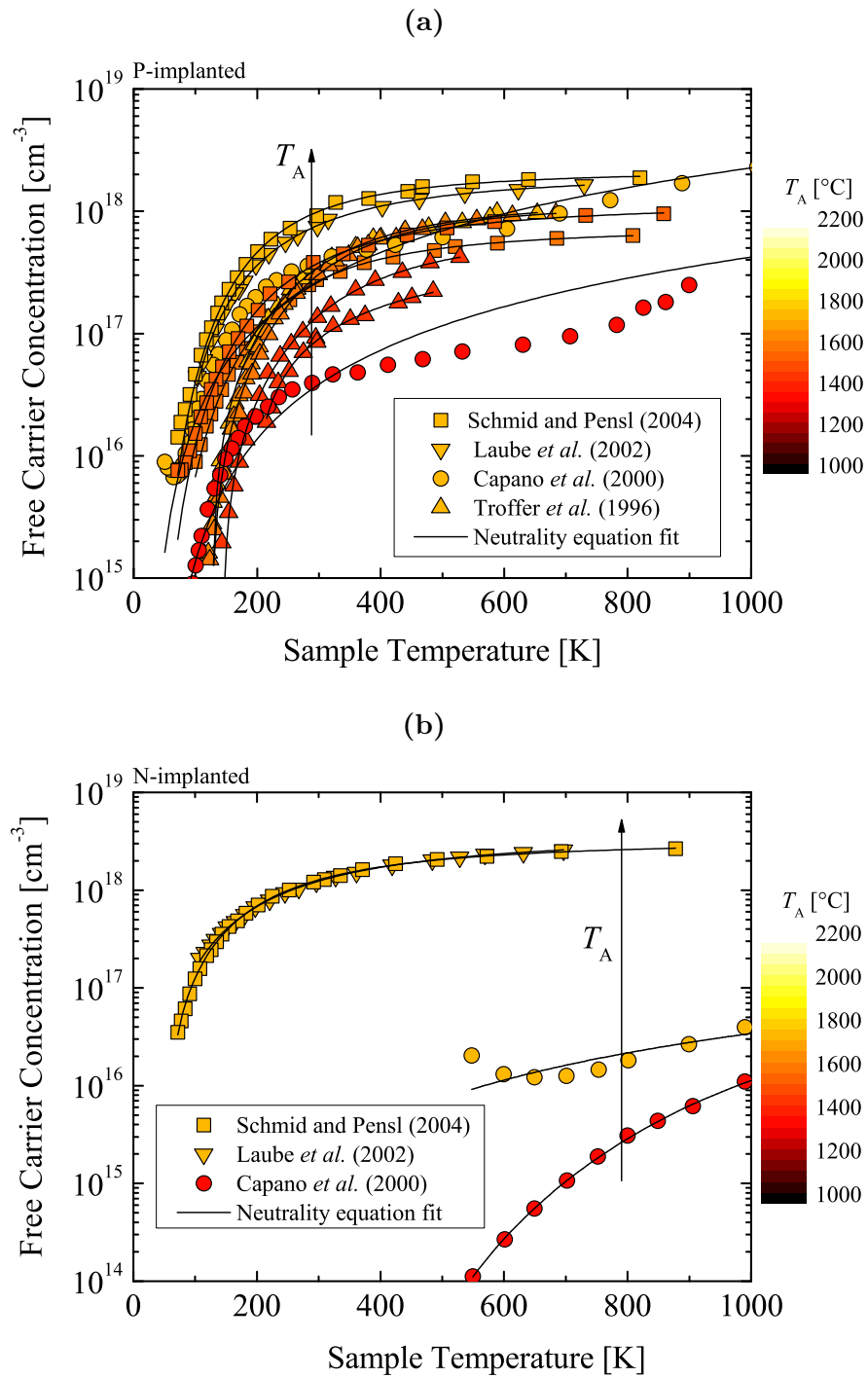


Figure 3.3: Free carrier concentration as a function of the sample temperature for (a) P- and (b) N-implanted SiC. The symbols refer to various experimental data, the solid lines are the neutrality equation fits, and the colors represent various annealing temperatures.

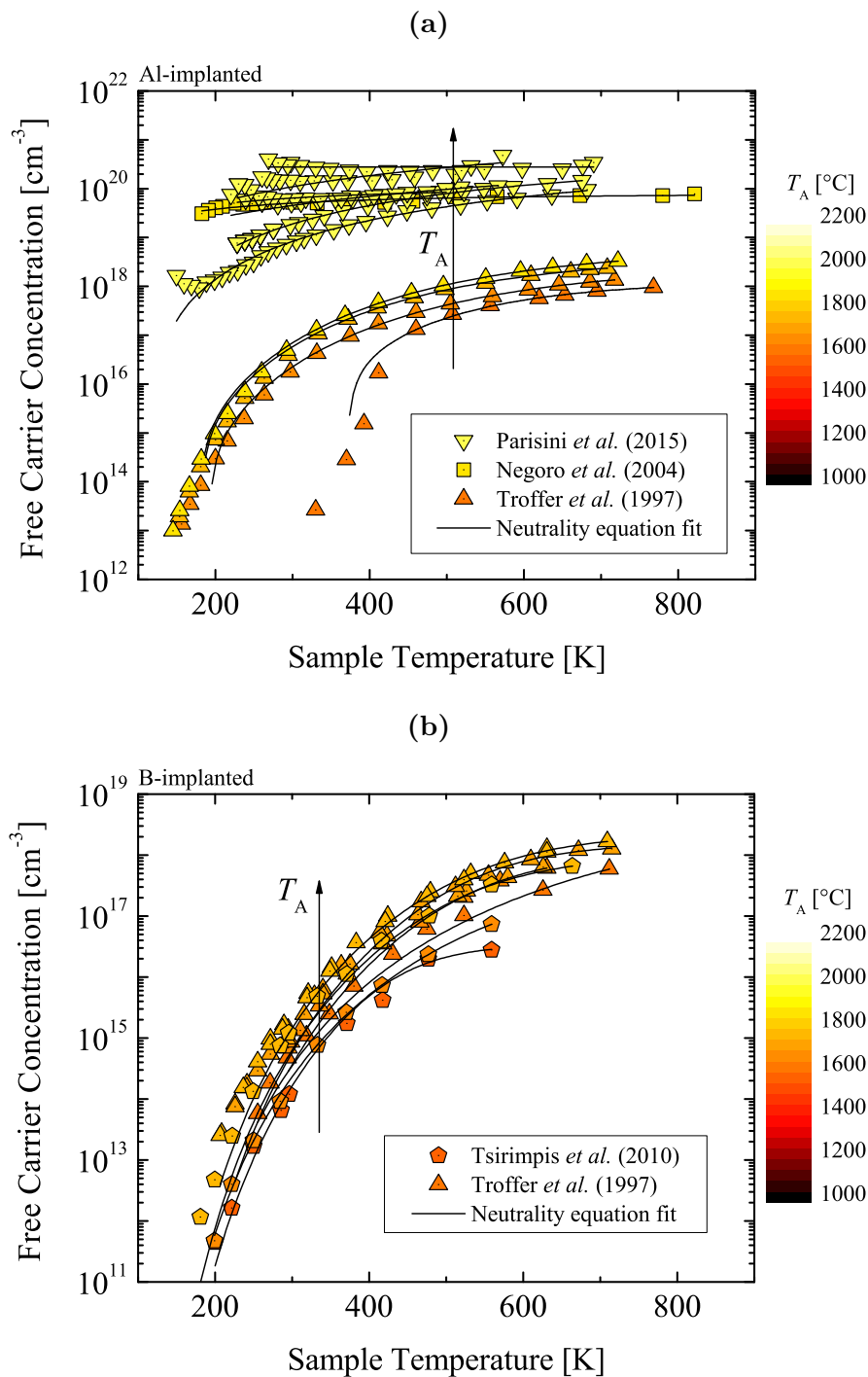


Figure 3.4: Free carrier concentration as a function of the sample temperature for (a) Al- and (b) B-implanted SiC. The symbols refer to various experimental data, the solid lines are the neutrality equation fits, and the colors represent various annealing temperatures.

## 3.2 Activation Ratio Model

In order to simplify the understanding and characteristics of the doping in semiconductors, the ratio of electrical activation of impurities has been introduced and is presented in the following [135], [149]. The activation ratio of an n-type doped semiconductor is defined as the donor concentration  $N_D$  over the total concentration of the n-type doping  $C_{\text{tot}}^n$

$$R_{\text{act}}^n = \frac{N_D}{C_{\text{tot}}^n}. \quad (3.24)$$

Likewise, the activation ratio of a p-type doped semiconductor is defined as the acceptor concentration  $N_A$  over the total concentration of the p-type doping  $C_{\text{tot}}^p$

$$R_{\text{act}}^p = \frac{N_A}{C_{\text{tot}}^p}. \quad (3.25)$$

The donor and acceptor concentrations from (3.24) and (3.25) are commonly obtained via least squares fitting [150] of the charge neutrality equation to the data of the free carrier concentration as a function of the sample temperature. The carrier concentrations are in general increased with increased annealing time, annealing temperature, total doping concentration, implantation temperature, and other processing variables. The annealing temperature has by far the highest influence on the activation ratio of impurities in SiC.

### 3.2.1 Methodology

The activation ratio model describes the relationship between the electrical activation ratio and the annealing temperatures. Based on this theoretical approach it is now possible to predict the activation ratios for an arbitrary annealing temperature of P-, N-, Al-, or B-implanted SiC. The model avoids computationally expensive numerical calculations, thereby significantly improving the overall simulation speed, whilst simultaneously providing a highly accurate approximation. The proposed model is an important step to further enhance the process simulation capabilities for SiC technologies.

The major assumption of the activation ratio model is that the time of the annealing processes is a minimum of 30 minutes, which assures that the doped material reaches the full activation state for the corresponding annealing temperature [135]. The activation ratio model characterizes the electrical activation ratio  $R_{\text{act}}$  (i.e.,  $R_{\text{act}}^n$  and  $R_{\text{act}}^p$  for n- and p-type SiC, respectively) as a function of the annealing temperature  $T_A$ . The model [136] is formulated as

$$R_{\text{act}} = R_{\frac{1}{2}} + \left( R_{\text{max}} - R_{\frac{1}{2}} \right) \tanh \left( k_{\text{slope}} (T_A - T_{\text{ip}}) \right), \quad (3.26)$$

with

$$R_{\frac{1}{2}} = \left( \frac{R_{\min} + R_{\max}}{2} \right). \quad (3.27)$$

$k$ ,  $R_{\min}$ ,  $R_{\max}$ , and  $T_{\text{ip}}$  are the model parameters.  $R_{\frac{1}{2}}$ ,  $R_{\max}$ , and  $R_{\min}$  are the half-maximal, maximal, and minimal electrical activation ratio, respectively,  $k_{\text{slope}}$  is the slope of the step, and  $T_{\text{ip}}$  the temperature at the inflection of the curve, as shown in Figure 3.5.

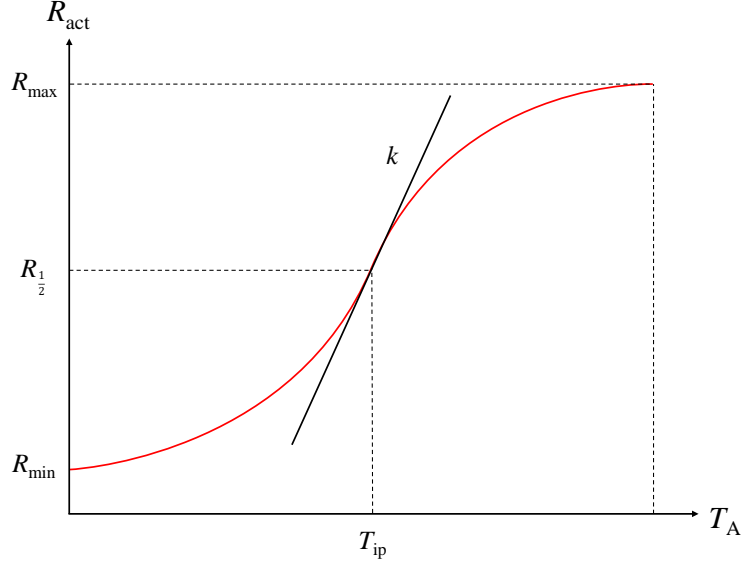


Figure 3.5: Schematic representation of parameters of the activation ratio model and its characteristics of the curve. The red line indicates the model and the black line the slope of the curve at the inflection point, i.e.,  $(T_{\text{ip}}, R_{\frac{1}{2}})$ .

### 3.2.2 Calibration

For the corresponding annealing temperature the donor and acceptor concentrations (obtained via charge neutrality fitting) are incorporated into the ratios of electrical activation via (3.24) and (3.25), respectively. The activation ratios as a function of the annealing temperature for n- and p-type SiC are shown in Figures 3.6 and 3.7. The acceptor and donor concentrations obtained via the charge neutrality fitting are in good agreement with experimental data [1], [130], [151], [152], [153] and provide additional insights into the activation mechanism. The activation ratios are highly temperature-dependent and can be characterized with the activation ratio model accurately predicting the temperature-related effects of the annealing steps. The parameters of the activation ratio model fitting from Figures 3.6 and 3.7 are summarized in Table 3.3.

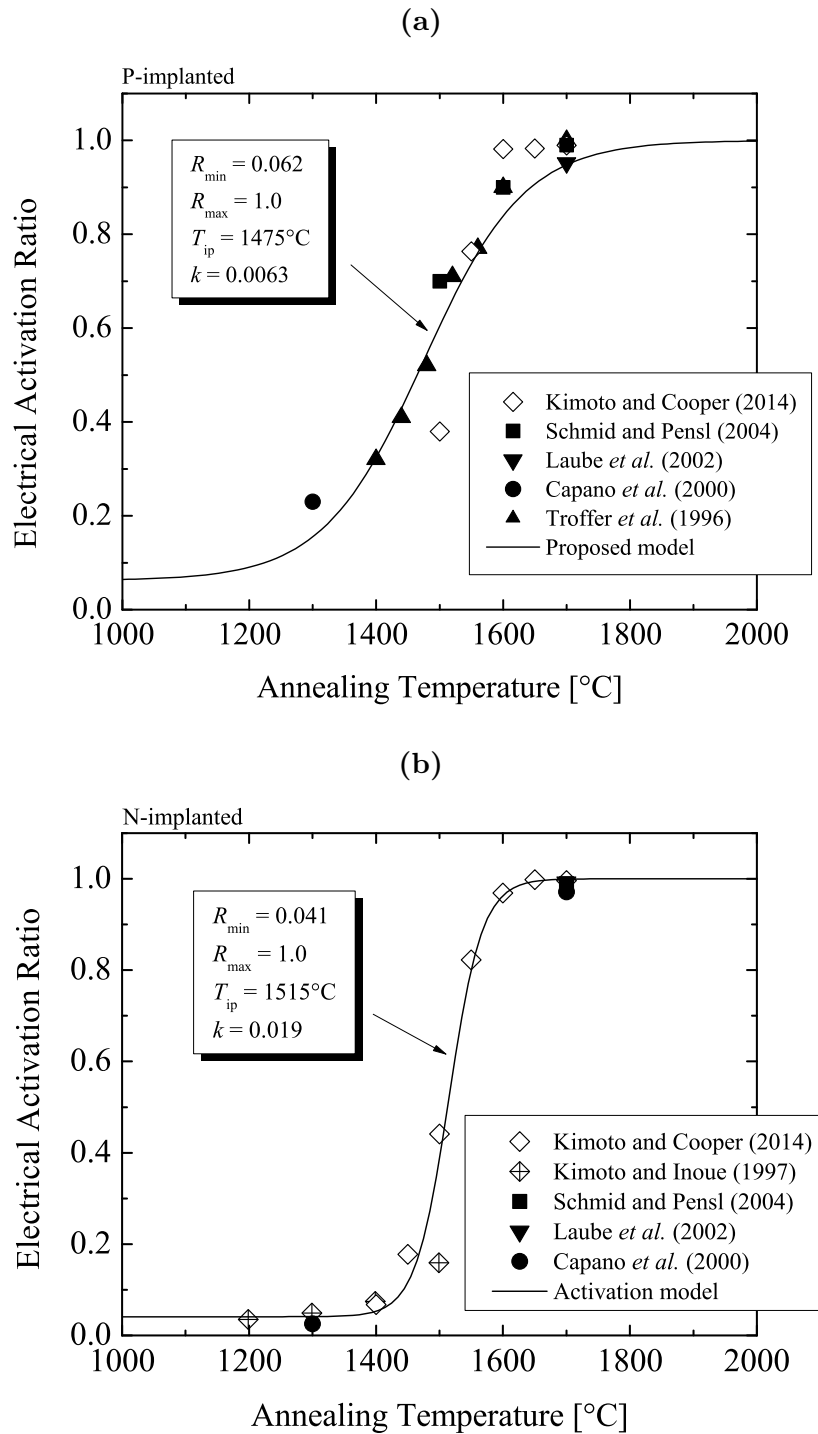


Figure 3.6: Electrical activation ratios of (a) P and (b) N donors as a function of the annealing temperature. The open symbols refer to experimental data sets, the closed symbols are results from fitting, and the solid lines are computed with the activation ratio model.

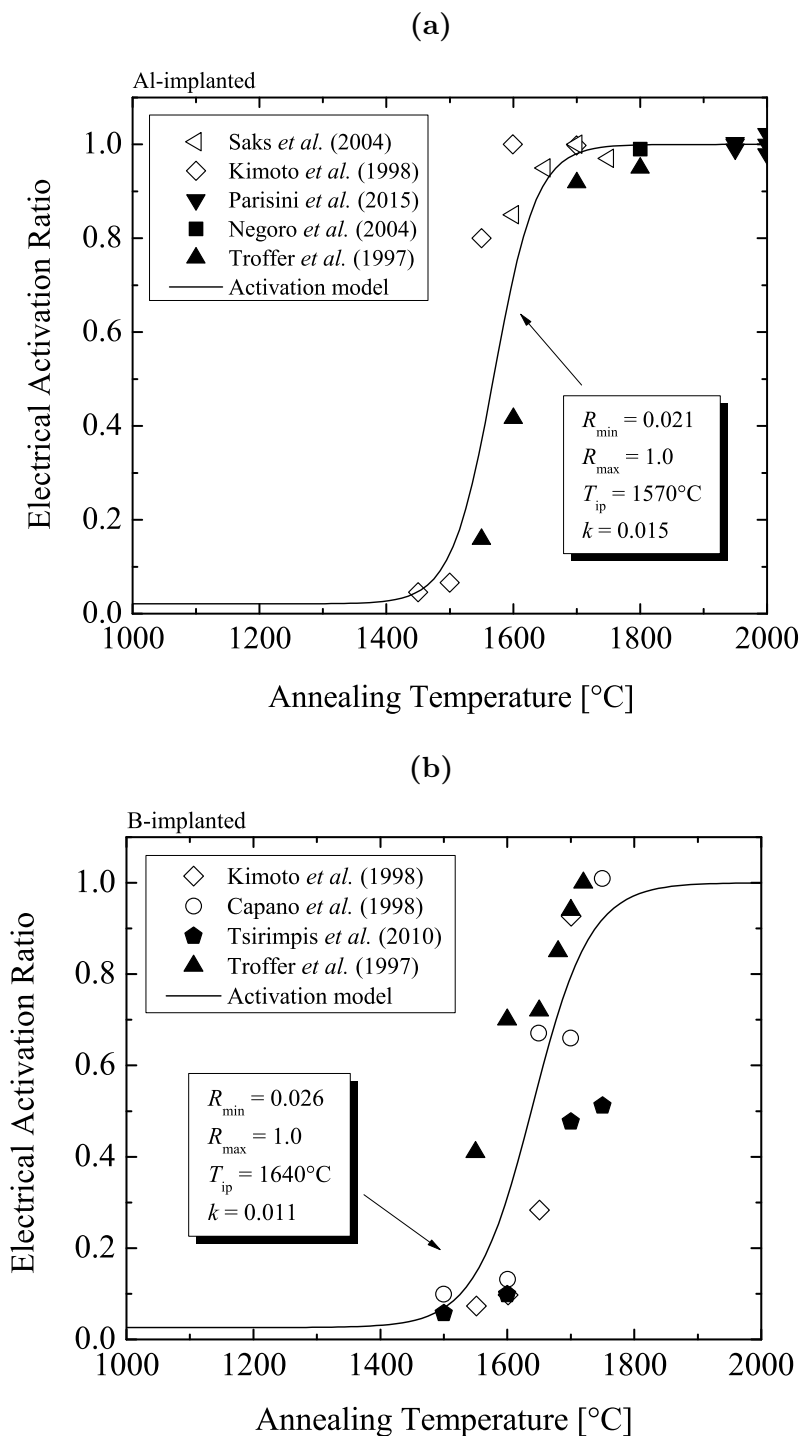


Figure 3.7: Electrical activation ratios of (a) Al and (b) B acceptors as a function of the annealing temperature. The open symbols refer to experimental data sets, the closed symbols are results from fitting, and the solid lines are computed with the activation ratio model.

Table 3.3: Model parameters for P-, N-, Al-, and B-implanted SiC.

Dopant	$R_{\min}$ [/]	$R_{\max}$ [/]	$T_{\text{ip}}$ [°C]	$k$ [1/°C]
P	0.062	1.0	1475	0.0063
N	0.041	1.0	1515	0.019
Al	0.021	1.0	1570	0.015
B	0.026	1.0	1640	0.011

The activation ratio model suggest that the P and N species reach full activation at high temperatures  $T_A > 1700^\circ\text{C}$  and that the minimal activation of both donor-type dopants is approximately 5%. Additionally, the model shows that the ratio of the N-implanted SiC is similar to a step function, while the ratio for the P-implanted SiC increases continuously with temperature, i.e.,  $k(N) \approx 3k(P)$ . A high activation (above 95 %) is achieved for  $T_A > 1800^\circ\text{C}$  for Al and  $T_A > 1700^\circ\text{C}$  for B impurities and a very low activation (below 10 %) is detected for  $T_A > 1500^\circ\text{C}$  for both Al and B implantations. These findings imply that the thermal activation mechanism dominates within the temperature range  $1500^\circ\text{C} < T_A < 1800^\circ\text{C}$  and must be therefore appropriately characterized, i.e., calculated with the introduced model.

The activation ratio model includes only a dependence on the annealing temperature. For a majority of semiconductor materials the total doping concentration has, in addition to the annealing temperature, a considerable effect on the electrical activation of impurities. For this reason a semi-empirical model is introduced in order to further increase the accuracy of process simulations.

### 3.3 Semi-Empirical Model

In the previous section a temperature-dependent activation model has been demonstrated in detail. However, the post-implantation annealing steps of process simulations are much more complex, i.e., include many more dependences. Besides the annealing temperature the next most significant dependence is on the total doping concentration [1]. Both process variables ( $T_A$  and  $C_{\text{tot}}$ ) are essential in order to maximize the efficiency of SiC devices and must be accurately predicted by TCAD process simulations. For this reason, the semi-empirical activation model has been proposed, evaluated, and tested [154] and is presented in the following.

### 3.3.1 Methodology

The semi-empirical model has been inherited and modified from the model for the electrical activation of dopants in silicon [53]. The modification for SiC introduces a continuous transition between the linear and the logarithmic component of the model, which enables model fitting on the entire scale of the investigated variables. The semi-empirical model is represented by an empirical time-independent formula and assumes that the activation of dopants happens instantaneously, i.e., in a fraction of time. The donor  $N_D$  or acceptor concentration  $N_A$  is represented as the active dopant concentration  $C_{\text{tot}}$  and is described as [154]

$$C_{\text{act}} = S_1 C_{\text{tot}} + S_2 C_{\text{th}} S_t, \text{ where} \quad (3.28)$$

$$\begin{aligned} S_1 &= 1/2 (1 + \tanh(C_{\text{th}} - C_{\text{tot}})), \\ S_2 &= 1/2 (1 + \tanh(C_{\text{tot}} - C_{\text{th}})), \text{ and} \end{aligned} \quad (3.29)$$

$$S_t = \left( 1 + (1 - F_{\text{act}}) \ln \left( \frac{|C_{\text{tot}}/C_{\text{th}} - F_{\text{act}}|}{1 - F_{\text{act}}} \right) \right). \quad (3.30)$$

$C_{\text{tot}}$  is the total concentration of (e.g., implanted) dopants,  $C_{\text{th}}$  is the dopant specific threshold concentration,  $F_{\text{act}}$  is the empirical scalar parameter,  $S_t$  is the saturation ratio, and  $S_1$  and  $S_2$  are model pre-factors.

For the total dopant concentration below the threshold concentration ( $C_{\text{tot}} < C_{\text{th}}$ ) the model suggests that after annealing at a given temperature the acceptor concentration equals the total doping concentration ( $N_A = C_{\text{tot}}$ ). Note,  $C_{\text{th}}$  varies with annealing temperature, therefore, the regime of full dopant activation is indirectly temperature-dependent. For the total dopant concentration above the threshold concentration ( $C_{\text{tot}} > C_{\text{th}}$ ) the model introduces dopant and temperature-dependent saturation effects, described by (3.30). Thus, a continuous switching between the linear and the logarithmic region of the activation response is required, which is handled via pre-factors (3.29) according to the difference between  $C_{\text{tot}}$  and  $N_A$ . This is a key contribution of the SiC modeling approach and enables model fitting and calibration of simulation tools.

Despite the complexity of the model expression, an advantage of the model is the low number of free model parameters and its analytic nature: The computational complexity is thus significantly smaller than a first principles simulation, e.g., a molecular dynamics simulation. In an industry-focused simulation context the empirical approach is thus preferred.

### 3.3.2 Calibration

In order to calibrate the semi-empirical model a sufficient amount of sets of annealing data must be collected for various implanted concentrations and annealing temperatures [136]. These are obtained via charge neutrality fitting of the measurements [137], [138], [140], [141], [144] for P- and N-implanted (n-type) SiC and [130], [134], [143], [144], [147], [152], [155] for Al- and B-implanted (p-type) SiC. The acceptor concentrations as a function of the total implanted concentrations for various annealing temperatures are shown in Figures 3.8 and 3.9 for n- and p-type SiC, respectively.

Doping concentrations from  $10^{16} \text{ cm}^{-3}$  to  $10^{21} \text{ cm}^{-3}$  and annealing temperatures from  $1300^\circ\text{C}$  to  $1900^\circ\text{C}$  have been investigated. Only the data which is based on identical crystal orientations, annealing ambient, implantation temperatures, and measurement methods is considered. As already discussed, this data selection is necessary to ensure a meaningful and correct investigation of the annealing temperature and total concentration-dependent effects on the activation of impurities. The annealing steps of the collected data include microwave heating in an Ar ambient. The collection of these data sets assumes no differences in activation ratios between hexagonal structures of SiC, i.e., 4H- and 6H-SiC. The error due to this assumption is in average very small, i.e.,  $< 5\%$  [134] and can thus be neglected. In addition, the fitted data must only include the activation state of impurities at the thermodynamic equilibrium, which is a fundamental requirement of the model. Overall, these important criteria limit the amount of relevant data, but in turn ensure a proper frame of reference for the semi-empirical model.

An iterative fitting method, evaluated by least squares error, is used to accurately fit the model (3.28–3.30) to the pre-processed data of the acceptor concentrations as a function of the total doping concentration. In order to minimize the numerical fitting error due to the low amount of relevant data, 100% activation is assumed for samples with low implanted concentration, which are annealed at high temperatures relative to the implanted dose. The model parameter  $C_{\text{th}}$  for P-, N-, Al-, and B-implanted SiC is obtained with respect to the various annealing temperatures. It has been empirically determined that the best fits are accomplished for  $F_{\text{act}} \approx 0.9$ . Therefore, the empirical scalar parameter is, particularly for SiC, fixed to 0.9 for all cases.

The temperature-dependent parameter  $C_{\text{th}}$  introduces the dopant concentration limit where saturation effects start to manifest. The activation ratio is significantly reduced (i.e., saturates) above the threshold for a particular annealing temperature. The threshold concentrations for the p- and n-type implantation, obtained by model fitting, is shown in Figures 3.10 and 3.11, respectively.

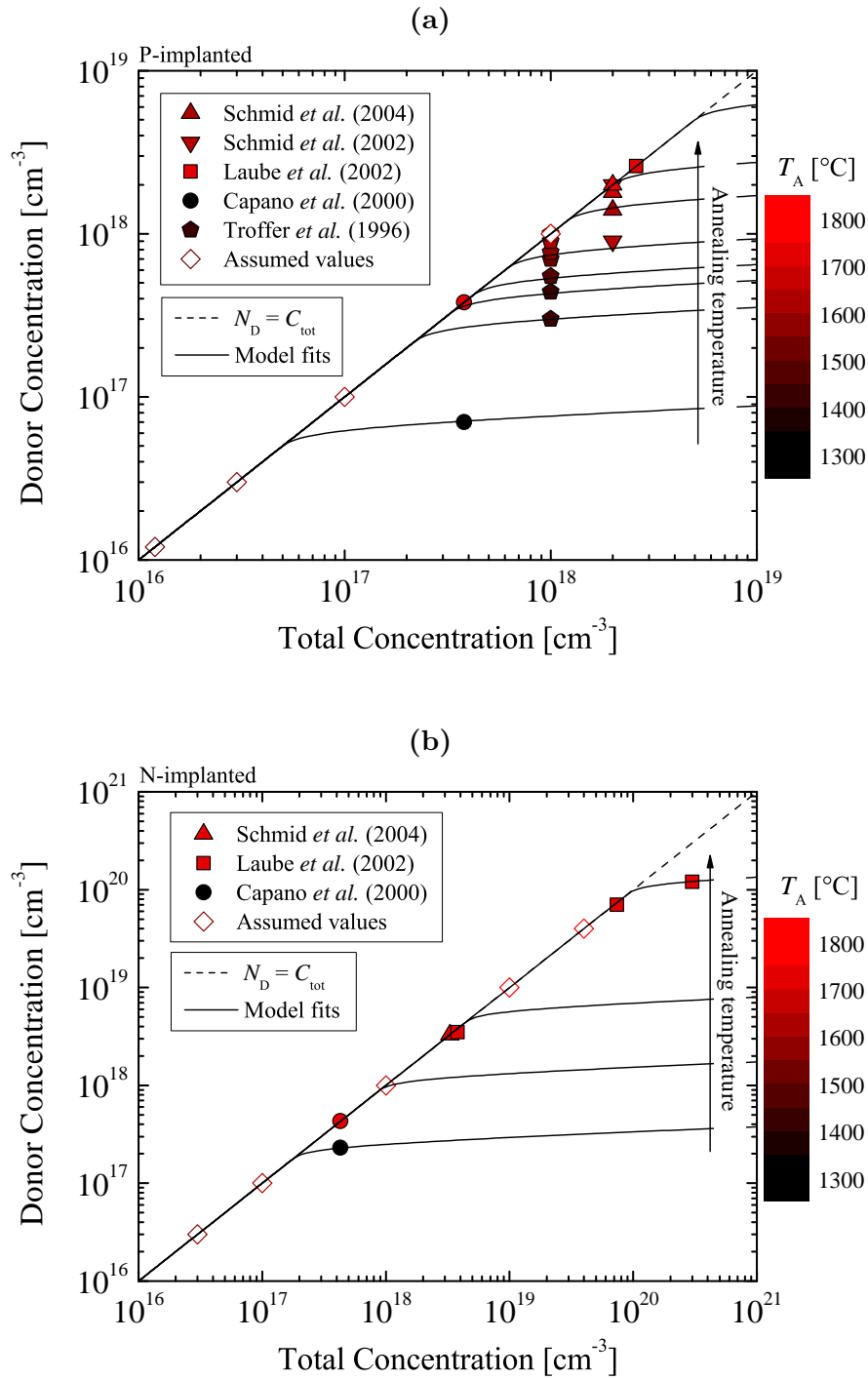


Figure 3.8: Acceptor concentrations as a function of the total doping concentration for (a) P- and (b) N-implanted SiC. The closed symbols refer to the references [137], [138], [140], [141], [144] and the open symbols refer to the assumed values, which are used to increase the accuracy of the model fitting. The solid lines are model fits and the dashed lines indicate the linear dependence of  $N_D$ . The colors refer to the various annealing temperatures.

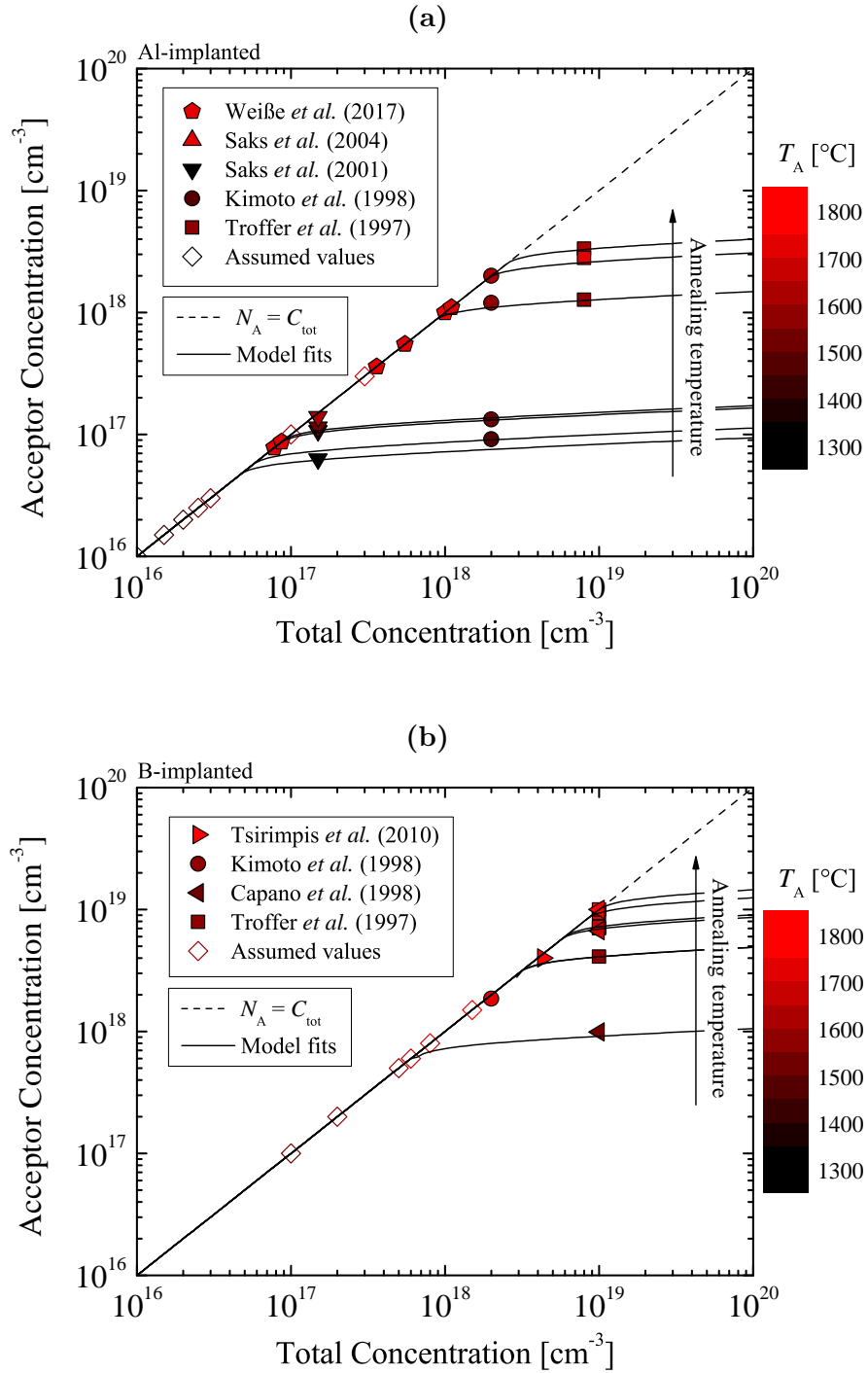


Figure 3.9: Acceptor concentrations as a function of the total doping concentration for (a) Al- and (b) B-implanted SiC. The closed symbols refer to the references [130], [134], [143], [144], [147], [152], [155] and the open symbols refer to the assumed values, which are used to increase the accuracy of the model fitting. The solid lines are model fits and the dashed lines indicate the linear dependence of  $N_A$ . The colors refer to the various annealing temperatures.

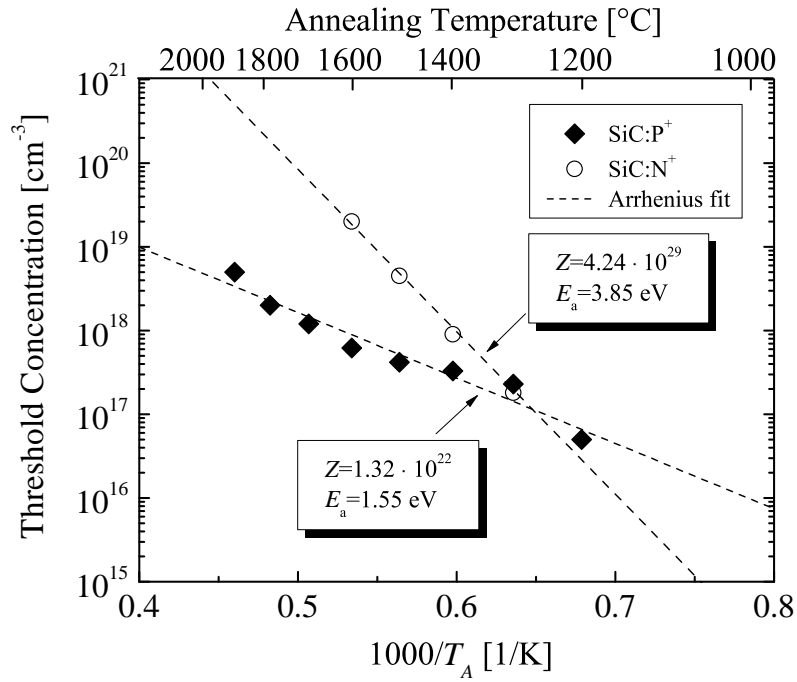


Figure 3.10: Threshold concentration as a function of the annealing temperature for P- and N-implanted SiC. The symbols refer to results obtained by the semi-empirical model and the dashed lines are Arrhenius fits.

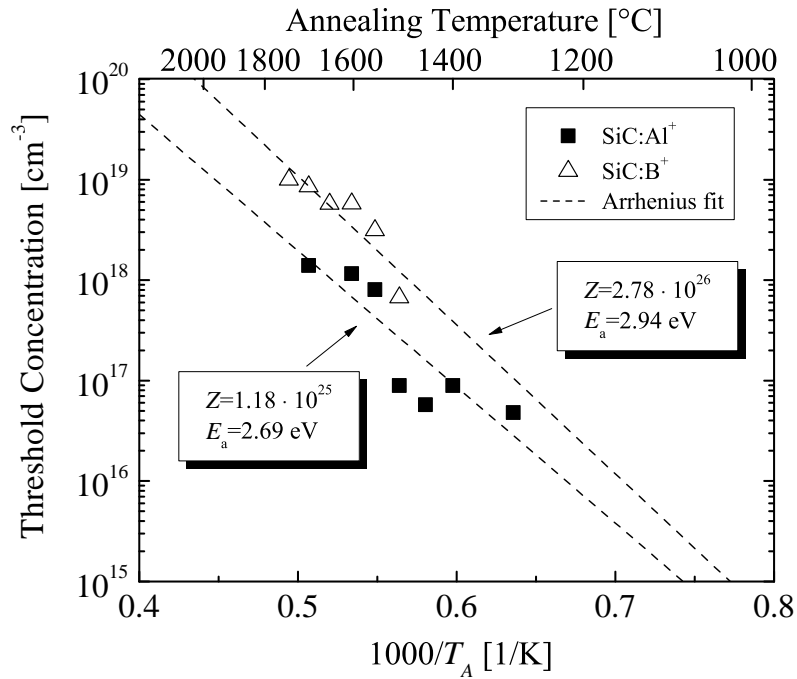


Figure 3.11: Threshold concentration as a function of the annealing temperature for Al- and B-implanted SiC. The symbols refer to results obtained by the semi-empirical model and the dashed lines are Arrhenius fits.

An Arrhenius function is used in order to introduce a continuous temperature dependence of the model parameter. The best fit is achieved with an activation energy  $E_a = 1.55$  eV and a pre-exponential factor  $Z = 1.32 \cdot 10^{22}$  cm<sup>-3</sup> for P,  $E_a = 3.85$  eV and  $Z = 4.24 \cdot 10^{29}$  cm<sup>-3</sup> for N,  $E_a = 2.69$  eV and  $Z = 1.18 \cdot 10^{25}$  cm<sup>-3</sup> for Al, and  $E_a = 2.94$  eV and  $Z = 2.78 \cdot 10^{26}$  cm<sup>-3</sup> for B dopants. The Arrhenius parameters of the threshold concentrations for each of the SiC dopants are summarized in Table 3.4.

N donors have by far the highest activation energies of  $C_{th}$ , followed by B and Al acceptors, and finally P donors. Comparing the two donor-type dopants,  $C_{th}$  of N is higher above and lower below 1290°C. This indicates that N dopants achieve 100% activation for higher total concentrations than P dopants at high annealing temperatures. Comparing the two acceptor-type dopants, the threshold of B-implanted SiC becomes significantly larger at high annealing temperatures than the threshold of Al-implanted SiC. This effect is associated with the atomic mass of the dopants, i.e., B ions are lighter than Al ions [143], see Table 3.1.

Table 3.4: Arrhenius parameters of threshold concentration ( $C_{th}$ ) for P-, N-, Al-, and B-implanted SiC.

Dopant	$Z$ [cm <sup>-3</sup> ]	$E_a$ [eV]
P	$1.32 \cdot 10^{22}$	1.55
N	$4.24 \cdot 10^{29}$	3.85
Al	$1.18 \cdot 10^{25}$	2.69
B	$2.78 \cdot 10^{26}$	2.94

### 3.3.3 Characterization

In order to characterize the model's predictive character and analyze results thoroughly, parameter studies were performed, which are based on  $> 10^6$  individual simulations to cover a wide range of parameter variations. Each of the simulations must satisfy thermal equilibrium criteria. In the case of the semi-empirical model, the activation is assumed to be instant, therefore, the resulting values correspond to the values in the thermal equilibrium.

The results are collected in phase diagrams, which show the conditions, such as temperature and concentration, at which thermodynamically distinct phases occur and coexist at thermal equilibrium: Results of ion implantation followed by various thermal annealing steps for P- and N-implanted SiC are shown in Figure 3.12 and for Al- and B-implanted SiC in Figure 3.13. The phase diagrams suggest activation regions of the dopants for various doping concentrations and annealing temperatures.

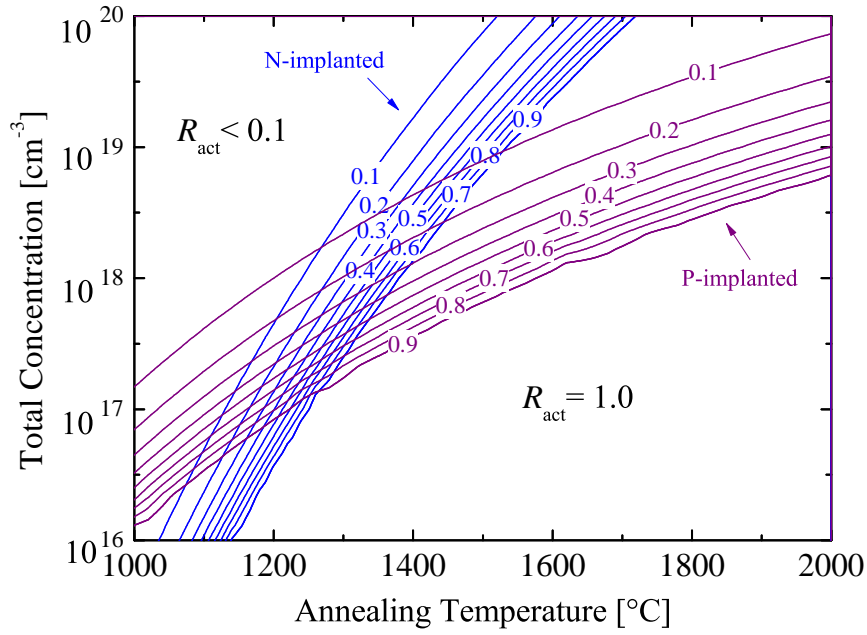


Figure 3.12: Phase diagrams of electrical activation as a function of the total concentration and annealing temperature for P- and N-implanted SiC. The contour lines refer to the electrical activation ratio  $R_{\text{act}}$ .

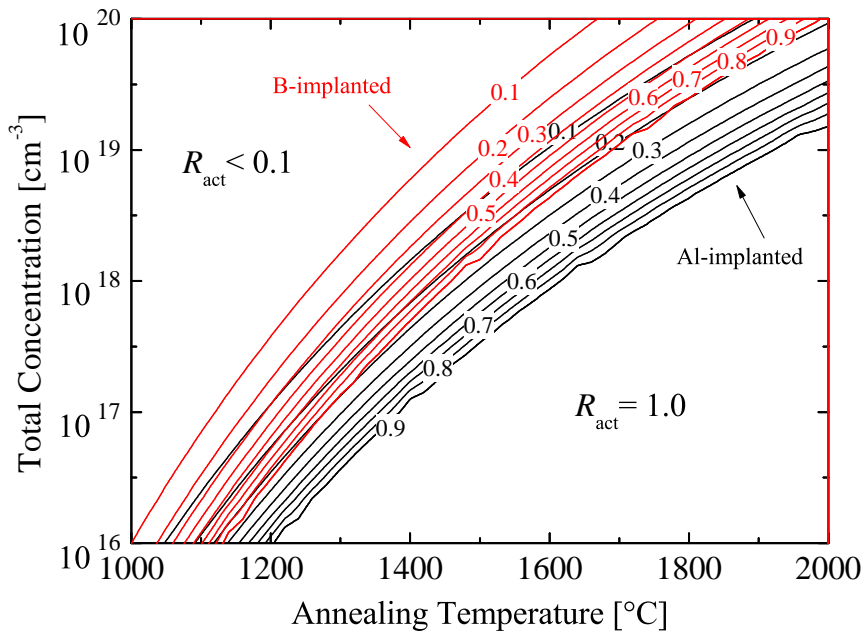


Figure 3.13: Phase diagrams of electrical activation as a function of the total concentration and annealing temperature for Al- and B-implanted SiC. The contour lines refer to the electrical activation ratio  $R_{\text{act}}$ .

The predicted phase diagrams are crucial to correctly predict parameters for SiC device processing, where the balance between the efficiency of electrical properties and the costs for post-implantation annealing must be carefully considered to optimize fabrication steps. When comparing donor-type dopants it is clear that P implants in general require higher annealing temperatures for successful anneals (i.e., activation above 90%), compared to N implants. For the low-dose implantations, below  $10^{17} \text{ cm}^{-3}$ , both of the implants are activated even for  $T_A < 1200^\circ\text{C}$ . However, for high-dose implantation ( $C_{\text{tot}} = 1.0 \cdot 10^{20} \text{ cm}^{-3}$ ), P implants are poorly activated (i.e.,  $R_{\text{act}} < 0.1$ ) even at  $T_A \approx 2000^\circ\text{C}$ , while on the other hand, N implants for the same  $C_{\text{tot}}$  are fully activated at  $T_A = 1750^\circ\text{C}$ . Comparing acceptor-type dopants at low-dose implantation, the full activation state ( $R_{\text{act}} = 1$ ) is achieved at  $T_A = 1070^\circ\text{C}$  for Al-implanted and  $T_A = 1010^\circ\text{C}$  for B-implanted SiC. In contrast, for high-dose implantation the full activation in thermal equilibrium is achieved at  $T_A = 1940^\circ\text{C}$  for Al and  $T_A = 1695^\circ\text{C}$  for B-implanted SiC. This suggests that for low  $C_{\text{tot}}$  lower temperatures are sufficient for full activation of Al, compared to B. However, for high  $C_{\text{tot}}$  this effect reverses. In addition, for  $C_{\text{tot}} = 10^{20} \text{ cm}^{-3}$  the full activation of Al acceptors is not achieved for the investigated annealing temperatures, but in contrast, B acceptors with the identical implantation dose reached full activation at  $T_A = 2010^\circ\text{C}$ .

### 3.3.4 Simulations

The semi-empirical activation model has been integrated into Silvaco's Victory Process simulator [53], which now includes calibrated model parameters as discussed in Section 3.3.2. In this section, in order to verify predictions of the semi-empirical model, the results of process simulations are compared to experimental findings. As will be discussed, process simulations include all the steps of typical device fabrication processes, such as implantation, oxidation, and annealing. For the verification of the model numerous simulations of the same device are performed, but with different values of a single parameter involved in a particular simulation step. More concretely, numerous SiC diodes are processed with various annealing temperatures to examine and clarify the effects of the temperature involved in the annealing step.

This section focuses on Al- and B-implanted SiC due to the availability of experimental data with respect to various annealing temperatures. The doping as well as the annealing steps follow the experimental setups of Saks *et al.* [134] and Troffer *et al.* [147] in order to enable an elaborate comparison. The implantation steps have been performed with Silvaco's Victory Process simulator using Monte Carlo ion implantation on (0001) Si-oriented 4H-SiC. The annealing steps have been performed with the semi-empirical model and parameters, alongside the Fermi diffusion model. An example of the simulated device is shown in Figure 3.14. The simplicity of the simulated devices is vital in order to ensure a proper, focused investigation of the process annealing steps, including the total doping concentration and the annealing temperature.

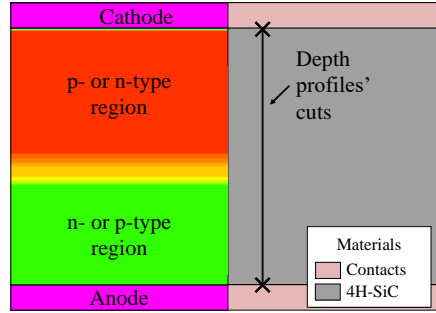


Figure 3.14: Schematic representation of the doping profile and geometry of the processed device in Silvaco's Victory Process simulator. The colors (left) refer to different doping regions, the gray region (right) is SiC substrate, and the light rose regions (right) are ohmic contacts, i.e., anode and cathode.

The semi-empirical activation model is evaluated by comparisons between simulations and experiments, shown in Figure 3.15. The first simulation setup (Figure 3.15a) follows the experimental setup of Saks *et al.* [134], which consists of an N-doped, n-type SiC wafer with a compensation concentration of  $\approx 5 \cdot 10^{15} \text{ cm}^{-3}$ , followed by several Al-implantations generating a rectangular profile with a mean concentration of  $\approx 10^{17} \text{ cm}^{-3}$ . The annealing steps are 12 h at  $T_A = 1300^\circ\text{C}$ , 1 h at  $T_A = 1400^\circ\text{C}$ , and 10 min at  $T_A = 1500^\circ\text{C}$ . The time of the thermal treatment influences the diffusion, but does not enter the proposed activation model. The second simulation setup (Figure 3.15b) follows the experimental setup of Troffer *et al.* [147], which consists of a N-doped, n-type SiC wafer with a compensation concentration of  $\approx 1.5 \cdot 10^{16} \text{ cm}^{-3}$ , followed by several B-implantations generating a rectangular profile with a mean concentration of  $\approx 10^{19} \text{ cm}^{-3}$ . The annealing steps are 30 min at  $T_A = 1500^\circ\text{C}$ , 30 min at  $T_A = 1600^\circ\text{C}$ , and 30 min at  $T_A = 1700^\circ\text{C}$ .

The depth profiles of both p-type dopants are reproduced with an average variation  $\sigma < 3\%$  for all of the implantation and annealing steps. This confirms that the semi-empirical model predicts acceptor concentrations very accurately in the temperature range of  $T_A > 1200^\circ\text{C}$  and  $T_A < 1800^\circ\text{C}$  and total implanted concentration range of  $C_{\text{tot}} > 10^{16} \text{ cm}^{-3}$  and  $C_{\text{tot}} < 10^{20} \text{ cm}^{-3}$ . Outside of these limitations the model extrapolates predictions according to Arrhenius fits.

In addition to the verification by comparison with experimental data, various simulations to predict a minimal required temperature for the full activation of the implants are performed. In the first case of  $1.0 \cdot 10^{17} \text{ cm}^{-3}$  Al-implanted SiC, an activation ratio  $R_{\text{act}} = 1$  is achieved for the thermal treatments above  $T_A = 1700^\circ\text{C}$ . In the case of  $1.0 \cdot 10^{19} \text{ cm}^{-3}$  B-implanted SiC,  $R_{\text{act}} = 1$  is achieved for the annealing steps above  $T_A = 1750^\circ\text{C}$ . The annealing steps of B-implanted SiC additionally show a high diffusion of B ions over the entire implanted region. However, the diffusion of Al ions is negligible and evident only at the surface, i.e., depth  $< 0.05 \mu\text{m}$ . These findings are consistent with the conclusions of Saks *et al.* [134].

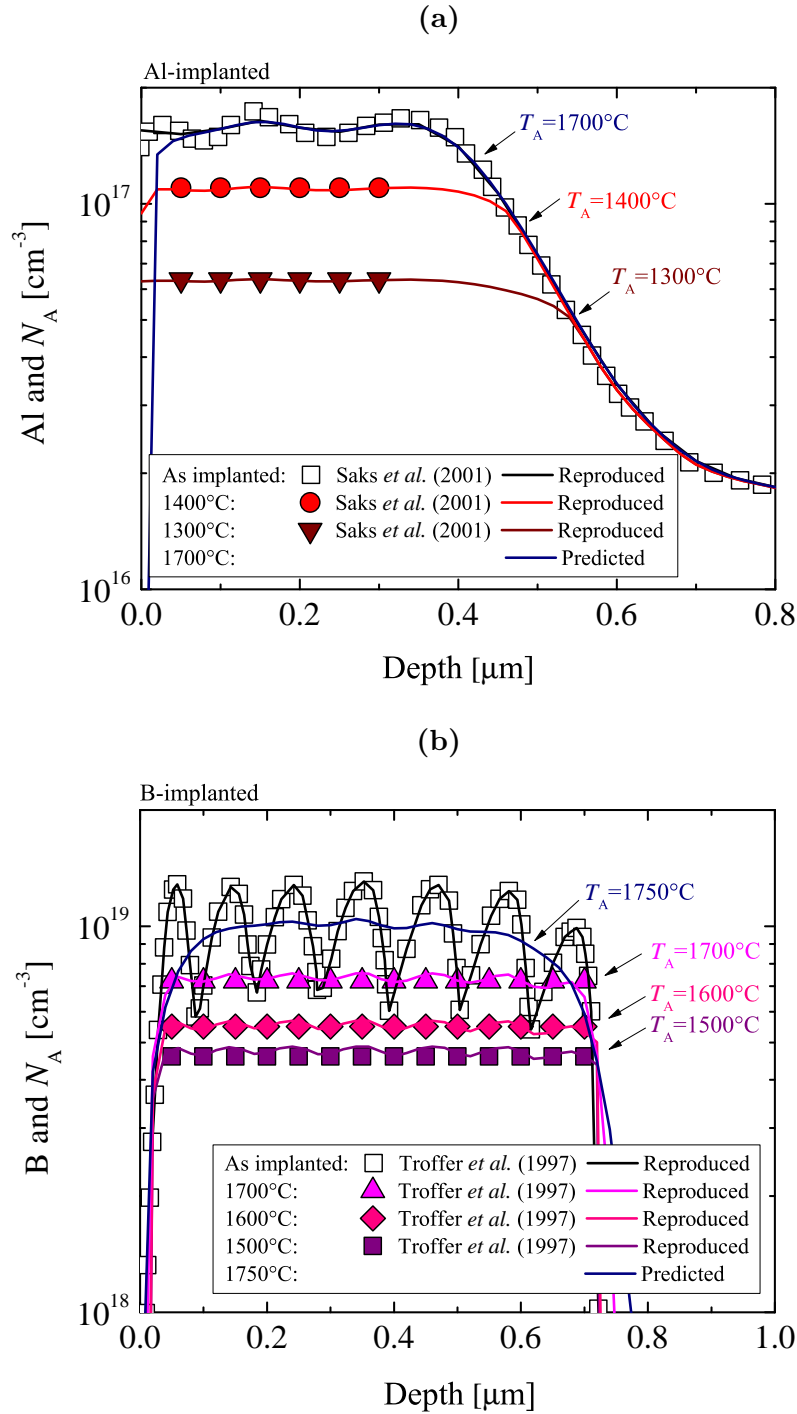


Figure 3.15: Depth profiles of implanted dopant and annealed acceptor concentrations of (a) Al- and (b) B-implanted SiC. The open symbols refer to the implanted profiles, colored symbols refer to the experimental data of average concentrations from Saks *et al.* [134] and Troffer *et al.* [147], and the solid lines refer to the reproduced and predicted results obtained in this study. The simulations have been performed with Silvaco's Victory Process simulator using Monte Carlo ion implantation, the Fermi diffusion model, and the here presented semi-empirical activation model.

To further corroborate the predictability of the semi-empirical model, device simulations of the processed Al-implanted SiC diodes are performed. The third simulation setup follows the experimental setup of Nipoti *et al.* [156], which consists of an n-type SiC wafer with a compensation concentration of  $\approx 3 \cdot 10^{15} \text{ cm}^{-3}$ , followed by several Al-implantations generating a rectangular profile with a mean concentration of  $\approx 10^{20} \text{ cm}^{-3}$ . The annealing steps are 30 min at  $T_A = 1500^\circ\text{C}$ , 30 min at  $T_A = 1600^\circ\text{C}$ , 30 min at  $T_A = 1700^\circ\text{C}$ , and 1 min at  $T_A = 1950^\circ\text{C}$ . The mean concentration of this setup exceeds the mean concentrations of the data considered for the model calibration, therefore, these simulations reflect model predictions based on the extrapolation of the model parameters. The resistivity of the variously processed devices, i.e., different annealing temperatures, is shown in Figure 3.16. The simulations show excellent agreement with the experimental data, which indicates that the model correctly predicts the device properties outside of the calibrated regions as well. The figure in addition confirms the importance of the post-implantation annealing steps, which can be seen by the four times decrease in resistivity. This further underlines the importance of the proposed activation model, as a 100% activation for high-dose implantation cannot be assumed, but must be accurately predicted, because this critically affects device performance.

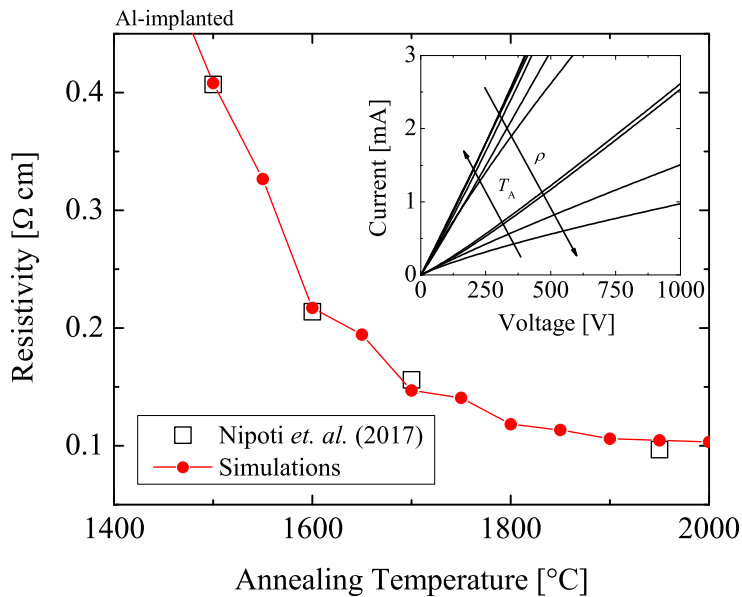


Figure 3.16: Resistivity of the Al-implanted SiC as a function of the annealing temperature. The open squares refer to the experimental data from Nipoti *et al.* [156] and the closed symbols refer to the resistivity calculated from the simulations. The inset figure shows simulation results, i.e., current as a function of voltage for samples annealed at various annealing temperatures.

## 3.4 Transient Model

Industry-related annealing steps typically take up to 30 min for low temperature anneals (1100°C–1600°C) and up to 5 min for high temperatures (1700°C–2200°C) [157]. Regardless, a time-dependent activation model can provide additional suggestions, such as, minimal time needed for sufficient activation (e.g.,  $R_{\text{act}} > 90\%$ ), to potentially optimize production costs. In addition, a time-dependent model provides deeper insights into the activation mechanism and supports further investigations of the annealing processes [158]. Therefore, in order to better understand and to be able to control annealing steps in device fabrication, a transient activation model has been developed [159] and is presented in the following.

### 3.4.1 Methodology

The preferred acceptor-type dopant species in SiC is Al for low resistivity applications [160], while the preferred donor-type dopant is P for high-dose implantations [161]. In addition, implantation and annealing steps of Al and P show potential for a wide utilization of SiC devices [130], [137], [152], [161], which is why the focus here is on Al- and P-implantation of 4H-SiC. A comprehensive collection of experimental data of various post-implantation steps of Al and P impurities in SiC has been gathered. The acceptor [130], [134], [152], [162], [163], [164] and donor [1], [138], [141], [144], [161], [164] concentrations have been obtained from experimental studies for various annealing temperatures, annealing times, and total implanted concentrations. The collected Al- and P-implanted data is plotted as a function of annealing time in Figure 3.17. As previously discussed, the experimental data has been selected such that identical crystal orientations, annealing ambients, implantation temperatures, and measuring methods are considered. This is particularly important as it enables proper model fitting for predicting the annealing temperature, annealing time, and total concentration [135]. It has been assumed that the different annealing methods (microwave, inductive, and resistive heating) result in the same activation ratios [154]. All of the selected data is based on annealing in an Ar ambient. In addition, no differences in activation rates between 4H- and 6H-SiC are assumed [134]. According to the available experimental data, the error due to this assumption is less than 5% and is thus considered negligible.

The transient model for electrical activation of dopants in SiC has been inherited and modified from the model for Si [53], which is described with a differential equation and represents the reaction of the dopants' activation processes. The active concentration of dopants in SiC is [159] modeled by

$$\frac{dC_{\text{act}}}{dt} = -\kappa \left( C_{\text{act}} - \frac{C_{\text{tot}}}{1 + \frac{C_{\text{tot}}}{C_{\text{ss}}}} \right). \quad (3.31)$$

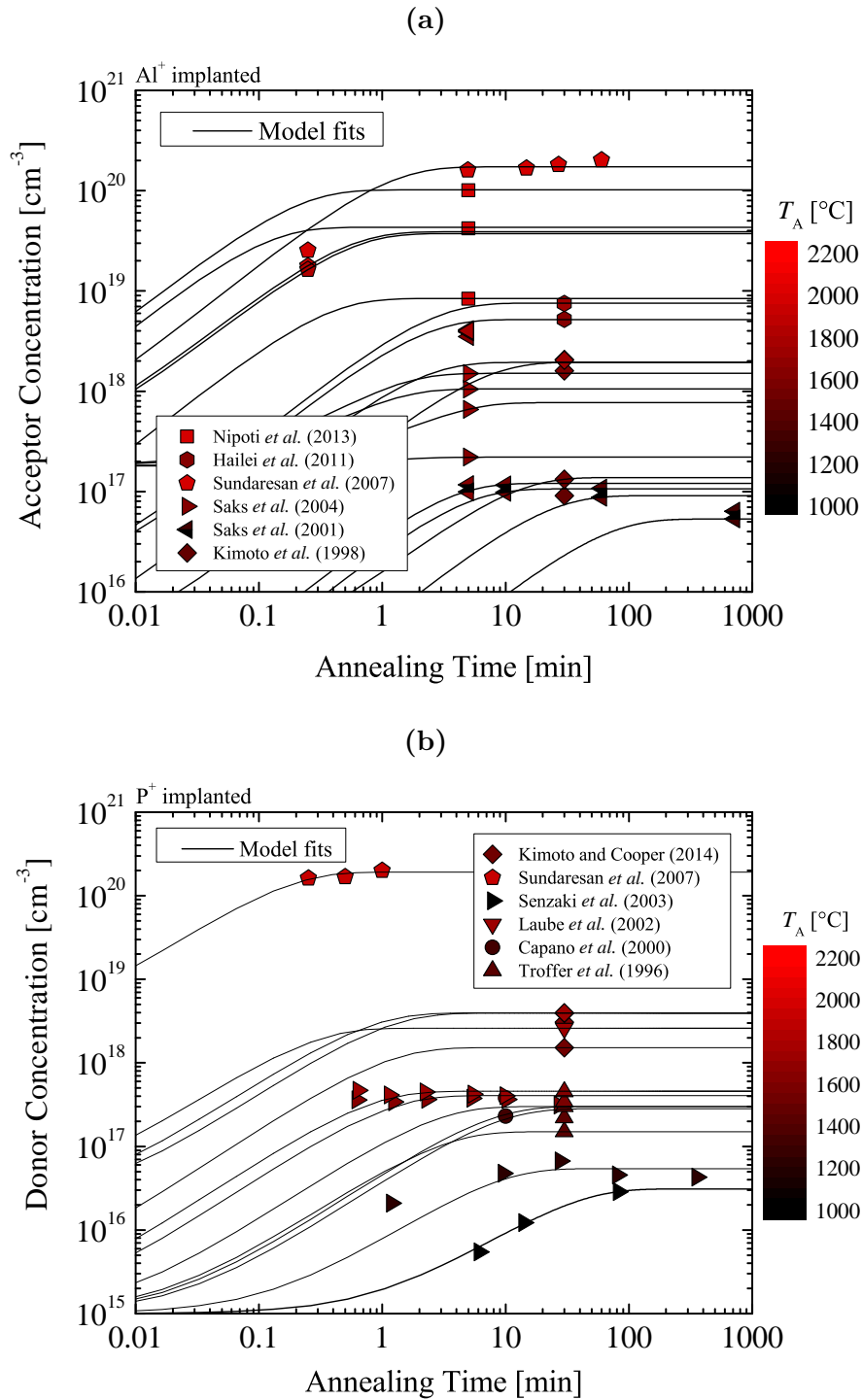


Figure 3.17: (a) Acceptor and (b) donor concentrations as a function of annealing time for various total concentrations and annealing temperatures. The data has been taken from previous experimental studies for acceptor-[130], [134], [152], [162], [163], [164] and donor [1], [138], [141], [144], [161], [164]-type doping. The solid lines refer to model fits.

$C_{\text{tot}}$  is the total implanted concentration of dopants.  $C_{\text{ss}}$  and  $\kappa$  are solid solubility and characteristic reaction rate, respectively, and are the key parameters of the model, obtained by model fitting. In the case of SiC,  $C_{\text{act}}$  is approximated to be equal to the electrically measured (i.e., Hall and sheet resistance measurements) acceptor ( $N_{\text{A}}$ ) or donor concentration ( $N_{\text{D}}$ ), which originate from the ionized dopants only.  $C_{\text{ss}}$  is the limiting parameter for the total active concentration and  $\kappa$  is the limiting parameter for the reaction rate of the activation mechanism, i.e., the slope of the curve.

### 3.4.2 Calibration

Several iterations of least squares approximation [165] have been performed for each individual data set to reduce the numerical error, when fitting the proposed activation model (3.31) to the data presented in Figure 3.17. The fitting parameters are  $C_{\text{ss}}$  and  $\kappa$ , which are individually obtained for each annealing temperature. The temperature-dependent parameters are then fitted with the Arrhenius equation [96] to ensure a continuous, interpolated, and extrapolated dependence on the annealing temperature. The calibrated Arrhenius parameters, i.e., activation energy  $E_{\text{a}}$  and pre-exponential factor  $Z$ , are summarized in Table 3.5.

The corresponding Arrhenius plots are shown in Figure 3.18. The activation energy for Al-implanted SiC is for both parameters ( $C_{\text{ss}}$  and  $\kappa$ ) higher, compared to P-implanted SiC.  $C_{\text{ss}}$  is for relatively low temperatures (around 1150°C) identical for Al and P impurities. On the contrary,  $\kappa$  is for Al and P identical for relatively high temperatures around 1950°C. For the steady state solution of the model, i.e., solution for the thermal equilibrium,  $C_{\text{ss}}$  plays a significant role by defining the upper limits of the active concentration of the dopants for particular annealing temperatures. Moreover,  $C_{\text{ss}}$  varies up to an order of magnitude between the Al and P dopants for high temperatures. Additionally, the Arrhenius plots suggest that the solubility limit for Al-implanted SiC is higher, compared to P-implanted SiC.

Table 3.5: Arrhenius parameters, i.e., activation energy and pre-exponential factor, of the solid solubility and characteristic rate for Al- and P-implanted SiC.

Dopant	$C_{\text{ss}}$		$\kappa$	
	$Z$ [ $\text{cm}^{-3}$ ]	$E_{\text{a}}$ [eV]	$Z$ [ $\text{min}^{-1}$ ]	$E_{\text{a}}$ [eV]
Al	$1.21 \cdot 10^{26}$	2.58	$5.83 \cdot 10^6$	2.72
P	$7.17 \cdot 10^{23}$	2.09	$6.51 \cdot 10^3$	1.38

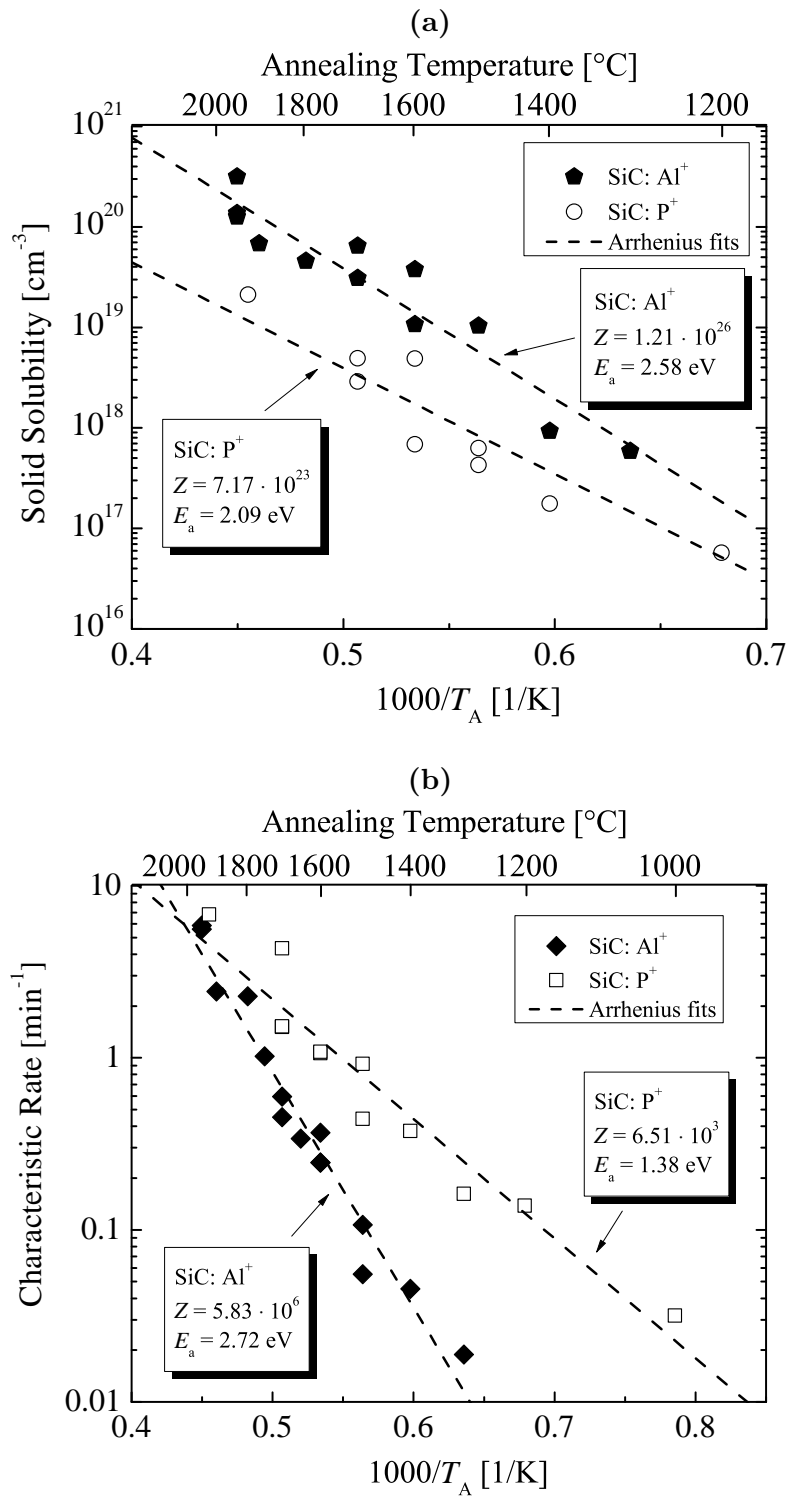


Figure 3.18: Model parameter (a) solid solubility and (b) characteristic rate as a function of annealing temperature for Al- (closed) and P-implanted (open symbols) SiC. The dashed lines refer to the fits with the Arrhenius equation.

The proposed transient model, together with the obtained model parameters, enable the prediction of the transient active concentration or activation ratio after thermal annealing steps of SiC device fabrication. In the next sections the calibrated model is analyzed and the model results are validated based on the gathered experimental data. In particular, in-depth modeling and parameter aspects are discussed, followed by actual process simulations of representative PN-junction diodes including validations with experimental data. These analyses are concluded with evaluating the electrical characteristics via device simulations in comparison to experimental data.

### 3.4.3 Characterization

The transient activation model has been characterized based on two investigations, one considering constant implanted concentration with annealing time and temperature being the independent variables, and another considering a steady state with annealing temperature and total concentration being the independent variables. The steady state case refers to the dopant activation state where a prolonged annealing treatment will not affect the concentration of activated dopants. This is typically in the range above 1000 min of annealing time. The parameter studies have been performed based on numerous (i.e.,  $10^6$ ) calculations of Al and P implantations in SiC, followed by various annealing steps. Phase diagrams of activation regions as a function of annealing temperature and annealing time are shown in Figure 3.19. Due to the Arrhenius fitting of the parameters, the results are extrapolated for certain annealing temperatures, shown with dashed lines.

The phase diagrams enable an estimation of the minimally required  $T_A$  and  $t_A$  to reach full (i.e., above 90%) activation. The phase diagrams additionally show that the phase region  $0.1 < R_{act} < 1.0$  is smaller for Al acceptors than for P donors. The difference in those areas indicates that P acceptors require less energy for activation than P donors, which is consistent with experimental findings [1]. Figure 3.19 in addition shows the steady states for different annealing temperatures. For instance, at 1700°C the steady state for Al acceptors is reached for an annealing time above  $\approx 25$  min and for P donors above  $\approx 3$  min, i.e., the activation ratio is not affected beyond these times.

In addition, it has been shown [159] that for high  $T_A$  the initial activation speed is extremely high and decreases rapidly with time. This implies that the activation process for high  $T_A$  is mostly significant for  $t_A < 5$  min. In contrast, for low  $T_A$  the initial activation speed is a few orders of magnitude lower and decreases slowly, thus  $t_A > 15$  min is required for the effective activation of impurities. The activation process for  $T_A = 1800, 2000,$  and  $2200^\circ\text{C}$  is almost instant and achieves  $> 90\%$  activation. This indicates that rapid thermal annealing methods are indeed suitable for the activation of dopants in SiC, provided that the annealing temperatures are above  $\approx 1700^\circ\text{C}$ .

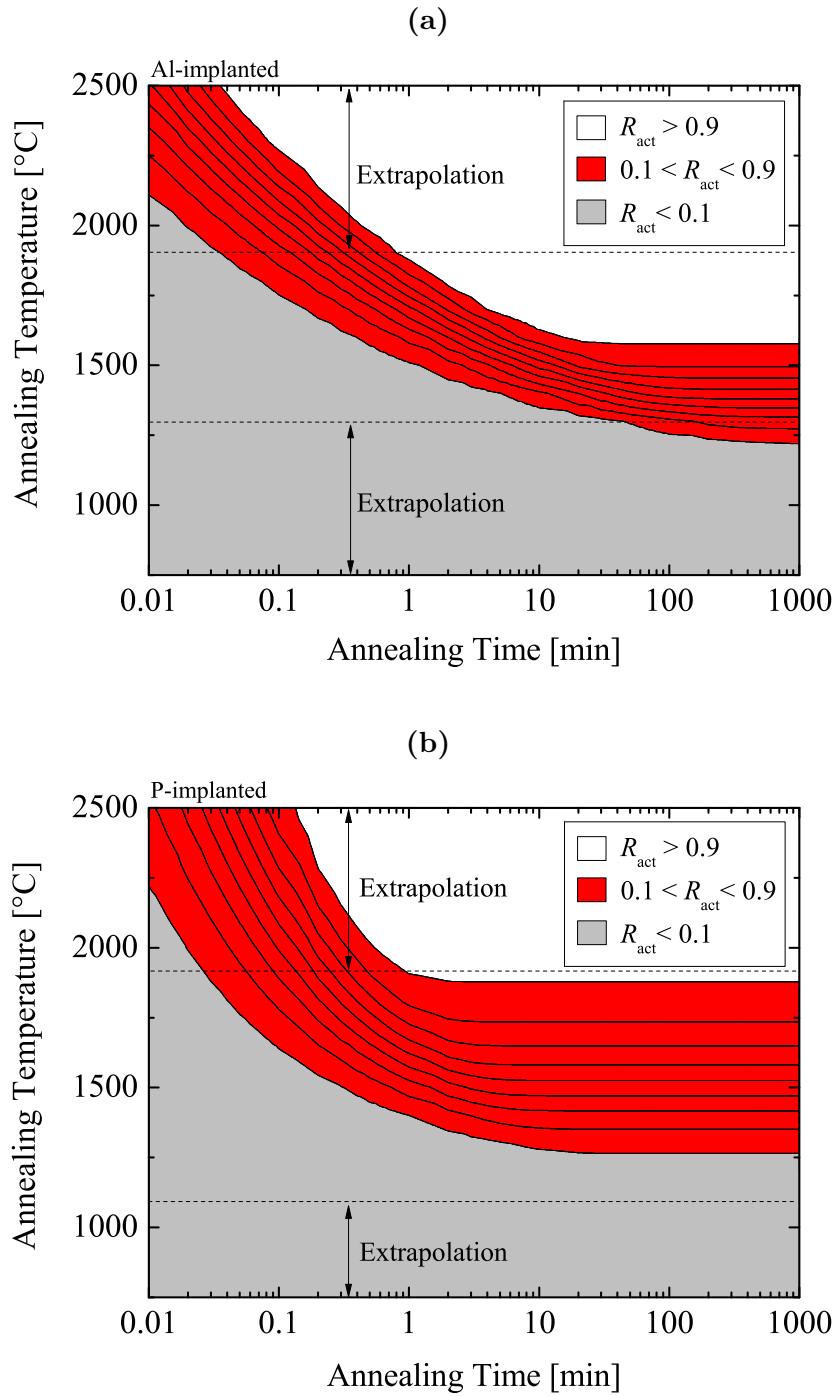


Figure 3.19: Phase diagrams of electrical activation as a function of annealing temperature and annealing time for (a) Al- and (b) P-implanted SiC. The simulations are performed for the total concentration  $C_{\text{tot}} = 1.0 \cdot 10^{18} \text{ cm}^{-3}$ . The gray, red, and white regions refer to the low, intermediate, and high activation of SiC impurities, respectively. The dashed lines are the extrapolation boundaries.

One of the significant issues of wide-bandgap semiconductors is that the rate of the dopant activation after high dose implantation (i.e., above  $10^{18} \text{ cm}^{-3}$ ) significantly decreases [152] and saturates [154]. In order to investigate the saturation effects due to high implantation doses, another parameter study is performed via calculating phase diagrams of activation regions as a function of annealing temperature and total implanted concentration, shown in Figure 3.20. These results suggest that the saturation region of the activation mechanism in SiC is temperature-dependent. As the annealing temperature increases, the boundary of the saturation region, shown with the dashed red lines, increases as well. This indicates that for annealing steps with high  $T_A$  the doping doses can be a few orders of magnitude higher than with a low  $T_A$ , while maintaining the same ratio of activation. The model predicts that annealing steps with  $T_A$  below  $1000^\circ\text{C}$  for Al-implanted and  $850^\circ\text{C}$  for P-implanted SiC do not contribute to the improvement of electrical properties, regardless of the doping dose. The white region of the phase diagram, which refers to the full dopant activation, is larger for the Al-implanted SiC compared to P-implanted SiC. This indicates that a wider span of the parameter variety can be chosen for the acceptor-type doping, while maintaining the desired high activation ratio  $> 90\%$ . These findings support the latest trend of Al being the preferable dopant for the SiC technology [160], [166], [167].

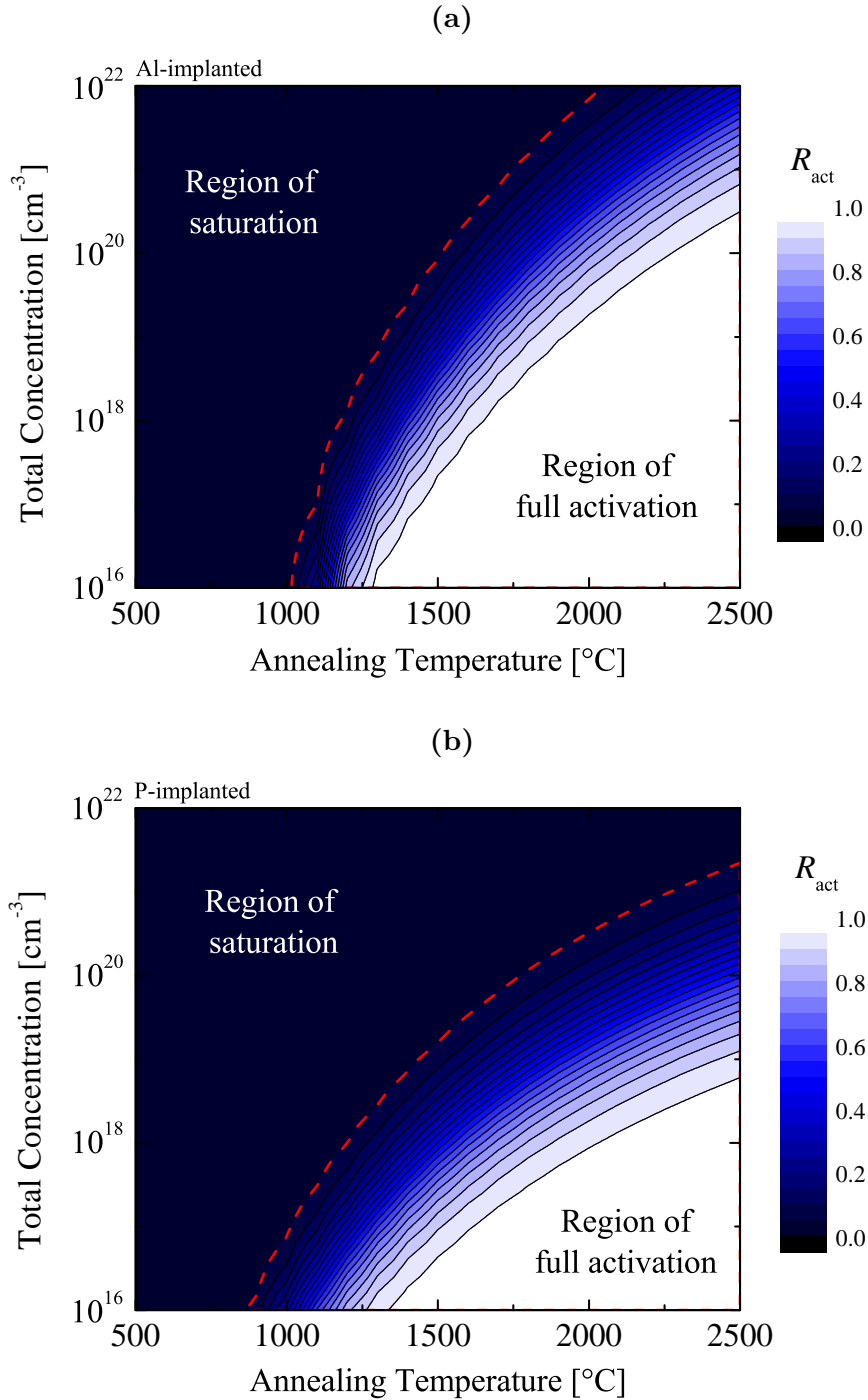


Figure 3.20: Phase diagrams of electrical activation as a function of annealing temperature and total concentration for (a) Al- and (b) P-implanted SiC. Simulations have been performed for an annealing time  $t_A = 1000$  min, i.e., steady state. The colors indicate various activation ratios ( $R_{act}$ ) and the red dashed lines indicate the boundaries of the saturation regions.

### 3.4.4 Simulations

The transient model and the parameters from Table 3.5 have been implemented into Silvaco's Victory Process simulator [53]. Various PN-junction diodes have been processed and evaluated according to model predictions. Each of the simulated PN-diodes varies with regard to the annealing temperature, annealing time, and/or total concentration. An exemplary device structure is shown in Figure 3.21 and the respective doping parameters are given in Table 3.6. The device processing setups are based on three different experimental investigations [137], [141], [161], which have been chosen to ensure a focused study of the annealing process. All of the setups include implantation of P in an Al-doped SiC substrate and a (0001) Si-face crystal orientation. The simulated processing steps are: 1) p-type (Al-doped) SiC substrate. 2) n-type (P) implantation according to the chosen setup. The Monte Carlo implantation model from the Victory Process simulator has been utilized. 3) Deposition of SiO<sub>2</sub>. 4) Annealing of implanted species according to the experimental setups. This step includes the proposed model and parameters. 5) Removal of SiO<sub>2</sub>. 6) Deposition of metal for contacts on top and bottom of the device.

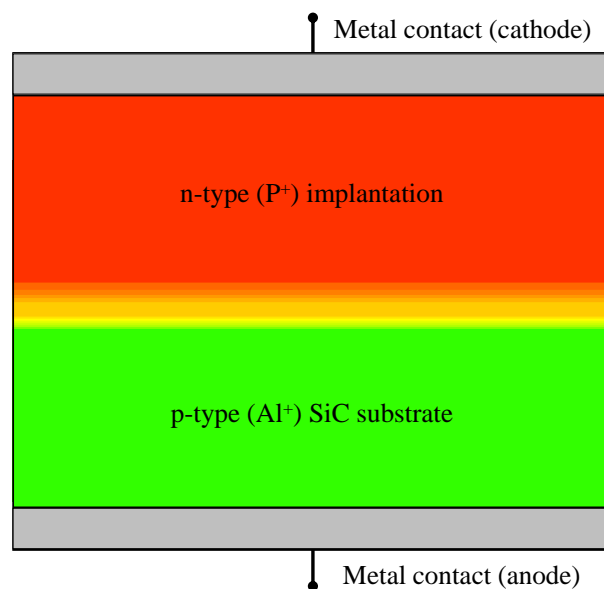


Figure 3.21: Schematic design of the PN-junction diode used in simulations utilizing the introduced transient activation model. The red and green region refer to the n- and p-type region, respectively. The gray regions indicate the contacts, i.e., cathode and anode.

Table 3.6: Implantation setups for p-type SiC (0001) Si-face.

Setup	1	2	3
Reference	Schmid <i>et al.</i> [137]	Troffer <i>et al.</i> [141]	Senzaki <i>et al.</i> [161]
Substrate Al <sup>+</sup> concentration [cm <sup>-3</sup> ]	$1.0 \cdot 10^{16}$	$1.3 \cdot 10^{17}$	$5.0 \cdot 10^{15}$
Implanted P <sup>+</sup> energies [keV]	70, 180, 320, 500, 750	70, 160, 280, 450, 600, 800, 1100, 1500, 2000	40, 70, 160, 180, 220, 250
Total fluence [cm <sup>-2</sup> ]	$1.4 \cdot 10^{16}$	$1.3 \cdot 10^{14}$	$7.0 \cdot 10^{15}$

The depth profiles, i.e., P and donor concentration, of the two implantation setups and simulations are shown in Figure 3.22. The solid lines refer to the results from the process simulations and the symbols refer to the experimental findings. The red color indicates implanted profiles of both simulations and experiments. The simulated implanted profiles of Setup 1 (Figure 3.22 (a)) and Setup 2 (Figure 3.22 (b)) are identical to the profiles from the corresponding references. The implanted species are annealed for 30 min at 1700°C and 30 min at 1550°C in the case of Setup 1 and for 30 min at 1700°C and 30 min at 1400°C in the case of Setup 2. The deviation between the results from simulation and experiment for the annealed samples is in average  $\sigma < 3\%$ . This indicates that the proposed model captures the key characteristics of the activation mechanism and provides an accurate prediction of the activation levels. It can be seen from Figure 3.22 (a) that a very low activation ratio of high-dose acceptor-type impurities is achieved after the typical annealing step, i.e., 30 min at 1700°C. Furthermore, an estimate of the required processing variables for sufficient (> 90%) activation is provided. Experimental methods have not been able to provide such an estimate due to technical limitations [137]. The prediction is based on the proposed model (blue lines) and suggests that the activation of high-dose implantation is significantly improved after an annealing step of 1 min at 2250°C. In the case of high-dose implantation  $N_D$  has been increased from  $3 \cdot 10^{18} \text{ cm}^{-3}$  to  $6 \cdot 10^{19} \text{ cm}^{-3}$ . Moreover, such simulations can provide an estimate for the shortest annealing time and lowest annealing temperature, which result in a desired active concentration. For instance, for Setup 2, it is evident that an annealing step of 5 min at 1650°C is sufficient to achieve an identical activation as compared to annealing for 30 min at 1700°C. This underlines that already small temperature variations (e.g., 50°C) have a strong impact on the activation process.

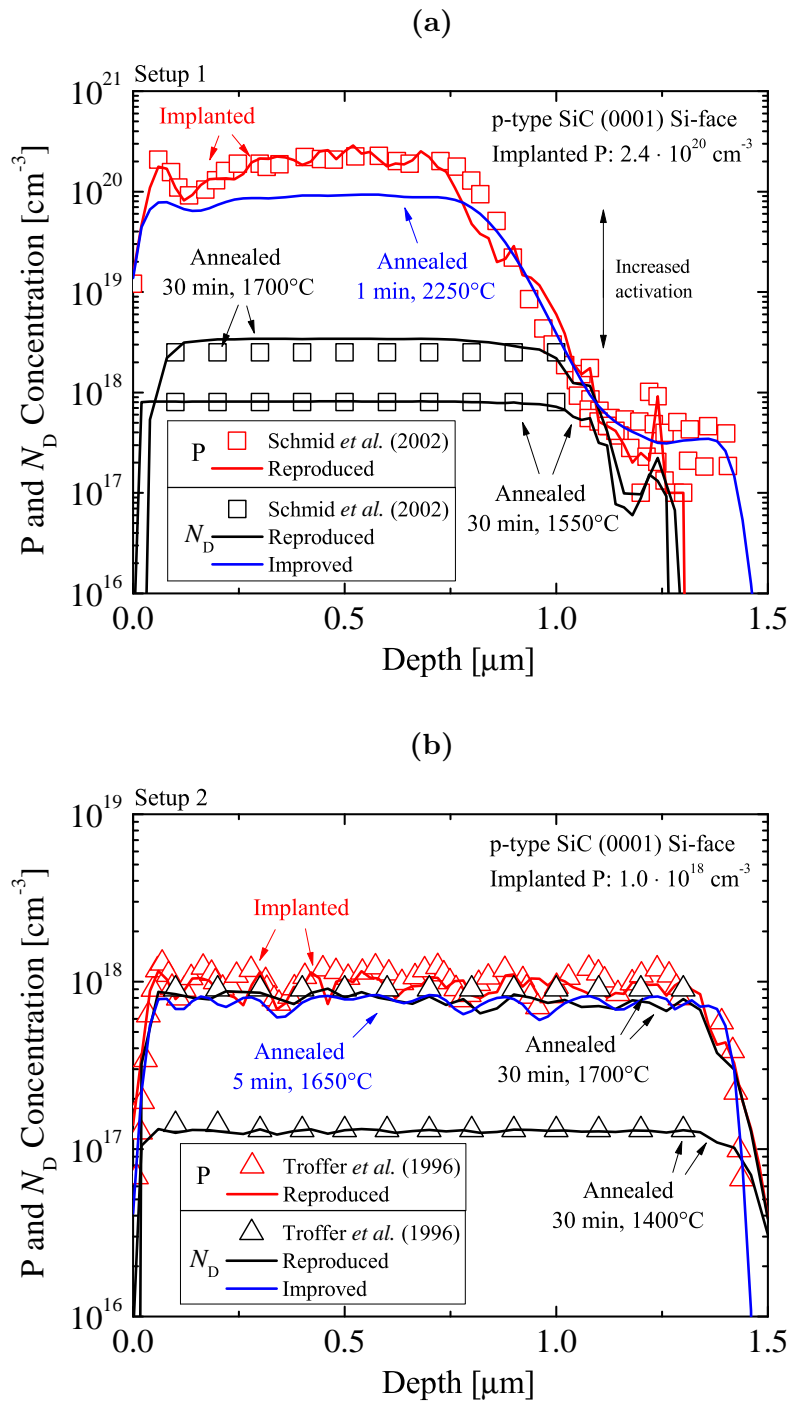


Figure 3.22: Depth profiles of P concentration and donor concentration utilizing implantation (a) Setup 1 and (b) Setup 2. The red and black symbols are P and  $N_D$  from [137], [141], respectively, the red and black lines are reproduced P and  $N_D$ , respectively, and the blue lines are predicted  $N_D$ .

According to the obtained depth profiles of Setup 1 and Setup 2, device simulations have been performed to characterize the electrical properties of the implanted SiC after the investigated annealing steps. In order to characterize the processed PN-diodes, the carrier concentration as a function of sample temperature is investigated and shown in Figure 3.23. The comparison of the experimental data (red symbols) and simulation results (black lines) clearly demonstrates a very low deviation, in average  $\sigma < 1\%$ . The PN-junction diode, processed with the previously proposed annealing step from Setup 1, shows improved device characteristics (Figure 3.23 (a), blue line). The carrier concentration is significantly increased by one order of magnitude, which provides better overall device operation. Moreover, the diode, which is fabricated with the proposed annealing step from Setup 2 (i.e., reduced time and temperature), shows an almost identical behavior (Figure 3.23 (b), blue line) as the diode with the non-modified annealing step. Small variations between the two annealing steps are evident in extreme operation temperatures, i.e, below 150 K and above 700 K, but are almost identical in the typical device operation regime, i.e., 200 – 600 K. Thus, the shorter annealing step is sufficient to achieve the same characteristics yet within considerable shorter time.

The simulation capabilities of the transient model are further evaluated by processing SiC diodes based on the implantation and annealing parameters of Setup 3 (cf. Table 3.6). Numerous process simulations of the PN-junction diodes have been performed followed by device simulations to obtain the current-voltage (IV) characteristics of each individual device. This approach, i.e., numerous process simulations, which are distinctive in the annealing variables only, provides a focused investigation of the annealing steps. Various  $t_A$  from 0.01 min to 1000 min at  $T_A$  from 1200°C to 1700°C have been investigated. The IV plots for various  $t_A$  and  $T_A$  are shown in Figure 3.24. For the sake of readability, only the two extreme conditions are shown, i.e.,  $T_A = 1200$  and 1700°C. The knee voltage is, regardless of the processing conditions,  $\approx 2.5$  V, which is approximately three times higher than that of an equivalent diode based on Si. It becomes clear from the results, that both annealing variables,  $T_A$  and  $t_A$ , significantly affect the slope of the IV characteristics and consequently the resistance of the samples. The IV plots (Figure 3.24) have been used to calculate the resistance-time characteristics of each individual device. The sheet resistance is obtained from the slope of the IV plots and the diode geometries for various  $t_A$  and  $T_A$ , as shown in Figure 3.25. For  $T_A > 1600^\circ\text{C}$  the sheet resistance decreases until  $t_A \approx 1$  min. This implies that for high annealing temperatures a rapid annealing step is sufficient. In this case no significant decrease of the sheet resistance is observed for  $t_A > 1$  min. On the other hand, low-temperature annealing shows a continuous decrease of the sheet resistance over 1000 min. The figure in addition suggests that the sheet resistance is reduced for more than  $500 \Omega/\text{sq}$  between the annealing step of  $T_A = 1200^\circ\text{C}$  and  $1700^\circ\text{C}$ . The comparison of the results (solid lines) to the experimental findings (symbols) shows a very good agreement, i.e., in average less than 5% deviation. This implies that the proposed model provides a very accurate prediction of the annealing temperature-dependent sheet resistance of SiC devices.

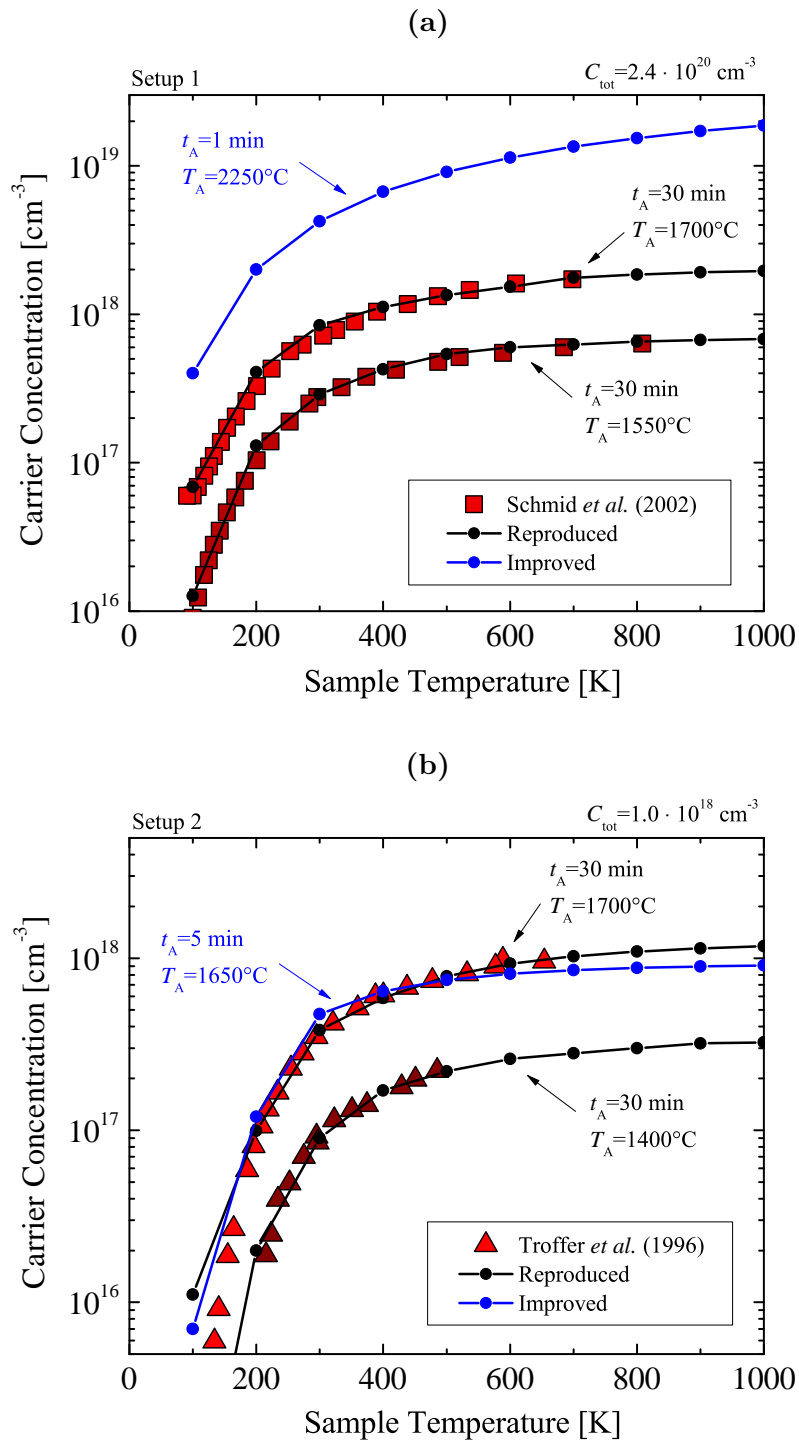


Figure 3.23: Carrier concentration as a function of sample temperature utilizing implantation (a) Setup 1 and (b) Setup 2. The symbols refer to experimental data from [137], [141], the black lines are simulation results from reproduced depth profiles, and the blue lines are simulation results from predicted depth profiles. The reproduced and predicted depth profiles are shown in Figure 3.22.

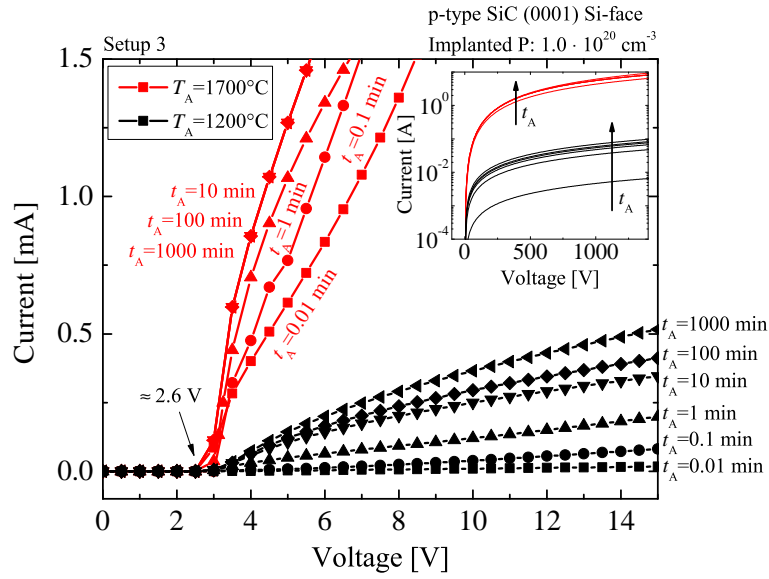


Figure 3.24: Current as a function of voltage of the PN-junction diodes annealed for  $t_A = 0.01, 0.1, 1, 10, 100,$  and  $1000$  min at  $T_A = 1200$  and  $1700^\circ\text{C}$ , utilizing implantation Setup 3.

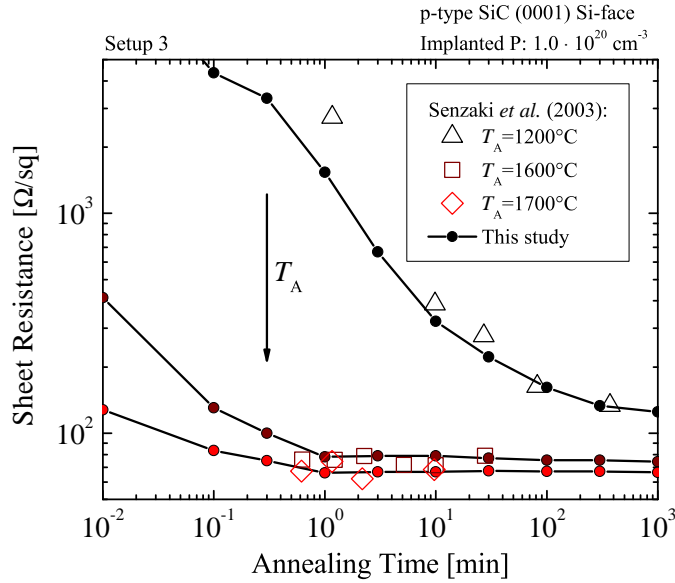


Figure 3.25: Sheet resistance as a function of annealing time of the PN-junction diodes annealed for various  $t_A$  at  $T_A = 1200, 1600,$  and  $1700^\circ\text{C}$ , utilizing implantation Setup 3. The symbols refer to the experimental data [161] and the lines are results from our simulations.

## 3.5 Summary of Research Achievements

In summary, within the scope of SiC dopant activation, the following research goals have been achieved:

1. A novel temperature-dependent model for activation of Al-, B-, P-, and N-implanted SiC has been developed and calibrated, which enables accurate predictions of doping profiles for arbitrary temperatures after post-implantation annealing steps [136].
2. Two activation models, a semi-empirical model and a transient model, which differ in the number of independent variables, have been calibrated for Al-, B-, P-, and N-implanted SiC. The models have been characterized based on extensive simulations and have been verified via comparisons with experimental data. Finally, numerous process and device simulations have been performed in order to evaluate the modeling approaches and parameters [154], [159].



## 4 Conclusions

State-of-the-art technologies as well as novel modeling and simulation approaches for SiC device fabrication steps, in particular, oxidation and post-implantation annealing, have been presented. More concretely, the main focus has been on thermal oxidation and electrical activation of various dopants. Important SiC properties, applications, and device fabrication technologies have been discussed, followed by a brief overview of TCAD. The required background for modeling and simulation of oxidation and annealing has been provided and the developed models and model extensions - representing the core contributions of this thesis - have been discussed in detail. The modeling approaches have been verified with process and device simulations based on reference SiC-based applications.

SiC is a semiconductor with an energy bandgap of 3.2 eV and is thus highly desirable for high-power and high-temperature applications due to its outstanding electric breakdown field of 3 MV/cm and thermal conductivity of 3.7 W/cmK. As many other materials, SiC exhibits various polytypes, which differ in the stacking sequence of the layers. For semiconductor device applications 4H-SiC is the most promising SiC polytype and thus commonly utilized and is therefore the focus of this work. Due to the hexagonal structure of SiC many crystallographic faces are available. However, typically the (0001) Si-, (11 $\bar{2}$ 0) a-, (1 $\bar{1}$ 00) m-, or (000 $\bar{1}$ ) C-face is considered due to the crystal symmetry.

The first part of the thesis deals with thermal oxidation of SiC, which is one of the most important processing steps of fabricating MOS devices in order to form SiO<sub>2</sub>, i.e., an oxide with an energy bandgap of 8.9 eV. Oxidation of SiC is a complex non-linear chemical process and thus requires accurate modeling techniques in order to be able to correctly predict oxide thicknesses. To set the stage, the three SiC oxidation modeling techniques, i.e., the Deal-Grove model, Massoud's model, and the C and Si emission model, have been presented and discussed in detail. The most accurate and advanced model is to this day Massoud's model, which has thus been used to fit experimental data and to obtain model parameters with low numerical fitting errors. Due to the orientation dependence of SiC (induced by the hexagonal crystal structure of 4H-SiC), the model parameters have been obtained for the four crystal faces, i.e., Si, a, m, and C. In order to introduce temperature dependence into the parameters, the growth rate coefficients have been fitted with the Arrhenius equation to obtain activation energies and pre-exponential factors for each crystal orientation: 4 model parameters times 4 faces times 2 Arrhenius parameters result in 32 parameters, which have all

been analyzed and calibrated. Interface reaction rates of SiC oxidation are similar for the Si- and C-face as well as for the a- and m-face, but for these orientations, the areal density of atoms and the mechanical stress effects are different. The oxidation rates are therefore the highest for the C-face followed by the m-, a-face, and lastly the Si-face. All the growth rate coefficients play an important role in the oxidation anisotropy of SiC. From the predicted oxidation growth rates it has been concluded that the saturation of the oxide growth is highest for the Si-face and the initial oxide enhancement is strongest for the m- and a-face.

In order to be able to utilize the obtained oxidation parameters in an actual process simulation, an interpolation method has been proposed to compute oxidation growth rate coefficients for arbitrary 3D problems. The interpolation method includes a well-known anisotropy of the oxidation of the Si- and C-face, as well as the anisotropic behavior of the m- and a-face. The interpolation method consists of six maxima and six minima (corresponding to the crystal symmetry in the shape of a star) in the  $x$ - $y$  plane, which intersects with the origin of the unit cell. In the  $x$ - $z$  and  $y$ - $z$  planes the method consists of a tangent-continuous union of two half-ellipses. The interpolation method has been used together with Massoud's model to perform 2D and 3D simulations of the thermal oxidation of SiC. These results have been proven to be in a good agreement with experimental findings from the literature.

Additionally, ReaxFF MD simulations have been performed in order to investigate the early stage of SiC oxidation for various crystallographic faces. The time evolution of the Si, C, and O atoms incorporated into the crystal structure has been extracted and analyzed for the considered oxidation temperatures ranging from 900°C to 1200°C. Oxide thicknesses have been accurately determined from the simulation results showing that even in the early stage of SiC oxidation (up to 1 ns) an orientation dependence is evident. The initial oxide thickness has been found to be approximately 2.7 nm. The comparison between the emitted Si and C species from the SiC crystal has shown a three-times higher emission of the C interstitials. An unexpected maximum has been observed for the time evolution of the Si and C emission rates between  $10^4$  and  $10^5$  fs. Emissions of Si and C have been observed to be orientation-dependent as well. The calculated growth rates indicate that the C-face has the highest oxidation rate, followed by the m-, a-, and Si-face. Furthermore, the differences in growth rates between the various faces are decreasing with time.

The second part of the thesis focuses on the electrical activation of dopants in SiC, introducing three novel modeling approaches, i.e., the activation ratio model, the semi-empirical model, and the transient model. All the discussed models enable to augment process simulations by an accurate prediction of the active concentration of dopants, but differ in the number of independent variables, i.e., annealing temperature, total implanted concentration, and annealing time. Each of the models has been fitted to the pre-processed experimental data of Al-, B-, P-, and N-implanted SiC. The obtained model parameters have in turn been fitted with the Arrhenius equation to incorporate temperature dependence. Extensive simulations have been performed to characterize

and evaluate each of the models via comparisons to reference experimental data. The activation ratio model has predicted a 50% activation for P-, N-, Al-, and B-implanted SiC at annealing temperatures 1475°C, 1515°C, 1570°C, and 1640°C, respectively. Results from the semi-empirical model have shown that for low-dose implantations ( $10^{15} \text{ cm}^{-3}$ ) relatively high activation ratios have been achieved for the temperatures below 1200°C, e.g., a full activation was achieved at 1070°C for Al- and 1010°C for B-implanted SiC. In contrast, for high-dose implantations ( $10^{20} \text{ cm}^{-3}$ ) the full activation of Al impurities was not achieved even at very high temperatures ( $> 2200^\circ\text{C}$ ), but B impurities reached full activation ( $> 90\%$ ) at 2010°C. Results from the transient model have further corroborated that the annealing time has profound effects for anneals with  $< 30$  min and that the activation is dopant-specific. For the cases of annealing time  $< 1$  min, the dopants have been fully activated for temperatures above 2000°C. For longer annealing times ( $> 1$  min) the donor- and acceptor-type dopants have exhibited various differences in annealing temperatures as well as the total implanted concentrations. On top of that, simulation results have suggested that the saturation effects of the SiC activation processes are temperature-dependent.

To sum up, this thesis presents key contributions to SiC modeling capabilities in the area of oxidation and annealing. The formulated research goals presented in Section 1.4 have been met. The novel modeling capabilities as well as the empirically determined parameters enable highly accurate predictions of 2D and in particular 3D oxidation and annealing processing steps and are thus of paramount importance to TCAD processing tools. All developed models have been calibrated and evaluated using extensive process and device simulation studies. Finally, many fundamental questions have been answered, based on the obtained results, further extending the understanding of SiC on the material but also on the device fabrication level.



# Bibliography

- [1] T. Kimoto and J. A. Cooper. *Fundamentals of Silicon Carbide Technology: Growth, Characterization, Devices and Applications*. John Wiley & Sons, 2014. DOI: 10.1002/9781118313534.
- [2] J. W. Palmour, S. Allen, B. Hull, E. Balkas, Y. Khlebnikov, and A. Burk. “Current Progress in SiC Power MOSFETs and Materials”. 2017, pp. 23–26.
- [3] X. She, A. Q. Huang, Ó. Lucía, and B. Ozpineci. “Review of Silicon Carbide Power Devices and Their Applications”. *IEEE Transactions on Industrial Electronics* 64.10 (2017), pp. 8193–8205. DOI: 10.1109/TIE.2017.2652401.
- [4] H. Moissan. “Nouvelles Recherches Sur la Météorité de Cañon Diablo”. *Comptes Rendus* 139 (1904), pp. 773–86.
- [5] E. G. Acheson. “Production of Artificial Crystalline Carbonaceous Materials”. *United States Patent 492,767* 28.02.93 (1893).
- [6] J. A. Lely. “Darstellung von Einkristallen von Silicium Carbid und Beherrschung von Art und Menge der Eingebauten Verunreinigungen”. *Berichte der Deutschen Keramischen Gesellschaft* 32 (1955), pp. 229–236.
- [7] Y. M. Tairov and V. F. Tsvetkov. “General Principles of Growing Large-Size Single Crystals of Various Silicon Carbide Polytypes”. *Journal of Crystal Growth* 52.1 (1981), pp. 146–150. DOI: 10.1016/0022-0248(81)90184-6.
- [8] D. L. Barrett, J. P. McHugh, H. M. Hobgood, R. H. Hopkins, P. G. McMullin, R. C. Clarke, and W. J. Choyke. “Growth of Large SiC Single Crystals”. *Journal of Crystal Growth* 128.1-4 (1993), pp. 358–362. DOI: 10.1016/0022-0248(93)90348-z.
- [9] M. F. Brady, W. H. Brixius, G. Fechko, R. C. Glass, D. Henshall, J. R. Jenny, R. T. Leonard, D. P. Malta, S. G. Müller, V. F. Tsvetkov, and H. C. Calvin. “Status of Large Diameter SiC Crystal Growth for Electronic and Optical Applications”. *Materials Science Forum* 338 (2000), pp. 3–8. DOI: 10.4028/www.scientific.net/msf.338-342.3.
- [10] G. L. Harris. *Properties of Silicon Carbide*. INSPEC, 1995.
- [11] A. Saha and J. A. Cooper. “A 1-kV 4H-SiC Power DMOSFET Optimized for Low On-Resistance”. *IEEE Transactions on Electron Devices* 54.10 (2007), pp. 2786–2791. DOI: 10.1109/TIE.2017.2652401.

- [12] W. J. Choyke, H. Matsunami, and G. Pensl. *Silicon Carbide: Recent Major Advances*. Springer-Verlag Berlin Heidelberg, 2004. DOI: 10.1007/978-3-642-18870-1.
- [13] R. Cheung. *Silicon Carbide Microelectromechanical Systems for Harsh Environments*. World Scientific, 2006. DOI: 10.1142/9781860949098.
- [14] H. Morkoc, S. Strite, G. B. Gao, M. E. Lin, B. Sverdlov, and M. Burns. “Large-Band-Gap SiC, III-V Nitride, and II-VI ZnSe-Based Semiconductor Device Technologies”. *Journal of Applied Physics* 76.3 (1994), pp. 1363–1398. DOI: 10.1063/1.358463.
- [15] P. T. Landsberg. *Basic Properties of Semiconductors*. Elsevier, 2016.
- [16] A. Shima, H. Shimizu, Y. Mori, M. Sagawa, K. Konishi, R. Fujita, T. Ishigaki, N. Tega, K. Kobayashi, S. Sato, and Y. Shimamoto. “3.3 kV 4H-SiC DMOSFET with Highly Reliable Gate Insulator and Body Diode”. *Materials Science Forum* 897 (2016), pp. 493–496. DOI: 10.4028/www.scientific.net/MSF.897.493.
- [17] V. Soler, M. Cabello, M. Berthou, J. Montserrat, J. Rebollo, P. Godignon, A. Mihaila, M. R. Rogina, A. Rodríguez, and J. Sebastián. “High-Voltage 4H-SiC Power MOSFETs With Boron-Doped Gate Oxide”. *IEEE Transactions on Industrial Electronics* 64.11 (2017), pp. 8962–8970. DOI: 10.1109/tie.2017.2723865.
- [18] C. Hammond. *The Basics of Crystallography and Diffraction*. Vol. 21. Oxford University Press, 2015.
- [19] C. I. Harris and V. V. Afanas'ev. “SiO<sub>2</sub> as an Insulator for SiC Devices”. *Microelectronic Engineering* 36.1-4 (1997), pp. 167–174. DOI: 10.1016/s0167-9317(97)00041-5.
- [20] P. G. Neudeck, R. S. Okojie, and L.-Y. Chen. “High-Temperature Electronics - A Role for Wide Bandgap Semiconductors?” *Proceedings of the IEEE* 90.6 (2002), pp. 1065–1076. DOI: 10.1109/jproc.2002.1021571.
- [21] W. Suttrop, G. Pensl, W. J. Choyke, R. Stein, and S. Leibenzeder. “Hall Effect and Infrared Absorption Measurements on Nitrogen Donors in 6H-Silicon Carbide”. *Journal of Applied Physics* 72.8 (1992), pp. 3708–3713. DOI: 10.1063/1.352318.
- [22] J. B. Casady and R. W. Johnson. “Status of Silicon Carbide (SiC) as a Wide-Bandgap Semiconductor for High-Temperature Applications: A Review”. *Solid-State Electronics* 39.10 (1996), pp. 1409–1422. DOI: 10.1016/0038-1101(96)00045-7.
- [23] J. A. Cooper and A. Agarwal. “SiC Power-Switching Devices-The Second Electronics Revolution?” *Proceedings of the IEEE* 90.6 (2002), pp. 956–968. DOI: 10.1109/jproc.2002.1021561.

- [24] C. Kittel, P. McEuen, and P. McEuen. *Introduction to Solid State Physics*. Vol. 8. Wiley, 1996.
- [25] G. Pensl, H. Morkoc, B. Monemar, and E. Janzen. “Silicon Carbide, III-Nitrides and Related Materials. I”. *Materials Science Forum* 264 (1997), p. 672. DOI: 10.4028/www.scientific.net/MSF.264-268.
- [26] W. M. Chen, N. T. Son, E. Janzen, D. M. Hofmann, and B. K. Meyer. “Effective Masses in SiC Determined by Cyclotron Resonance Experiments”. *Physica Status Solidi (a)* 162.1 (1997), pp. 79–93. DOI: 10.1002/1521-396x(199707)162:1<79::aid-pssa79>3.3.co;2-4.
- [27] S. M. Sze. *Semiconductor Devices: Physics and Technology*. John Wiley & Sons, 2008.
- [28] A. Elasser and T. P. Chow. “Silicon Carbide Benefits and Advantages for Power Electronics Circuits and Systems”. *Proceedings of the IEEE* 90.6 (2002), pp. 969–986. DOI: 10.1109/jproc.2002.1021562.
- [29] W. J. Choyke, R. P. Devaty, L. L. Clemen, M. F. MacMillan, and M. Yoganathan. “Optical Properties and Characterization of SiC and III-V Nitrides”. *Silicon Carbide and Related Materials 1995* 142 (1996), pp. 257–262.
- [30] G. Wellenhofer and U. Rössler. “Global Band Structure and Near-Band-Edge States”. *Physica Status Solidi (b)* 202.1 (1997), pp. 107–123. DOI: 10.1002/1521-3951(199707)202:1<107::aid-pssb107>3.0.co;2-9.
- [31] R. R. Lamichhane, N. Ericsson, S. Frank, C. Britton, L. Marilino, A. Mantooh, M. Francis, P. Shepherd, M. Glover, S. Perez, T. McNutt, B. Whitaker, and Z. Cole. “A Wide Bandgap Silicon Carbide (SiC) Gate Driver for High-Temperature and High-Voltage Applications”. *Proceedings of the IEEE International Symposium on Power Semiconductor Devices & IC’s (ISPSD)*. 2014, pp. 414–417. DOI: 10.1109/ispsd.2014.6856064.
- [32] Z. Wang, X. Shi, L. M. Tolbert, F. F. Wang, Z. Liang, D. Costinett, and B. J. Blalock. “A High Temperature Silicon Carbide MOSFET Power Module with Integrated Silicon-on-Insulator-Based Gate Drive”. *IEEE Transactions on Power Electronics* 30.3 (2015), pp. 1432–1445. DOI: 10.1109/ecce.2014.6953997.
- [33] B. Whitaker, A. Barkley, Z. Cole, B. Passmore, D. Martin, T. R. McNutt, A. B. Lostetter, J. S. Lee, and K. Shiozaki. “A High-Density, High-Efficiency, Isolated On-Board Vehicle Battery Charger Utilizing Silicon Carbide Power Devices”. *IEEE Transactions on Power Electronics* 29.5 (2014), pp. 2606–2617. DOI: 10.1109/tpel.2013.2279950.
- [34] M. Östling, R. Ghandi, and C.-M. Zetterling. “SiC Power Devices—Present Status, Applications and Future Perspective”. *Proceedings of the International Symposium on Power Semiconductor Devices and ICs (ISPSD)*. 2011, pp. 10–15. DOI: 10.1109/ISPSD.2011.5890778.

- [35] R. Trew. “SiC and GaN Transistors-Is There One Winner for Microwave Power Applications?” *Proceedings of the IEEE* 90.6 (2002), pp. 1032–1047. DOI: 10.1109/JPROC.2002.1021568.
- [36] B. J. Baliga. *Fundamentals of Power Semiconductor Devices*. Springer-Verlag US, 2008. DOI: 10.1007/978-0-387-47314-7.
- [37] H. Amano, S. Kamiyama, and I. Akasaki. “Impact of Low-Temperature Buffer Layers on Nitride-Based Optoelectronics”. *Proceedings of the IEEE* 90.6 (2002), pp. 1015–1021. DOI: 10.1109/jproc.2002.1021566.
- [38] S. Dimitrijević, J. Han, H. A. Moghadam, and A. Aminbeidokhti. “Power-Switching Applications Beyond Silicon: Status and Future Prospects of SiC and GaN Devices”. *MRS Bulletin* 40.5 (2015), pp. 399–405. DOI: 10.1557/mrs.2015.89.
- [39] W. Wondrak, R. Held, E. Niemann, and U. Schmid. “SiC Devices for Advanced Power and High-Temperature Applications”. *IEEE Transactions on Industrial Electronics* 48.2 (2001), pp. 307–308. DOI: 10.1109/41.915409.
- [40] K. C. Reinhardt and M. A. Marciniak. “Wide-Bandgap Power Electronics for the More Electric Aircraft”. *Proceedings of the Intersociety Energy Conversion Engineering Conference (IECEC)*. 1996, pp. 127–132. DOI: 10.1109/iecec.1996.552858.
- [41] A. S. Bakin, S. I. Dorozhkin, and A. S. Zubrilov. “6H- and 4H-Silicon Carbide for Device Applications”. *Proceedings of the International High Temperature Electronics Conference (HITEC)*. 1998, pp. 253–256. DOI: 10.1109/HITEC.1998.676798.
- [42] J. Millan, P. Godignon, X. Perpina, A. Pérez-Tomás, and J. Rebollo. “A Survey of Wide Bandgap Power Semiconductor Devices”. *IEEE Transactions on Power Electronics* 29.5 (2014), pp. 2155–2163. DOI: 10.1109/TPEL.2013.2268900.
- [43] R. C. Clarke and J. W. Palmour. “SiC Microwave Power Technologies”. *Proceedings of the IEEE* 90.6 (2002), pp. 987–992. DOI: 10.1109/JPROC.2002.1021563.
- [44] G. S. May and C. J. Spanos. *Fundamentals of Semiconductor Manufacturing and Process Control*. John Wiley & Sons, 2006.
- [45] R. Courtland. “Moore’s Law’s Next Step: 10 Nanometers”. *IEEE Spectrum* 54.1 (2017), pp. 52–53. DOI: 10.1109/MSPEC.2017.7802750.
- [46] G. Moore. “Moore’s law”. *Electronics Magazine* 38.8 (1965), p. 114.
- [47] R. R. Schaller. “Moore’s Law: Past, Present and Future”. *IEEE Spectrum* 34.6 (1997), pp. 52–59. DOI: 10.1109/6.591665.
- [48] C. C. Mann. “The End of Moore’s Law?” *Technology Review* 103.3 (2000), pp. 42–48.

- [49] B. El-Kareh. *Fundamentals of Semiconductor Processing Technology*. Springer-Verlag New York, 1995. DOI: 10.1007/978-1-4615-2209-6.
- [50] C.-M. Zetterling. *Process Technology for Silicon Carbide Devices*. Vol. 2. INSPEC, 2002.
- [51] S. Selberherr. *Analysis and Simulation of Semiconductor Devices*. Springer-Verlag Wien, 1984. DOI: 10.1007/978-3-7091-8752-4.
- [52] H. K. Gummel. “A Self-Consistent Iterative Scheme for One-Dimensional Steady State Transistor Calculations”. *IEEE Transactions on Electron Devices* 11.10 (1964), pp. 455–465. DOI: 10.1109/T-ED.1964.15364.
- [53] *Silvaco’s Victory Process Simulator*. [https://www.silvaco.com/products/tcad/process\\_simulation/victory\\_process/victory\\_process.html](https://www.silvaco.com/products/tcad/process_simulation/victory_process/victory_process.html). (accessed September 5, 2018).
- [54] *Silvaco’s Victory Device Simulator*. [https://www.silvaco.com/products/tcad/device\\_simulation/victory\\_device/victory\\_device.html](https://www.silvaco.com/products/tcad/device_simulation/victory_device/victory_device.html). (accessed September 5, 2018).
- [55] S. Dhar, Y. W. Song, L. C. Feldman, T. Isaacs-Smith, C. C. Tin, J. R. Williams, G. Chung, T. Nishimura, D. Starodub, T. Gustafsson, and E. Garfunkel. “Effect of Nitric Oxide Annealing on the Interface Trap Density Near the Conduction Bandedge of 4H–SiC at the Oxide/(1120) 4H–SiC Interface”. *Applied Physics Letters* 84.9 (2004), pp. 1498–1500. DOI: 10.1063/1.1651325.
- [56] W. M. Haynes. *CRC Handbook of Chemistry and Physics*. CRC press, 2014.
- [57] E. Rosencher, A. Straboni, S. Rigo, and G. Amsel. “An O<sup>18</sup> Study of the Thermal Oxidation of Silicon in Oxygen”. *Applied Physics Letters* 34.4 (1979), pp. 254–256. DOI: 10.1063/1.90771.
- [58] T. Hosoi, D. Nagai, T. Shimura, and H. Watanabe. “Exact Evaluation of Interface-Reaction-Limited Growth in Dry and Wet Thermal Oxidation of 4H–SiC (0001) Si-face Surfaces”. *Japanese Journal of Applied Physics* 54.9 (2015), p. 098002. DOI: 10.7567/jjap.54.098002.
- [59] J. Schmitt and R. Helbig. “Oxidation of 6H-SiC as Function of Doping Concentration and Temperature”. *Journal of The Electrochemical Society* 141.8 (1994), pp. 2262–2265. DOI: 10.1149/1.2055100.
- [60] I. C. Vickridge, J. J. Ganem, G. Battistig, and E. Szilagy. “Oxygen Isotopic Tracing Study of the Dry Thermal Oxidation of 6H-SiC”. *Nuclear Instruments and Methods in Physics Research Section B* 161 (2000), pp. 462–466. DOI: 10.1016/s0168-583x(99)00931-3.
- [61] J. M. Knaup, P. Deák, T. Frauenheim, A. Gali, Z. Hajnal, and W. J. Choyke. “Theoretical Study of the Mechanism of Dry Oxidation of 4H–SiC”. *Physical Review B* 71.23 (2005), p. 235321. DOI: 10.1103/physrevb.71.235321.

- [62] B. E. Deal and A. S. Grove. “General Relationship for the Thermal Oxidation of Silicon”. *Journal of Applied Physics* 36.12 (1965), pp. 3770–3778. DOI: 10.1063/1.1713945.
- [63] Y. Song, S. Dhar, L. C. Feldman, G. Chung, and J. R. Williams. “Modified Deal Grove Model for the Thermal Oxidation of Silicon Carbide”. *Journal of Applied Physics* 95.9 (2004), pp. 4953–4957. DOI: 10.1063/1.1690097.
- [64] H. Z. Massoud, J. D. Plummer, and E. A. Irene. “Thermal Oxidation of Silicon in Dry Oxygen Growth-Rate Enhancement in the Thin Regime I. Experimental Results”. *Journal of the Electrochemical Society* 132.11 (1985), pp. 2685–2693. DOI: 10.1149/1.2113648.
- [65] H. Z. Massoud, J. D. Plummer, and E. A. Irene. “Thermal Oxidation of Silicon in Dry Oxygen: Growth-Rate Enhancement in the Thin Regime II. Physical Mechanisms”. *Journal of the Electrochemical Society* 132.11 (1985), pp. 2693–2700. DOI: 10.1149/1.2113649.
- [66] T. Yamamoto, Y. Hijikata, H. Yaguchi, and S. Yoshida. “Oxide Growth Rate Enhancement of Silicon Carbide (0001) Si-faces in Thin Oxide Regime”. *Japanese Journal of Applied Physics* 47.10R (2008), p. 7803. DOI: 10.1143/jjap.47.7803.
- [67] T. Yamamoto, Y. Hijikata, H. Yaguchi, and S. Yoshida. “Oxygen-Partial-Pressure Dependence of SiC Oxidation Rate Studied by In Situ Spectroscopic Ellipsometry”. *Materials Science Forum* 600 (2009), pp. 667–670. DOI: 10.4028/www.scientific.net/msf.600-603.667.
- [68] T. Yamamoto, Y. Hijikata, H. Yaguchi, and S. Yoshida. “Growth Rate Enhancement of (0001)-Face Silicon–Carbide Oxidation in Thin Oxide Regime”. *Japanese Journal of Applied Physics* 46.8L (2007), p. L770. DOI: 10.1143/jjap.46.l770.
- [69] Y. Hijikata, H. Yaguchi, and S. Yoshida. “A Kinetic Model of Silicon Carbide Oxidation Based on the Interfacial Silicon and Carbon Emission Phenomenon”. *Applied Physics Express* 2.2 (2009), p. 021203. DOI: 10.1143/apex.2.021203.
- [70] D. Goto, Y. Hijikata, S. Yagi, and H. Yaguchi. “Differences in SiC Thermal Oxidation Process Between Crystalline Surface Orientations Observed by In-Situ Spectroscopic Ellipsometry”. *Journal of Applied Physics* 117.9 (2015), p. 095306. DOI: 10.1063/1.4914050.
- [71] Y. Hijikata, R. Asafuji, R. Konno, Y. Akasaka, and R. Shinoda. “Si and C Emission Into the Oxide Layer During the Oxidation of Silicon Carbide and its Influence on the Oxidation Rate”. *AIP Advances* 5.6 (2015), p. 067128. DOI: 10.1063/1.4922536.
- [72] V. Šimonka, A. Hössinger, J. Weinbub, and S. Selberherr. “Growth Rates of Dry Thermal Oxidation of 4H-Silicon Carbide”. *Journal of Applied Physics* 120.13 (2016), p. 135705. DOI: 10.1063/1.4964688.

- [73] V. Šimonka, G. Nawratil, A. Hössinger, J. Weinbub, and S. Selberherr. “Anisotropic Interpolation Method of Silicon Carbide Oxidation Growth Rates for Three-Dimensional Simulation”. *Solid-State Electronics* 128 (2017), pp. 135–140. DOI: 10.1016/j.sse.2016.10.032.
- [74] H. Kageshima, K. Shiraishi, and M. Uematsu. “Universal Theory of Si Oxidation Rate and Importance of Interfacial Si Emission”. *Japanese Journal of Applied Physics* 38.9A (1999), p. L971. DOI: 10.1143/JJAP.38.L971.
- [75] D. Goto and Y. Hijikata. “Unified Theory of Silicon Carbide Oxidation Based on the Si and C Emission Model”. *Journal of Physics D* 49.22 (2016), p. 225103. DOI: 10.1088/0022-3727/49/22/225103.
- [76] D. A. Newsome, D. Sengupta, H. Foroutan, M. F. Russo, and A. C. T. van Duin. “Oxidation of Silicon Carbide by O<sub>2</sub> and H<sub>2</sub>O: A ReaxFF Reactive Molecular Dynamics Study, Part I”. *The Journal of Physical Chemistry C* 116.30 (2012), pp. 16111–16121. DOI: 10.1021/jp306391p.
- [77] V. Šimonka, A. Hössinger, J. Weinbub, and S. Selberherr. “ReaxFF Reactive Molecular Dynamics Study of Orientation Dependence of Initial Silicon Carbide Oxidation”. *The Journal of Physical Chemistry A* 121.46 (2017), pp. 8791–8798. DOI: 10.1021/acs.jpca.7b08983.
- [78] H. Z. Massoud and J. D. Plummer. “Analytical Relationship for the Oxidation of Silicon in Dry Oxygen in the Thin-Film Regime”. *Journal of Applied Physics* 62.8 (1987), pp. 3416–3423. DOI: 10.1063/1.339305.
- [79] S. Ogawa and Y. Takakuwa. “Rate-Limiting Reactions of Growth and Decomposition Kinetics of Very Thin Oxides on Si (001) Surfaces Studied by Reflection High-Energy Electron Diffraction Combined with Auger Electron Spectroscopy”. *Japanese Journal of Applied Physics* 45.9R (2006), p. 7063. DOI: 10.1143/JJAP.45.7063.
- [80] M. Uematsu, H. Kageshima, and K. Shiraishi. “Simulation of Wet Oxidation of Silicon Based on the Interfacial Silicon Emission Model and Comparison with Dry Oxidation”. *Journal of Applied Physics* 89.3 (2001), pp. 1948–1953. DOI: 10.1063/1.1335828.
- [81] Y. Hijikata, H. Yaguchi, S. Yoshida, Y. Takata, K. Kobayashi, H. Nohira, and T. Hattori. “Characterization of Oxide Films on 4H–SiC Epitaxial (000 $\bar{1}$ ) Faces by High-Energy-Resolution Photoemission Spectroscopy: Comparison Between Wet and Dry Oxidation”. *Journal of Applied Physics* 100.5 (2006), p. 053710. DOI: 10.1063/1.2345471.
- [82] Y. Hijikata, S. Yagi, H. Yaguchi, and S. Yoshida. “Thermal Oxidation Mechanism of Silicon Carbide”. *Physics and Technology of Silicon Carbide Devices*. InTech, 2012. DOI: 10.5772/50748.
- [83] M. Uematsu, H. Kageshima, and K. Shiraishi. “Unified Simulation of Silicon Oxidation Based on the Interfacial Silicon Emission Model”. *Japanese Journal of Applied Physics* 39.7B (2000), p. L699. DOI: 10.1143/JJAP.39.L699.

- [84] M. Schürmann, S. Dreiner, U. Berges, and C. Westphal. “Structure of the Interface Between Ultrathin SiO<sub>2</sub> Films and 4H–SiC (0001)”. *Physical Review B* 74.3 (2006), p. 035309. DOI: 10.1103/PhysRevB.74.035309.
- [85] P. Fiorenza and V. Raineri. “Reliability of Thermally Oxidized SiO<sub>2</sub>/4H–SiC by Conductive Atomic Force Microscopy”. *Applied Physics Letters* 88.21 (2006), p. 2112. DOI: 10.1063/1.2207991.
- [86] N. Tokura, K. Hara, T. Miyajima, H. Fuma, and K. Hara. “Current-Voltage and Capacitance-Voltage Characteristics of Metal/Oxide/6H-Silicon Carbide Structure”. *Japanese Journal of Applied Physics* 34.10R (1995), p. 5567. DOI: 10.1143/JJAP.34.5567.
- [87] J. J. Ahn, Y. D. Jo, S. C. Kim, J. H. Lee, and S. M. Koo. “Crystallographic Plane-Orientation Dependent Atomic Force Microscopy-Based Local Oxidation of Silicon Carbide”. *Nanoscale Research Letters* 6.1 (2011), pp. 1–5. DOI: 10.1186/1556-276x-6-235.
- [88] K. Christiansen and R. Helbig. “Anisotropic Oxidation of 6H–SiC”. *Journal of Applied Physics* 79.6 (1996), pp. 3276–3281. DOI: 10.1063/1.361225.
- [89] S. K. Gupta and J. Akhtar. *Thermal Oxidation of Silicon Carbide (SiC)-Experimentally Observed Facts*. INTECH, 2011. DOI: 10.5772/20465.
- [90] K. Kakubari, R. Kuboki, Y. Hijikata, H. Yaguchi, and S. Yoshida. “Real Time Observation of SiC Oxidation Using an In Situ Ellipsometer”. *Materials Science Forum* 527 (2006), pp. 1031–1034. DOI: 10.4028/www.scientific.net/MSF.527-529.1031.
- [91] J. N. Shenoy, M. K. Das, J. A. Cooper Jr., M. R. Melloch, and J. W. Palmour. “Effect of Substrate Orientation and Crystal Anisotropy on the Thermally Oxidized SiO<sub>2</sub>/SiC Interface”. *Journal of Applied Physics* 79.6 (1996), pp. 3042–3045. DOI: 10.1063/1.361244.
- [92] V. Šimonka, G. Nawratil, A. Hössinger, J. Weinbub, and S. Selberherr. “Direction Dependent Three-Dimensional Silicon Carbide Oxidation Growth Rate Calculations”. *Proceedings of the Joint International EUROSIOI Workshop and International Conference on Ultimate Integration on Silicon (EUROSIOI-ULIS)*. 2016, pp. 226–229. DOI: 10.1109/ULIS.2016.7440094.
- [93] D. Potter. *Computational Physics*. Wiley, 1973.
- [94] J. Thijssen. *Computational Physics*. Cambridge University Press, 2007.
- [95] R. Macey, G. Oster, and T. Zahley. *Berkeley Madonna User’s Guide*. University of California, 2009.
- [96] S. Arrhenius. *Über die Dissociationswärme und den Einfluss der Temperatur auf den Dissociationsgrad der Elektrolyte*. Wilhelm Engelmann, 1889.
- [97] J. H. Wilkinson, F. L. Bauer, and C. Reinsch. *Linear Algebra*. Vol. 2. Springer-Verlag Berlin Heidelberg, 1971.

- 
- [98] S. R. Brown and L. E. Melamed. *Experimental Design and Analysis*. 74. Sage, 1990.
- [99] D. C. Montgomery. *Design and Analysis of Experiments*. John Wiley & Sons, 2017.
- [100] C. L. Lawson and R. J. Hanson. *Solving Least Squares Problems*. SIAM, 1995.
- [101] H. Kageshima, M. Uematsu, and K. Shiraishi. “Theory of Thermal Si Oxide Growth Rate Taking Into Account Interfacial Si Emission Effects”. *Microelectronic Engineering* 59.1 (2001), pp. 301–309. DOI: 10.1016/S0167-9317(01)00614-1.
- [102] Y. Hijikata. *Physics and Technology of Silicon Carbide Devices*. InTech, 2013. DOI: 10.5772/3428.
- [103] E. A. Irene, H. Z. Massoud, and E. Tierney. “Silicon Oxidation Studies: Silicon Orientation Effects on Thermal Oxidation”. *Journal of the Electrochemical Society* 133.6 (1986), pp. 1253–1256. DOI: 10.1149/1.2108829.
- [104] Y. Hijikata, H. Yaguchi, and S. Yoshida. “Model Calculations of SiC Oxide Growth Rate at Various Oxidation Temperatures Based on the Silicon and Carbon Emission Model”. *Materials Science Forum* 645 (2010), pp. 809–812. DOI: 10.4028/www.scientific.net/MSF.645-648.809.
- [105] V. Šimonka, G. Nawratil, A. Hössinger, J. Weinbub, and S. Selberherr. “Geometrical Aspects of Three-Dimensional Silicon Carbide Oxidation Growth Rate Modeling”. *Book of Abstracts of the Joint International EUROSIOI Workshop and International Conference on Ultimate Integration on Silicon (EUROSIOI-ULIS)*. 2016, pp. 128–129.
- [106] V. Šimonka, A. Hössinger, J. Weinbub, and S. Selberherr. “Three-Dimensional Growth Rate Modeling and Simulation of Silicon Carbide Thermal Oxidation”. *Proceedings of the International Conference on Simulation of Semiconductor Processes and Devices (SISPAD)*. 2016, pp. 233–237. DOI: 10.1109/SISPAD.2016.7605190.
- [107] C. T. Banzhaf, M. Grieb, A. Trautmann, A. J. Bauer, and L. Frey. “Characterization of Diverse Gate Oxides on 4H-SiC 3D Trench-MOS Structures”. *Materials Science Forum* 740 (2013), pp. 691–694. DOI: 10.4028/www.scientific.net/MSF.740-742.691.
- [108] T. Hosoi, K. Konzono, Y. Uenishi, S. Mitani, Y. Nakano, T. Nakamura, T. Shimura, and H. Watanabe. “Investigation of Surface and Interface Morphology of Thermally Grown SiO<sub>2</sub> Dielectrics on 4H-SiC (0001) Substrates”. *Materials Science Forum* 679 (2011), pp. 342–345. DOI: 10.4028/www.scientific.net/msf.679-680.342.
- [109] I. Vickridge, J. Ganem, Y. Hoshino, and I. Trimaille. “Growth of SiO<sub>2</sub> on SiC by Dry Thermal Oxidation: Mechanisms”. *Journal of Physics D* 40.20 (2007), p. 6254. DOI: 10.1088/0022-3727/40/20/S10.

- [110] J. Woerle, V. Šimonka, E. Müller, A. Hössinger, H. Sigg, S. Selberherr, J. Weinbub, M. Camarda, and U. Grossner. “Investigating Orientation-Dependent Oxidation of Macrosteps on 4H-SiC Epilayers”. *Proceedings of the European Conference on Silicon Carbide and Related Materials (ECSCRM)*. 2018, in print.
- [111] H. Matsunami and T. Kimoto. “Step-Controlled Epitaxial Growth of SiC: High Quality Homoepitaxy”. *Materials Science and Engineering: R* 20.3 (1997), pp. 125–166. DOI: 10.1016/S0927-796X(97)00005-3.
- [112] H. Fujiwara, T. Kimoto, T. Tojo, and H. Matsunami. “Characterization of In-Grown Stacking Faults in 4H-SiC (0001) Epitaxial Layers and its Impacts on High-Voltage Schottky Barrier Diodes”. *Applied Physics Letters* 87.5 (2005), p. 051912. DOI: 10.1063/1.1997277.
- [113] W. Chen and M. A. Capano. “Growth and Characterization of 4H-SiC Epilayers on Substrates with Different Off-Cut Angles”. *Journal of Applied Physics* 98.11 (2005), p. 114907. DOI: 10.1063/1.2137442.
- [114] G. Ciccotti, M. Ferrario, and C. Schuette. “Molecular Dynamics Simulation”. *Entropy* 16 (2014), p. 233.
- [115] A. C. T. Van Duin, S. Dasgupta, F. Lorant, and W. A. Goddard. “ReaxFF: A Reactive Force Field for Hydrocarbons”. *The Journal of Physical Chemistry A* 105.41 (2001), pp. 9396–9409. DOI: 10.1021/jp004368u.
- [116] T. P. Senftle, S. Hong, M. M. Islam, S. B. Kylasa, Y. Zheng, Y. K. Shin, C. Junkermeier, R. Engel-Herbert, M. J. Janik, H. M. Aktulga, T. Verstraelen, A. Grama, and A. C. T. van Duin. “The ReaxFF Reactive Force-Field: Development, Applications and Future Directions”. *npj Computational Materials* 2 (2016), p. 15011. DOI: 10.1038/npjcompumats.2015.11.
- [117] G.-Y. Li, J.-X. Ding, H. Zhang, C.-X. Hou, F. Wang, Y.-Y. Li, and Y.-H. Liang. “ReaxFF Simulations of Hydrothermal Treatment of Lignite and its Impact on Chemical Structures”. *Fuel* 154 (2015), pp. 243–251. DOI: 10.1016/j.fuel.2015.03.082.
- [118] S. Han, X. Li, F. Nie, M. Zheng, X. Liu, and L. Guo. “Revealing the Initial Chemistry of Soot Nanoparticle Formation by ReaxFF Molecular Dynamics Simulations”. *Energy & Fuels* 31 (2017), pp. 8434–8444. DOI: 10.1021/acs.energyfuels.7b01194.
- [119] M. M. Islam, A. Ostadhosseini, O. Borodin, A. T. Yeates, W. W. Tipton, R. G. Hennig, N. Kumar, and A. C. T. van Duin. “ReaxFF Molecular Dynamics Simulations on Lithiated Sulfur Cathode Materials”. *Physical Chemistry Chemical Physics* 17.5 (2015), pp. 3383–3393. DOI: 10.1039/c4cp04532g.

- [120] S. S. Han, S.-H. Choi, and A. C. T. van Duin. “Molecular Dynamics Simulations of Stability of Metal-Organic Frameworks Against H<sub>2</sub>O Using the ReaxFF Reactive Force Field”. *Chemical Communications* 46.31 (2010), pp. 5713–5715. DOI: 10.1002/chin.201043001.
- [121] J. C. Fogarty, H. M. Aktulga, A. Y. Grama, A. C. T. Van Duin, and S. A. Pandit. “A Reactive Molecular Dynamics Simulation of the Silica-Water Interface”. *The Journal of Chemical Physics* 132.17 (2010), p. 174704. DOI: 10.1063/1.3407433.
- [122] A. D. Kulkarni, D. G. Truhlar, S. Goverapet Srinivasan, A. C. T. van Duin, P. Norman, and T. E. Schwartzenuber. “Oxygen Interactions with Silica Surfaces: Coupled Cluster and Density Functional Investigation and the Development of a New ReaxFF Potential”. *The Journal of Physical Chemistry C* 117.1 (2012), pp. 258–269. DOI: 10.1021/jp3086649.
- [123] H. M. Aktulga, J. C. Fogarty, S. A. Pandit, and A. Y. Grama. “Parallel Reactive Molecular Dynamics: Numerical Methods and Algorithmic Techniques”. *Parallel Computing* 38.4 (2012), pp. 245–259. DOI: 10.1016/j.parco.2011.08.005.
- [124] *Vienna Scientific Cluster*. <http://vsc.ac.at/>. (accessed September 5, 2017).
- [125] T. Seyller. “Passivation of Hexagonal SiC Surfaces by Hydrogen Termination”. *Journal of Physics: Condensed Matter* 16.17 (2004), S1755. DOI: 10.1088/0953-8984/16/17/016.
- [126] H. J. C. Berensen, J. P. M. Postma, W. van Gunsteren, A. DiNola, and J. R. Haak. “Molecular Dynamics with Coupling to an External Bath”. *Journal of Chemical Physics* 81 (1984), p. 3684. DOI: 10.1063/1.448118.
- [127] D. A. Newsome, D. Sengupta, and A. C. T. van Duin. “High-Temperature Oxidation of SiC-Based Composite: Rate Constant Calculation from ReaxFF MD Simulations, Part II”. *The Journal of Physical Chemistry C* 117.10 (2013), pp. 5014–5027. DOI: 10.1021/jp307680t.
- [128] A. Hallén and M. Linnarsson. “Ion Implantation Technology for Silicon Carbide”. *Surface and Coatings Technology* 306 (2016), pp. 190–193. DOI: 10.1016/j.surfcoat.2016.05.075.
- [129] C. A. Fisher, R. Esteve, S. Doering, M. Roesner, M. de Biasio, M. Kraft, W. Schustereder, and R. Rupp. “An Electrical and Physical Study of Crystal Damage in High-Dose Al-and N-implanted 4H-SiC”. *Materials Science Forum* 897 (2017), pp. 411–414. DOI: 10.4028/www.scientific.net/MSF.897.411.
- [130] T. Kimoto, O. Takemura, H. Matsunami, T. Nakata, and M. Inoue. “Al<sup>+</sup> and B<sup>+</sup> Implantations into 6H-SiC Epilayers and Application to pn Junction Diodes”. *Journal of Electronic Materials* 27.4 (1998), pp. 358–364. DOI: 10.1007/s11664-998-0415-6.
- [131] D. K. Ferry. *Semiconductors*. Macmillan Publishing Company, 1991.

- [132] K. Seeger. *Semiconductor Physics*. Springer-Verlag Berlin Heidelberg, 2004. DOI: 10.1007/978-3-662-09855-4.
- [133] J. S. Blakemore. *Semiconductor Statistics*. Courier Corporation, 2002.
- [134] N. S. Saks, A. K. Agarwal, S. H. Ryu, and J. W. Palmour. “Low-Dose Aluminum and Boron Implants in 4H and 6H Silicon Carbide”. *Journal of Applied Physics* 90.6 (2001), pp. 2796–2805. DOI: 10.1063/1.1392958.
- [135] V. Šimonka, A. Hössinger, J. Weinbub, and S. Selberherr. “Modeling of Electrical Activation Ratios of Phosphorus and Nitrogen Doped Silicon Carbide”. *Proceedings of the International Conference on Simulation of Semiconductor Processes and Devices (SISPAD)*. 2017, pp. 125–128. DOI: 10.23919/SISPAD.2017.8085280.
- [136] V. Šimonka, A. Hössinger, J. Weinbub, and S. Selberherr. “Modeling and Simulation of Electrical Activation of Acceptor-Type Dopants in Silicon Carbide”. *Materials Science Forum* 924 (2018), pp. 192–195. DOI: 10.4028/www.scientific.net/MSF.924.192.
- [137] F. Schmid, M. Laube, G. Pensl, G. Wagner, and M. Maier. “Electrical Activation of Implanted Phosphorus Ions in [0001] and [11-20]-Oriented 4H-SiC”. *Journal of Applied Physics* 91.11 (2002), pp. 9182–9186. DOI: 10.4028/www.scientific.net/msf.389-393.787.
- [138] M. Laube, F. Schmid, G. Pensl, G. Wagner, M. Linnarsson, and M. Maier. “Electrical Activation of High Concentrations of N<sup>+</sup> and P<sup>+</sup> Ions Implanted Into 4H-SiC”. *Journal of Applied Physics* 92.1 (2002), pp. 549–554. DOI: 10.1063/1.1479462.
- [139] V. Heera, D. Panknin, and W. Skorupa. “p-Type Doping of SiC by High Dose Al Implantation—Problems and Progress”. *Applied Surface Science* 184.1 (2001), pp. 307–316. DOI: 10.1016/S0169-4332(01)00510-4.
- [140] F. Schmid and G. Pensl. “Comparison of the Electrical Activation of P<sup>+</sup> and N<sup>+</sup> Ions Co-Implanted Along with Si<sup>+</sup> or C<sup>+</sup> Ions into 4H-SiC”. *Applied Physics Letters* 84.16 (2004), pp. 3064–3066. DOI: 10.1063/1.1707220.
- [141] T. Troffer, C. Peppermüller, G. Pensl, K. Rottner, and A. Schöner. “Phosphorus-Related Donors in 6H-SiC Generated by Ion Implantation”. *Journal of Applied Physics* 80.7 (1996), pp. 3739–3743. DOI: 10.1063/1.363325.
- [142] M. V. Rao, J. B. Tucker, M. C. Ridgway, O. W. Holland, N. Papanicolaou, and J. Mittereder. “Ion-Implantation in Bulk Semi-Insulating 4H-SiC”. *Journal of Applied Physics* 86.2 (1999), pp. 752–758. DOI: 10.1063/1.370799.
- [143] T. Tsirimpis, M. Krieger, H. B. Weber, and G. Pensl. “Electrical Activation of B<sup>+</sup>-Ions Implanted into 4H-SiC”. *Materials Science Forum* 645 (2010), pp. 697–700. DOI: 10.4028/www.scientific.net/msf.645-648.697.

- [144] M. A. Capano, J. A. Cooper Jr., M. R. Melloch, A. Saxler, and W. C. Mitchel. “Ionization Energies and Electron Mobilities in Phosphorus and Nitrogen-Implanted 4H-Silicon Carbide”. *Journal of Applied Physics* 87.12 (2000), pp. 8773–8777. DOI: 10.4028/www.scientific.net/msf.338-342.703.
- [145] A. Parisini, M. Gorni, A. Nath, L. Belsito, M. V. Rao, and R. Nipoti. “Remarks on the Room Temperature Impurity Band Conduction in Heavily Al<sup>+</sup> Implanted 4H–SiC”. *Journal of Applied Physics* 118.3 (2015), p. 035101. DOI: 10.1063/1.4926751.
- [146] Y. Negoro, K. Katsumoto, T. Kimoto, and H. Matsunami. “Electronic Behaviors of High-Dose Phosphorus-Ion Implanted 4H–SiC (0001)”. *Journal of Applied Physics* 96.1 (2004), pp. 224–228. DOI: 10.1063/1.1756213.
- [147] T. Troffer, M. Schadt, T. Frank, H. Itoh, G. Pensl, J. Heindl, H. P. Strunk, and M. Maier. “Doping of SiC by Implantation of Boron and Aluminum”. *Physica Status Solidi (a)* 162.1 (1997), pp. 277–298. DOI: 10.1002/1521-396x(199707)162:1<277::aid-pssa277>3.0.co;2-c.
- [148] J. M. Bluet, J. Pernot, J. Camassel, S. Contreras, J. L. Robert, J. F. Michaud, and T. Billon. “Activation of Aluminum Implanted at High Doses in 4H–SiC”. *Journal of Applied Physics* 88.4 (2000), pp. 1971–1977. DOI: 10.1063/1.1305904.
- [149] V. Šimonka, A. Hössinger, J. Weinbub, and S. Selberherr. “Modeling and Simulation of Electrical Activation of Acceptor-Type Dopants in Silicon Carbide”. *Proceedings of the International Conference on Silicon Carbide and Related Materials (ICSCRM)*. 2017, p. 2756130.
- [150] A. F. Hayes. *Introduction to Mediation, Moderation, and Conditional Process Analysis: A Regression-Based Approach*. Guilford Press, 2013.
- [151] T. Kimoto and N. Inoue. “Nitrogen Ion Implantation into  $\alpha$ -SiC Epitaxial Layers”. *Physica Status Solidi (a)* 162.1 (1997), pp. 263–276. DOI: 10.1002/1521-396x(199707)162:1<263::aid-pssa263>3.0.co;2-w.
- [152] N. S. Saks, A. V. Suvorov, and D. C. Capell. “High Temperature High-Dose Implantation of Aluminum in 4H–SiC”. *Applied Physics Letters* 84.25 (2004), pp. 5195–5197. DOI: 10.1063/1.1764934.
- [153] M. A. Capano, S. Ryu, M. R. Melloch, J. A. Cooper Jr., and M. R. Buss. “Dopant Activation and Surface Morphology of Ion Implanted 4H-and 6H-Silicon Carbide”. *Journal of Electronic Materials* 27.4 (1998), pp. 370–376. DOI: 10.1007/s11664-998-0417-4.
- [154] V. Šimonka, A. Hössinger, J. Weinbub, and S. Selberherr. “Empirical Model for Electrical Activation of Aluminum-and Boron-Implanted Silicon Carbide”. *IEEE Transactions on Electron Devices* 65.2 (2018), pp. 674–679. DOI: 10.1109/TED.2017.2786086.

- [155] J. Weisse, M. Hauck, T. Sledziewski, M. Tschiesche, M. Krieger, A. Bauer, H. Mitlehner, L. Frey, and T. Erlbacher. “Analysis of Compensation Effects in Aluminum-Implanted 4H–SiC Devices”. *Materials Science Forum* 924 (2018), pp. 184–187. DOI: 10.4028/www.scientific.net/MSF.924.184.
- [156] R. Nipoti, A. Carnera, G. Alfieri, and L. Kranz. “About the Electrical Activation of  $1 \times 10^{20} \text{ cm}^{-3}$  Ion Implanted Al in 4H–SiC at Annealing Temperatures in the Range 1500 – 1950°C”. *Materials Science Forum* 924 (2018), pp. 333–338. DOI: 10.4028/www.scientific.net/MSF.924.333.
- [157] P. Fedeli, M. Gorni, A. Carnera, A. Parisini, G. Alfieri, U. Grossner, and R. Nipoti. “1950°C Post Implantation Annealing of Al<sup>+</sup> Implanted 4H–SiC: Relevance of the Annealing Time”. *ECS Journal of Solid State Science and Technology* 5.9 (2016), P534–P539. DOI: 10.1149/2.0361609jss.
- [158] V. Šimonka, A. Hössinger, S. Selberherr, and J. Weinbub. “Investigation of Post-Implantation Annealing for Phosphorus-Implanted 4H-Silicon Carbide”. *Proceedings of the International Conference on Microelectronic Devices and Technologies (MicDAT)*. 2018, pp. 42–44.
- [159] V. Šimonka, A. Toifl, A. Hössinger, S. Selberherr, and J. Weinbub. “Transient Model for Electrical Activation of Aluminium and Phosphorus-Implanted Silicon Carbide”. *Journal of Applied Physics* 123.23 (2018), p. 235701. DOI: 10.1063/1.5031185.
- [160] A. Parisini and R. Nipoti. “Analysis of the Hole Transport Through Valence Band States in Heavy Al Doped 4H–SiC by Ion Implantation”. *Journal of Applied Physics* 114.24 (2013), p. 243703. DOI: 10.1063/1.4852515.
- [161] J. Senzaki, K. Fukuda, and K. Arai. “Influences of Postimplantation Annealing Conditions on Resistance Lowering in High-Phosphorus-Implanted 4H–SiC”. *Journal of Applied Physics* 94.5 (2003), pp. 2942–2947. DOI: 10.1063/1.1597975.
- [162] R. Nipoti, R. Scaburri, A. Hallén, and A. Parisini. “Conventional Thermal Annealing for a More Efficient p-type Doping of Al<sup>+</sup> Implanted 4H–SiC”. *Journal of Materials Research* 28.1 (2013), pp. 17–22. DOI: 10.1557/jmr.2012.207.
- [163] W. Hailei, S. Guosheng, Y. Ting, Y. Guoguo, W. Lei, Z. Wanshun, L. Xingfang, Z. Yiping, and W. Jialiang. “Effect of Annealing Process on the Surface Roughness in Multiple Al Implanted 4H–SiC”. *Journal of Semiconductors* 32.7 (2011), p. 072002. DOI: 1674-4926/32/7/072002.
- [164] S. G. Sundaresan, M. V. Rao, Y.-l. Tian, M. C. Ridgway, J. A. Schreifels, and J. J. Kopanski. “Ultrahigh-Temperature Microwave Annealing of Al<sup>+</sup>- and P<sup>+</sup>- Implanted 4H–SiC”. *Journal of Applied Physics* 101.7 (2007), p. 073708. DOI: 10.1063/1.2717016.
- [165] B. Wendroff. *Theoretical Numerical Analysis*. Elsevier, 2014.

- [166] T. Kimoto, K. Kawahara, N. Kaji, H. Fujihara, and J. Suda. “Ion Implantation Technology in SiC for High-Voltage/High-Temperature Devices”. *Proceedings of the International Workshop on Junction Technology (IWJT)*. 2016, pp. 54–58. DOI: 10.1109/iwjt.2016.7486673.
- [167] R. Nipoti, A. Parisini, G. Sozzi, M. Puzanghera, A. Parisini, and A. Carnera. “Structural and Functional Characterizations of Al<sup>+</sup> Implanted 4H-SiC Layers and Al<sup>+</sup> Implanted 4H-SiC pn Junctions after 1950°C Post Implantation Annealing”. *ECS Journal of Solid State Science and Technology* 5.10 (2016), P621–P626. DOI: 10.1149/2.0211610jss.



# Curriculum Vitae

## Personal Information

Name	Vito Šimonka
Address	Argentinerstraße 16/3/44, 1040 Vienna, Austria
Nationality	Slovenian
Date of Birth	April 18, 1991
Place of Birth	Murska Sobota, Slovenia

## Academic Career and Positions

since 10/2015	Doctoral Student Supervisor: Prof. Dr. Siegfried Selberherr Institute for Microelectronics, TU Wien, Austria
since 08/2015	Research Assistant Christian Doppler Laboratory for High Performance TCAD Institute for Microelectronics, TU Wien, Austria
07/2015	Master's Degree in Physics Supervisor: Prof. Dr. Matjaž Perc Faculty of Natural Sciences and Mathematics, University of Maribor, Slovenia
10/2013 - 10/2015	Student Research Assistant European Social Fund project University of Maribor, Slovenia

09/2012	Bachelors's Degree in Physics Supervisors: Doc. Dr. Aleš Fajmut and Prof. Dr. Milan Brumen Faculty of Natural Sciences and Mathematics, University of Maribor, Slovenia
06/2012 - 09/2012	Internship FMC, sistemski integrator d.o.o., Slovenia

## Professional Training

11/2016	VSC Training Course: Shared Memory Parallelization with OpenMP, Vienna, Austria
09/2016	Dresden Microelectronics Academy 2016, Dresden, Germany
04/2016	VSC Training Course: Efficient Parallel Applications using Intel developer tools, Vienna, Austria
07/2013 - 09/2013	PRACE Summer of High Performance Computing, Barcelona, Spain
10/2013	Challenge Future Summit, Maribor, Slovenia
11/2012	PoliMaT Academy TalentCamp, Ljubljana, Slovenia

## Awards

01/2017	Rectors Award University of Maribor, Slovenia
05/2016	Best Master's Thesis in the Field of Science and Technology Educational Fundation of Pomurje, Slovenia
12/2015	Diploma Magna Cum Laude Faculty of Natural Sciences and Mathematics, University of Maribor, Slovenia

09/2015	Award for Excellent Research Work Faculty of Natural Sciences and Mathematics, University of Maribor, Slovenia
05/2015	The Best Student of University of Maribor University of Maribor, Slovenia
12/2013	Summer of HPC Ambassador Award PRACE, Spain
10/2012 - 10/2015	Zois Scholarship Public Fund of Slovenia for Excellence, Slovenia



# Own Publications

## Journal Articles

- [8] V. Šimonka, A. Toifl, A. Hössinger, S. Selberherr, and J. Weinbub. "Transient Model for Electrical Activation of Aluminium and Phosphorus-Implanted Silicon Carbide". *Journal of Applied Physics* 123 (2018), pp. 235701-1–235701-7. DOI: 10.1063/1.5031185.
- [7] V. Šimonka, A. Hössinger, J. Weinbub, and S. Selberherr. "Modeling and Simulation of Electrical Activation of Acceptor-Type Dopants in Silicon Carbide". *Materials Science Forum* 924 (2018), pp. 192–195. DOI: 10.4028/www.scientific.net/MSF.924.192.
- [6] V. Šimonka, A. Hössinger, J. Weinbub, and S. Selberherr. "Empirical Model for Electrical Activation of Aluminium-and Boron-Implanted Silicon Carbide". *IEEE Transactions on Electron Devices* 65 (2017), pp. 1–6. DOI: 10.1109/ted.2017.2786086.
- [5] V. Šimonka, A. Hössinger, J. Weinbub, and S. Selberherr. "ReaxFF Reactive Molecular Dynamics Study of Orientation Dependence of Initial Silicon Carbide Oxidation". *Journal of Physical Chemistry A* 121 (2017), pp. 8791–8798. DOI: 10.1021/acs.jpca.7b08983.
- [4] V. Šimonka, G. Nawratil, A. Hössinger, J. Weinbub, and S. Selberherr. "Anisotropic Interpolation Method of Silicon Carbide Oxidation Growth Rates for Three-Dimensional Simulation". *Solid-State Electronics* 128 (2017), pp. 135–14, **invited**. DOI: 10.1016/j.sse.2016.10.032.
- [3] V. Šimonka, A. Hössinger, J. Weinbub, and S. Selberherr. "Growth Rates of Dry Thermal Oxidation of 4H-Silicon Carbide". *Journal of Applied Physics* 120 (2016), pp. 135705. DOI: 10.1063/1.4964688.
- [2] V. Šimonka, M. Fras, and M. Gosak. "Stochastic Simulation of the Circadian Rhythmicity in the SCN Neuronal Network". *Physica A* 424 (2015), pp. 1-10. DOI: 10.1016/j.physa.2014.12.034.
- [1] R. Repnik, S. A. Ranjkesh, V. Šimonka, M. Ambrožič, Z. Bradač, and S. Kralj. "Symmetry Breaking in Nematic Liquid Crystals: Analogy with Cosmology and Magnetism". *Journal of Physics: Condensed Matter* 25 (2013), pp. 404201-1-404201-10. DOI: 10.1088/0953-8984/25/40/404201.

## Book Contributions

- [1] V. Šimonka, A. Hössinger, J. Weinbub, and S. Selberherr. "Direction Dependent Three-Dimensional Silicon Carbide Oxidation Growth Rate Calculations". *Proceedings of the Joint International EUROSIOI Workshop and International Conference on Ultimate Integration on Silicon (EUROSIOI-ULIS)*. 2016, pp. 226–229. DOI: 10.1109/ULIS.2016.7440094.

## Conference Contributions

- [11] J. Wörle, V. Šimonka, E. Müller, A. Hössinger, H. Sigg, S. Selberherr, J. Weinbub, M. Camarda, and U. Grossner. "Investigating Orientation-Dependent Oxidation of Macrosteps on 4H-SiC Epilayers". *Proceedings of the European Conference on Silicon Carbide and Related Materials (ECSCRM)*. 2018, in print.
- [10] A. Toifl, V. Šimonka, A. Hössinger, S. Selberherr, and J. Weinbub. "Steady-State Empirical Model for Electrical Activation of Silicon-Implanted Gallium Nitride". *Proceedings of the International Conference on Simulation of Semiconductor Processes and Devices (SISPAD)*. 2018, in print.
- [9] V. Šimonka, A. Hössinger, J. Weinbub, and S. Selberherr. "Modeling and Simulation of Electrical Activation of Acceptor-Type Dopants in Silicon Carbide". *Proceedings of the International Conference on Silicon Carbide and Related Materials (ICSCRM)*. 2017, p. 2756130.
- [8] V. Šimonka, A. Hössinger, J. Weinbub, and S. Selberherr. "Modeling of Electrical Activation Ratios of Phosphorus and Nitrogen Doped Silicon Carbide". *Proceedings of the International Conference on Simulation of Semiconductor Processes and Devices (SISPAD)*. 2017, pp. 125–128. DOI: 10.23919/SISPAD.2017.8085280.
- [7] P. Manstetten, V. Šimonka, G. Diamantopoulos, L. Gnam, A. Makarov, A. Hössinger, J. Weinbub. "Computational and Numerical Challenges in Semiconductor Process Simulation". *Proceedings of the SIAM Conference on Computational Science and Engineering (CSE)*. 2017, pp. 46.
- [6] V. Šimonka, A. Hössinger, J. Weinbub, and S. Selberherr. "Three-Dimensional Growth Rate Modeling and Simulation of Silicon Carbide Thermal Oxidation". *Proceedings of the International Conference on Simulation of Semiconductor Processes and Devices (SISPAD)*. 2016, pp. 233–236. DOI: 10.1109/SISPAD.2016.7605190.

- [5] **V. Šimonka**, G. Nawratil, A. Hössinger, J. Weinbub, and S. Selberherr. "Geometrical Aspects of Three-Dimensional Silicon Carbide Oxidation Growth Rate Modeling". *Book of Abstracts of the Joint International EUROSIOI Workshop and International Conference on Ultimate Integration on Silicon (EUROSIOI-ULIS)*. 2016, pp. 128–129.
- [4] **V. Šimonka**, M. Fras, and M. Gosak. "Stochastic Simulations of the Spatio-Temporal Circadian Activity in the Suprachiasmatic Nucleus". *Proceedings of the Symposia of Physicists University of Maribor*. 2014, p. 61.
- [3] **V. Šimonka**, V. Pohorec, A. Fajmut, and M. Brumen. "From Arterial Shear Stress to the Development of Vascular Smooth Muscle Force: Systems Biology Approach". *Book of Abstracts of the Conference on Systems Biology of Mammalian Cells*. 2014, p. 80.
- [2] **V. Šimonka**, V. Pohorec, A. Fajmut, and M. Brumen. "Role of Nitric Oxide in Pathogenesis of Atherosclerosis: Modelling Approach". *Book of Abstracts of the Regional Biophysics Conference*. 2014, p. 66.
- [1] **V. Šimonka**, M. Bernhardt, and M. Brumen. "Mathematical Modeling of Regulation of Glucose Concentration in Blood". *Book of Abstracts of the Regional Biophysics Conference*. 2012, p. 108.

## Invited Talks

- [1] **V. Šimonka**. "Natančni Fizikalni Modeli 3D Simulatorjev Proizvodnje Mikroelektronskih Naprav". *Faculty of Natural Sciences and Mathematics, University of Maribor, Slovenia*. 2017, **invited**.

